Myristoylated Neuronal Calcium Sensor-1 captures the ciliary vesicle at distal appendages

Tomoharu Kanie[1,2,4], Roy Ng[1], Keene L. Abbott[1], Olaf Pongs[3], and Peter K. Jackson[1,4]

[1]Baxter Laboratory, Department of Microbiology & Immunology and Department of Pathology, Stanford University, Stanford, CA, 94305

[2]Department of Cell Biology, University of Oklahoma Health Sciences Center, Oklahoma, OK, 73112

[3]Institute for Physiology, Center for Integrative Physiology and Molecular Medicine (CIPPM), Saarland University, Homburg, Germany

[4]Corresponding authors

Summary (230 Words)

The primary cilium is a microtubule-based organelle that cycles through assembly and disassembly. In many cell types, formation of the cilium is initiated by recruitment of ciliary vesicles to the distal appendage of the mother centriole. However, the distal appendage mechanism that directly captures ciliary vesicles is yet to be identified. In an accompanying paper, we show that the distal appendage protein, CEP89, is important for the ciliary vesicle recruitment, but not for other steps of cilium formation. The lack of a membrane binding motif in CEP89 suggests that it may indirectly recruit ciliary vesicles via another binding partner. Here, we identify Neuronal Calcium Sensor-1 (NCS1) as a stoichiometric interactor of CEP89. NCS1 localizes to the position between CEP89 and a ciliary vesicle marker, RAB34, at the distal appendage. This localization was completely abolished in CEP89 knockouts, suggesting that CEP89 recruits NCS1 to the distal appendage. Similarly to CEP89 knockouts, ciliary vesicle recruitment as well as subsequent cilium formation was perturbed in NCS1 knockout cells. The ability of NCS1 to recruit the ciliary vesicle is dependent on its myristoylation motif and NCS1 knockout cells expressing myristoylation defective mutant failed to rescue the vesicle recruitment defect despite localizing proper localization to the centriole. In sum, our analysis reveals the first known mechanism for how the distal appendage recruits the ciliary vesicles.

Introduction

The primary cilium is an organelle that consists of the microtubule-based axoneme surrounded by the ciliary membrane, which accumulates specific membrane proteins (e.g., G-protein coupled receptors) to serve as a sensor for extracellular environmental cues (Reiter & Leroux, 2017). The cilium extends from the mother centriole, and cycles assembly and disassembly, as the cell needs to disassemble the cilium prior to mitosis (Vorobjev & Chentsov Yu, 1982) to allow the centrosome to function within the spindle pole during mitosis. The processes of the cilium formation were described in great detail through electron microscopy by Sergei Sorokin in 1960s (S. Sorokin, 1962) (S. P. Sorokin, 1968) and is known to be subdivided to two types called the extracellular and intracellular pathways (Molla-Herman et al., 2010). In the extracellular pathway used, for example, by mouse inner medullary collecting duct cells (mIMCD3 cells), the mother centriole is believed to first dock to the plasma membrane before the extension of the axonemal microtubule as well as ciliary membrane (Molla-Herman et al., 2010). In the intracellular pathway used, for example, by Retinal Pigment Epithelia (RPE) cells (Molla-Herman et al., 2010) and fibroblasts (S. Sorokin, 1962) (Molla-Herman et al., 2010), the first step of cilium formation is attachment of the small vesicles, or so-called ciliary vesicles, to the distal end of the mother centriole (S. Sorokin, 1962), or more specifically to the distal appendage (Schmidt et al., 2012; Sillibourne et al., 2013). The distal appendage is a nine-fold blade-like structure attached to the distal end of the mother centriole (Anderson, 1972; Bowler et al., 2019; Paintrand, Moudjou, Delacroix, & Bornens, 1992). The ciliary vesicle recruitment is followed by the fusion of the small vesicles (Lu et al., 2015), removal of CP110 (Lu et al., 2015), which is believed to cap the distal end of the mother centriole (Spektor, Tsang, Khoo, & Dynlacht, 2007), and subsequently axonemal extension, which is mediated at least partially by

53 intraflagellar transport (IFT) (Craft, Harris, Hyman, Kner, & Lechtreck, 2015). While the distal
54 appendage is indispensable for all those steps, how exactly the distal appendage controls these
55 multiple processes is largely unknown.

56 To understand the molecular roles of the distal appendage, we first need to uncover its
57 molecular composition and identify critical functions of distal appendage proteins. In an
58 accompanying paper, we comprehensively analyzed all known distal appendage proteins to date
59 and revealed that the Centrosomal Protein 89 (CEP89) is important for ciliary vesicle
60 recruitment, but not for other processes organizing cilium formation. Since CEP89 lacks
61 apparent lipid binding motifs, we hypothesized that an interacting partner of CEP89 may bind to
62 ciliary vesicle directly. We sought to identify and understand the protein directly recruiting the
63 ciliary vesicle.

64 **Results**

65 **Discovery of Neuronal Calcium Sensor-1 as a stoichiometric interactor of CEP89**

66 To identify interacting partners of CEP89, we performed tandem affinity purification and mass
67 spectrometry (TAP-MS) (Rigaut et al., 1999). Localization and affinity purification (LAP)
68 (Cheeseman & Desai, 2005) tagged CEP89 was expressed in retinal pigment epithelia
69 immortalized with human telomerase (RPE-hTERT), and CEP89 was immunoprecipitated first
70 by Green Fluorescent Protein (GFP) antibody beads followed by a second affinity precipitation
71 by S protein beads. Final eluates were resolved by SDS-PAGE gel and analyzed by silver-
72 staining (Figure 1A) and mass spectrometry (Figure 1B). This analysis identified two
73 stoichiometric interactors, Neuronal Calcium Sensor-1 (NCS1) and C3ORF14, consistent with
74 the previous high-throughput proteome analyses, which identified both proteins as either CEP89
75 interactors (Huttlin et al., 2021) or neighbors (Gupta et al., 2015). Consistent with the TAP-MS

76 data, endogenous NCS1 strongly coimmunoprecipitated with endogenous CEP89 (Figure 1-
77 figure supplement 1A).

78 NCS1 is a member of NCS family proteins, which are characterized as containing
79 calcium binding EF-hand motifs as well as a myristoylation signal for N-terminal addition of
80 myristate (Burgoyne & Weiss, 2001). NCS1 was first identified as Frequenin in Drosophila, a
81 protein that can facilitate neurotransmitter release in neuromuscular junction (Pongs et al., 1993).
82 Since then, numerous papers propose models wherein NCS1 is involved in both presynaptic and
83 postsynaptic functions (reviewed in (Dason, Romero-Pozuelo, Atwood, & Ferrus, 2012)).
84 However, how exactly NCS-1 regulates neuronal function is still not well understood. As
85 described later in this paper, NCS-1 is expressed ubiquitously in various tissues, consistent with
86 the previous report (Gierke et al., 2004). While the previous literatures reported the role of NCS1
87 in other cell types including cardiomyocytes (Nakamura, Jeromin, Mikoshiba, & Wakabayashi,
88 2011) and adipocytes (Ratai, Hermainski, Ravichandran, & Pongs, 2019), molecular mechanisms
89 regulating non-neuronal functions of NCS1 remains enigmatic. A centrosomal role of NCS1 has
90 never been described.

91 CEP89 binding to NCS1 required the N-terminal region (1-343a.a.) (Figure 1C and D).
92 The C-terminal portion of CEP89 (344-783a.a.) is required for its centrosomal localization
93 (Figure 1- figure supplement 1B), consistent with a previous report (Sillibourne et al., 2013). An
94 *in vitro* binding assay using *in vitro* translated proteins revealed that HA tagged CEP89 directly
95 binds to MYC tagged C3ORF14 and NCS1 (Figure 1E), whereas HA-C3ORF14 did not bind to
96 NCS1 (Figure 1F). A negative control, CEP350 fragment (2470-2836 a.a.), which binds to its
97 binding partner FGFR1OP (or FOP) efficiently (Figure 1-figure supplement 2A) as previously
98 described (Kanie et al., 2017), did not bind to either HA-CEP89, nor HA-C3ORF14 (Figure 1E

99 and F). Thus, CEP89 serves to bridge NCS1 and C3ORF14 (Figure 1G).

100

101 **NCS1 is recruited to the distal appendage by CEP89 and is positioned between CEP89 and**

102 **the ciliary vesicle marker, RAB34**

103 We next sought to determine the precise localization of NCS1 and C3ORF14. When observed

104 via a wide-field microscopy, NCS1 localized to the mother centriole, marked by CEP170 (Figure

105 2A). Some cytoplasmic staining was also observed. Both centriolar and cytoplasmic staining was

106 highly specific as the signal was strongly reduced in NCS1 knockout cells (Figure 2A). The

107 cytoplasmic localization of NCS1 is inconsistent with a previous study, where C-terminally

108 Enhanced Yellow Fluorescent Protein (EYFP) tagged NCS1 constitutively localized to

109 membranous compartments (O'Callaghan et al., 2002). We tested if the difference in localization

110 is due to the tagging. We also tested whether membrane binding, myristoylation motif, of NCS1

111 affects its localization by making the myristoylation defective mutant by converting the position

112 2 glycine to alanine (NCS1-G2A). N-terminally LAP (EGFP and S) tagged wild-type or G2A

113 mutant of NCS1 localized to mother centriole as well as cytoplasm, similar to endogenous NCS1

114 (Figure 2- figure supplement 1A and B). Consistent with the previous paper (O'Callaghan et al.,

115 2002), C-terminally LAP tagged wild-type NCS1 localized to membrane compartments, such as

116 plasma membrane and endoplasmic reticulum, whereas the myristoylation defective mutant

117 (G2A) diffusely localized to cytoplasm (Figure 2-figure supplement 1C and D). This result

118 suggests that C-terminal tagging of NCS1 changes its localization potentially via exposing the

119 myristoylation motif of NCS1, and endogenous NCS1 may sequester its myristoylation motif to

120 allow localization to cytoplasm. A small amount of nuclear localization observed in LAP tagged

121 NCS1 likely derives from LAP tagging (Figure 2- figure supplement 1), as the endogenous

122 NCS1 did not localize to nucleus (Figure 2A). Similar to NCS1, C-terminally LAP tagged
123 C3ORF14 localized to the location between acetylated tubulin, a cilium marker, and Pericentrin,
124 a centrosome marker, suggesting that it also localizes specifically to the mother centriole (Figure
125 2B). NCS1 localization to the mother centriole was enhanced upon serum deprivation (Figure
126 2C), a condition that induces cilium formation in RPE cells, much like several other distal
127 appendage proteins (see Figure 1D of an accompanying paper for detail). When observed via 3D
128 structured illumination microscopy, of which resolution is twice as high as a diffraction limited
129 microscopy (Y. Wu & Shroff, 2018), C-terminally LAP (EGFP-S) tagged C3ORF14 localized to
130 a position slightly distal to the distal appendage protein, CEP164, in side-view (Figure 2D).
131 When top (or axial) view of the mother centriole was visualized, LAP-C3ORF14 formed a ring-
132 like structure that is slightly smaller than the CEP164 ring (Figure 2E), which is reminiscent of
133 the 9-fold symmetrical structure of the distal appendage (Paintrand et al., 1992). Similarly, NCS1
134 localized slightly distal to CEP164 (Figure 2F) as well as the binding partner, CEP89 (Figure
135 2G), and slightly proximal to the ciliary vesicle marker, RAB34 (Stuck, Chong, Liao, & Pazour,
136 2021)(see also the accompanying paper) (Figure 2H). Like C3ORF14, NCS1 formed a slightly
137 smaller ring than CEP164 (Figure 2I). Consistent with this, the ring diameter of NCS1 and
138 C3ORF14 was 319.5±7.7 nm (n=13, average±SEM) and 348.8±8.0 nm (n=16, average±SEM),
139 respectively (see Figure 1C of the accompanying paper). It is notable that both C3ORF14 and
140 NCS1 also localized to the region close to subdistal appendage in some but not all centrioles
141 (Figure 2D and F), consistent with what was observed for CEP89 localization (Chong et al.,
142 2020). This near subdistal appendage localization explains why C3ORF14 was previously
143 classified as a subdistal appendage protein (Gupta et al., 2015). These results suggest that NCS1
144 localizes to the distal appendage and more precisely to the position sandwiched between CEP89

145 and the ciliary vesicle (Figure 2J).

146 We next determined the hierarchy of the three proteins. Centriolar localization of CEP89 was not
147 affected by depletion of either NCS1 nor C3ORF14 (Figure 2K and Figure 2-figure supplement
148 2A). NCS1 failed to localize to the mother centriole without altering its cytoplasmic localization
149 in CEP89 knockout cells but not in C3ORF14 knockout cells (Figure 2L and Figure 2-figure
150 supplement 2B), indicating that CEP89 recruits NCS1 to the distal appendage. The lack of NCS1
151 localization at the centriole in CEP89 knockouts cells was rescued by expressing untagged
152 CEP89 (Figure 2L and Figure 2- figure supplement 2B). C3ORF14 localization required CEP89,
153 but not NCS1 (Figure 2M and Figure 2- figure supplement 2C). The expression level of neither
154 NCS1, nor C3ORF14 was affected by CEP89 depletion (Figure 2- figure supplement 2D and E).
155 These results suggest that both NCS1 and C3ORF14 are recruited to the distal appendage by
156 CEP89 (Figure 2N). We also tested whether the three proteins affect localization of other distal
157 appendage proteins and found that the localization of other distal appendage proteins were
158 unchanged in cells deficient in CEP89, NCS1, or C3ORF14 (Figure 2-figure supplement 3A-C)
159 (see also Figure 2A-L of the accompanying paper). Similar to the centriolar localization of
160 CEP89, which was significantly reduced in CEP83 or SCLT1 knockouts, NCS1 localization was
161 also greatly diminished in these knockouts (Figure 2-figure supplement 3D). This is consistent
162 with the observation that CEP83-SCLT1 module serves as a structural component of the distal
163 appendage (see an accompanying paper for the detail). In contrast, the feedback complex
164 CEP164-TTBK2 (see an accompanying paper for the detail) was required for proper centriolar
165 localization of NCS1 (Figure 2- figure supplement 3D) but not for CEP89 (Figure 2F of an
166 accompanying paper). Given that CEP89 is a substrate of TTBK2 (Bernatik et al., 2020; Lo et
167 al., 2019), this might suggest that phosphorylation of TTBK2 could affect the interaction

168 between CEP89 and NCS1. It is also possible that NCS1 may be a phosphorylation target of
169 TTBK2. These questions warrant future investigation.
170
171 **NCS1 is important for efficient ciliary vesicle recruitment at the distal appendage**
172 We next sought to understand the role of NCS1 at the distal appendage and performed kinetic
173 analysis of ciliation in control (sgGFP) and knockouts of CEP89, NCS1, or C3ORF14 in RPE
174 cells, in which serum starvation induces cilium formation (Figure 3A). Control RPE cells form
175 cilia over 24 hours after serum starvation, and almost of all cells completed cilium formation
176 between 24 and 48 hours. CEP89 and NCS1 knockouts displayed a notable delay in initiating
177 ciliation (see 12-hour in Figure 3A), but gradually catch up on ciliogenesis and exhibited only
178 mild ciliary formation defects at later time points (see 48 hours in Figure 3A). The cilium
179 formation defect was rescued by expressing untagged CEP89 in CEP89 knockouts or untagged
180 NCS1 in NCS1 knockouts (Figure 3B). This kinetic defect is strongly consistent with the
181 knockouts of several other distal appendage proteins, namely ANKRD26 and FBF1 (Figure 5A
182 and B of an accompanying paper). Consistent with the cells deficient in ANKRD26 or FBF1 (see
183 Figure 5- figure supplement 1 of an accompanying paper), ciliary ARL13B signal intensity was
184 reduced in CEP89 or NCS1 knockouts even after the cells complete cilium formation (Figure 3-
185 figure supplement 1A-C). This suggests that even though the NCS1 or CEP89 knockouts can
186 eventually form primary cilia, those cilia may be functionally different from wild-type cilia.
187 C3ORF14 knockouts showed similar but much milder kinetic defect of cilium formation than
188 CEP89 or NCS1 knockouts, therefore, we focused on NCS1 in the subsequent investigation.
189 We then sought to understand how NCS1 is involved in cilium formation. In an
190 accompanying paper, we showed that CEP89 participates in cilium formation by regulating

191 ciliary vesicle recruitment without affecting IFT88::CEP19 recruitment, important steps that
192 require distal appendage proteins (Schmidt et al., 2012) (Dateyama et al., 2019)(see Figure 5 of
193 an accompanying paper). We tested if NCS1 has similar roles to its binding partner, CEP89.
194 Indeed, NCS1 knockouts exhibited moderate ciliary vesicle recruitment defect, similar to CEP89
195 knockouts, when assessed using RAB34 as a ciliary vesicle marker (Figure 3C). Transmission
196 electron microscopy analysis confirmed the ciliary vesicle recruitment defect in NCS1 knockouts
197 (Figure 3D and E). The presence of fused vesicles, albeit much lower percentage than control
198 cells, in NCS1 knockouts (Figure 3D and E) suggests that NCS1 is important for recruitment but
199 not fusion of the ciliary vesicle. Removal of CP110, which is believed to act as a cap of
200 axonemal microtubule, was partially, but measurably affected in NCS1 knockout cells (Figure
201 3F), consistent with the fact that CP110 removal is in part downstream of ciliary vesicle
202 recruitment (Figure 4D of an accompanying paper). Neither IFT88 nor CEP19 recruitment to the
203 centriole was affected in NCS1 knockout cells (Figure 3G and H). These results suggest that
204 NCS1 plays an important role in cilium formation by regulating ciliary vesicle recruitment, but
205 not other known processes of cilium formation, consistent with the role of CEP89 in ciliary
206 vesicle recruitment.

207 **Yet unknown distal appendage proteins may compensate the lack of NCS1 in ciliary vesicle**
208 **recruitment**

209 As we showed in an accompanying paper, the distal appendage is indispensable for the
210 recruitment of the ciliary vesicle to the mother centriole. Virtually no RAB34 positive ciliary
211 vesicle was observed at mother centriole in cells deficient in CEP164, CEP83, or TTBK2, which
212 are critical for structural integrity of the distal appendage (Figure 5C of an accompanying paper).
213 This phenotype is much stronger than what we observed in CEP89 or NCS1 knockouts (Figure

214 3C), suggesting that some other distal appendage proteins may compensate the lack of NCS1 for
215 the ciliary vesicle recruitment. To address this question, we created cells lacking both NCS1 and
216 each of the other distal appendage proteins (FBF1, CEP89, ANKRD26, KIZ, LRRC45) as well
217 as the distal appendage associated protein, INPP5E (Figure 4A). We omitted the integral
218 components of the distal appendage proteins (CEP164, TTBK2, CEP83, SCLT1) from the
219 analysis, as the knockouts of these proteins showed very strong ciliary vesicle recruitment
220 defects on their own, therefore making it difficult to test if the NCS1 depletion shows additive
221 effects. Cilium formation assay revealed that depletion of NCS1 decreased the percentage of
222 ciliated cells in each single knockout cells, except CEP89 (Figure 4B and C). This suggests that
223 CEP89, but no other distal appendage protein regulates the same ciliary formation pathway as
224 NCS1. Similarly, depletion of NCS1 decreased the RAB34 positive centriole in each of the
225 single distal appendage knockout cells, except CEP89 knockouts (Figure 4D). These results
226 suggest that yet unknown distal appendage proteins would be required to compensate for the
227 ciliary vesicle recruitment defect of NCS1 knockout cells. Another possibility is that one or more
228 integral components (CEP164, TTBK2, SCLT1, and CEP83) may be directly involved in ciliary
229 vesicle recruitment. These hypotheses warrant future investigation.

230 **NCS1 captures ciliary vesicle via its myristoylation motif**

231 Since NCS1 is myristoylated, we wondered whether the membrane association motif is
232 necessary for NCS1 to recruit the ciliary vesicle. We tested this hypothesis by creating a
233 myristoylation defective mutant (NCS1-G2A). We tested whether the mutant indeed lost the
234 ability to bind membrane using differential centrifugation following nitrogen cavitation. We first
235 determined which fraction is the most optimal to assess membrane association in our
236 experimental setting. While the microsomal fraction prepared from the pellet following

237 ultracentrifugation at 100,000 g is often used to analyze membrane fraction of the cells (Graham,
238 2015), the plasma membrane marker, Epidermal Growth Factor Receptor (EGFR), was enriched
239 mostly in the pellet following centrifugation at 15,000 *g* in our experiment (Figure 5A; see
240 Methods for further explanation of the technical design). In addition, NCS1-G2A was
241 fractionated in the 100,000 *g* pellet to similar extent as wild-type NCS1 (Figure 5A), indicating
242 that centrifugation at 100,000 *g* may also pellet some soluble proteins, even though cytoplasmic
243 protein RabGDI remained in the 100,000 *g* supernatant. Thus, we decided to use 15,000 *g* pellet
244 to assess membrane fraction in our experiment. In control cells (sgSafe), both NCS1 and CEP89
245 was found in both soluble fraction (15,000 *g* supernatant) and membrane fraction (15,000 *g*
246 pellet) (Figure 5A). In contrast, NCS1-G2A was only found in the soluble fraction (15,000 *g*
247 supernatant) (Figure 5A), suggesting that myristoylation is required for membrane localization of
248 NCS1. Interestingly, CEP89 was only found in the soluble fraction (15,000 *g* supernatant) in
249 NCS1 knockout cells expressing either empty vector or NCS1-G2A, but not NCS1-WT. This
250 suggests that membrane localization of CEP89 requires NCS1 with an intact myristoylation
251 motif. When expressed at similar level to endogenous NCS1 (Figure 5B), both wild-type and the
252 myristoylation defective (G2A) NCS1 localizes to the mother centriole to a similar extent
253 (Figure 5C and D). However, the myristoylation defective mutant almost completely failed to
254 rescue ciliation and ciliary vesicle recruitment defect of NCS1 knockout cells (Figure 5E and F).
255 These data suggest that NCS1 recruits ciliary vesicle to the distal appendage via its
256 myristoylation motif (Figure 5G).

257 **Calcium binding is needed for stability of NCS1**

258 In addition to myristoylation motif, human NCS1 also has three functional and one apparently
259 non-functional (due to the mutation in critical amino acids needed for co-ordination bond with

260 calcium) EF-hand motifs (Bourne, Dannenberg, Pollmann, Marchot, & Pongs, 2001). Several
261 other NCS family proteins, including Recoverin and Hippocalcin, show a calcium-myristoyl
262 switch (Ames et al., 1997; O'Callaghan, Tepikin, & Burgoyne, 2003). In this mechanism, the
263 sequestered myristoylation motif is exposed to allow the protein to bind membrane upon calcium
264 binding. It has been proposed that NCS1 may employ a similar molecular switch. While the
265 structure of fission yeast Ncs1, solved by nuclear magnetic resonance spectroscopy showed the
266 calcium-myristoyl switch (Lim, Strahl, Thorner, & Ames, 2011), several lines of evidence
267 suggest the absence of that type of switch in budding yeast and mammalian NCS1(Ames et al.,
268 2000; O'Callaghan et al., 2002) (Lemire, Jeromin, & Boisselier, 2016). Since a myristoylation
269 defective mutant of NCS1 failed to form cilia efficiently without affecting its centrosomal
270 localization (Figure 5C and E), we tested if there is a calcium-myristoylation switch by making
271 various EF-hand mutations, where each or combination of the three active EF-hand motif was
272 disabled by mutating invariant glutamate at -Z position to glutamine (E84Q for the 1st, E120Q
273 for the 2nd, and E168Q for the 3rd active EF-hand mutation). We expressed *wild type* or EF-hand
274 mutants of untagged NCS1 in NCS1 knockout cells and detected the expression and the
275 localization of each mutant using α-NCS1 antibody. The wild-type and the mutants of NCS1
276 were functionally tested via ciliation assay rather than the ciliary vesicle recruitment assay,
277 because the ciliation assay is much less variable than the vesicle recruitment assay. Although the
278 E84Q mutant as well as any double and triple EF-hand mutants were highly destabilized (See
279 input in Figure 5- figure supplement 1A), centriolar NCS1 signal intensity of the mutant was
280 reduced in parallel to its diminished expression level. This suggests that the first EF hand is
281 indispensable for stability of NCS1. E120Q mutant had similar expression level, but its
282 centrosomal signal was significantly reduced (Figure 5- figure supplement 1B), consistent with

283 its diminished interaction with CEP89 (see IP: GFP in Figure 5- figure supplement 1A), a protein
284 that recruits NCS1 to the mother centriole (Figure 2L). This suggests that the second EF-hand is
285 involved in keeping its structure to interact with CEP89. E168Q had a negligible effect in
286 stability and localization of NCS1. The ciliation assay revealed that none of single EF-hand
287 mutants showed significant cilium formation defect (Figure 5- figure supplement 1C) despite the
288 partial reduction of centriolar signal intensity for E84Q and E120Q. The double or triple mutants
289 almost completely failed to rescue ciliation defect of NCS1 knockout cells (Figure 5-figure
290 supplement 5C), reflecting their very low expression level (Figure 5-figure supplement 1A).
291 These results suggest that calcium binding is primarily required for the structure and stability of
292 NCS1 and NCS1 does not clearly exhibit a calcium-myristoylation switch. The structural role of
293 calcium on NCS1 is largely consistent with NCS1's high binding affinity to calcium (-90 nM)
294 (Aravind et al., 2008).

295 **NCS1 is recruited to the centriole in a microtubule-independent manner where it captures**
296 **ciliary vesicles**

297 We next sought to understand where NCS1 captures ciliary vesicle. One possibility is that NCS1
298 captures the ciliary vesicle in the cytoplasm and then traffics it to the centriole by dynein-
299 dependent transport via microtubule. Another possibility is that NCS1 traffics to the centriole
300 first and then captures ciliary vesicles. To distinguish these two possibilities, we treated RPE
301 cells with nocodazole to destabilize microtubules, as microtubules were previously shown to be
302 indispensable for ciliary vesicle recruitment (C. T. Wu, Chen, & Tang, 2018). Consistent with
303 the previous report (C. T. Wu et al., 2018), destabilization of microtubule by nocodazole (Figure
304 6A and B) immediately inhibited ciliary vesicle recruitment and subsequent cilium formation
305 (Figure 6C and D), suggesting that ciliary vesicles are trafficked to the mother centriole via

306 microtubules. In contrast, centriolar NCS1 signal was gradually increased upon serum starvation
307 even in the presence of nocodazole (Figure 6E), suggesting that NCS1 accumulates at the distal
308 appendage by microtubule-independent mechanisms, possibly by diffusion, similar to the
309 previously proposed diffusion-to-capture model of IFT trafficking to the ciliary base (Hibbard,
310 Vazquez, Satija, & Wallingford, 2021). Because NCS1 is an N-terminally myristoylated protein,
311 we also considered whether NCS1 might be trafficked to the distal appendage through UNC119,
312 a chaperone that binds to N-myristoylated ciliary proteins like NPHP3 and cystin and traffics
313 them to the primary cilium (K. J. Wright et al., 2011). We conclude that NCS1 unlikely uses
314 UNC119 pathway, as we did not observe UNC119A/UNC119B in our AP/MS analysis of
315 CEP89 (Figure 1B-Source Data), nor in purifications of UNC119A/UNC119B proteins
316 themselves (K. J. Wright et al., 2011). In a complementary approach to the microtubule
317 destabilization, we tested if NCS1 localizes to the distal appendage even if the ciliary vesicle
318 recruitment is inhibited by RAB34 depletion (see Figure 4B and C of an accompanying paper).
319 We confirmed that centriolar NCS1 was comparable between control (sgSafe) and RAB34
320 knockout cells (Figure 6F), suggesting that NCS1 is recruited to the centriole independently from
321 the ciliary vesicle. These results suggest that NCS1 moves to the distal appendage possibly by
322 diffusion or an alternative trafficking mechanism and there it captures the ciliary vesicle that is
323 trafficked to the centriole by microtubule-dependent trafficking.

324 **NCS1 localizes to the ciliary base in neuronal and non-neuronal cells**

325 While the majority of papers to date focused on the role of NCS1 in neurons given its original
326 discovery as a protein that facilitates neurotransmitter release (Pongs et al., 1993), expression
327 analysis revealed that the protein is expressed ubiquitously in non-neuronal tissues (Gierke et al.,
328 2004). Since we discovered that NCS1 localizes to the centriole, a major microtubule organizing

329 center in animal cells (Bornens, 2012), we tested the expression and the localization of NCS1 in
330 neuronal and non-neuronal cell types. We first tested the expression of NCS1 in various murine
331 tissues and confirmed that NCS1 is expressed in a wide-range of tissues (Figure 7-figure
332 supplement 1A). The low expression level of NCS1 in liver, skeletal muscle, and fat might
333 reflect that most of the cells (hepatocyte, myocyte, and adipocytes, respectively) in those tissues
334 do not retain cilia, or because of the difference in ratio between intracellular and extracellular
335 proteins. When we performed immunofluorescence assay, NCS1 localized to both cytoplasm and
336 the ciliary base (a dot next to ciliary markers, ARL13B or AC3) in isolated hippocampal neuron
337 (top panel in Figure 7A) as well as cells in hypothalamus (Figure 7B) and the dentate gyrus of
338 the hippocampus (Figure 7-figure supplement 2C). Both cytoplasmic and the centriole signal was
339 specific for NCS1 as we detected no signal in NCS1 knockout cells (bottom panel in Figure 7A
340 and B, and Figure 7-figure supplement 2C). NCS1 also localized to the ciliary base in virtually
341 all the non-neuronal ciliated cells that we tested, including kidney epithelia, pancreatic islet cells,
342 airway epithelia, ependymal cells, and mouse embryonic fibroblasts (MEFs) (Figure 7C and D,
343 Figure 7-figure supplement 2A-D). Only ciliated cells where we failed to detect NCS1 at the
344 ciliary base was photoreceptor cells (Figure 7-figure supplement 2E). We next sought to
345 determine whether NCS1 is involved in cilium formation in those cells, as we saw in RPE cells
346 (Figure 3A and B). In MEFs, cilium formation is modestly perturbed in Ncs1 depleted cells
347 (Figure 7E and F), consistent with the kinetic cilium formation defect in RPE cells (Figure 3A).
348 Decrease in ciliary ARL13B signal was also detected in *Ncs1*$^{-/-}$ MEFs (Figure 7F), similar to
349 NCS1 knockout RPE cells (Figure 3-figure supplement 1). In contrast, we did not detect a
350 measurable cilium formation defect in hippocampal neurons that lack Ncs1 (Figure 7G), whereas
351 the signal of ciliary membrane protein, type III adenylyl cyclase (ADCY3) (Bishop, Berbari,

352 Lewis, & Mykytyn, 2007) (Berbari, Bishop, Askwith, Lewis, & Mykytyn, 2007), was
353 significantly decreased (Figure 7H). Other ciliary GPCRs, such as SSTR3 and GPR161, were
354 also decreased in *Ncs1*$^{-/-}$ neurons, but did not show statistical significance with the small number
355 of samples analyzed (Figure 7-fiure supplement 3A and B). The difference in the cilium
356 formation defect in different cell types (modest ciliation defects in RPE and MEFs, but no defect
357 in neurons) as well as potential signaling function of NCS1 will be discussed in the Discussion.

358 ***Ncs1* knockout mice exhibit obesity, but not other phenotypes related to ciliopathies**

359 To date, NCS1 has been characterized mainly in neuronal aspects, as NCS1 was classically
360 believed to be a neuron-specific calcium sensor (Olafsson et al., 1997). Ncs1 was shown to be
361 essential for memory formation in C. elegans. Mice lacking Ncs1 exhibited impairment of
362 memory formation (de Rezende et al., 2014; Saab et al., 2009) (Nakamura et al., 2017). Since
363 NCS1 is now shown to localize to the distal appendage in both neuronal and non-neuronal cells
364 and regulate efficient cilium formation at least in some cell types, we sought to test if *Ncs1*
365 knockout mice show phenotypes related to ciliopathies, pleiotropic disorders caused by
366 functional and structural dysfunction of cilia (Reiter & Leroux, 2017). A series of previous
367 mouse genetic studies showed that the loss of ciliary function in mice result in partially penetrant
368 pre-weaning lethality, obesity, retinal degeneration, and male infertility (Nishimura et al., 2004)
369 (Ding et al., 2020; Fath et al., 2005; Mykytyn et al., 2004). We assessed whether the previously
370 generated *Ncs1*$^{-/-}$ mice (Hermainski, 2012; Ng et al., 2016) exhibit ciliopathy phenotypes.
371 Inconsistent with the previous two reports (Nakamura et al., 2011) (Dickinson et al., 2016),
372 which generated *Ncs1* knockout mice independently, our *Ncs1*$^{-/-}$ mice did not exhibit pre-
373 weaning lethality (Figure 7A, p=0.369 in Chi-square test in data with male and female
374 combined). The difference between our data and the previous studies might derive from the

375 background of mice (C57BL6/J in our study and C57BL6/N in the previous studies). When body
376 weight was analyzed, both male and female *Ncs1*$^{-/-}$ mice became more obese than their
377 littermates starting at 9-10 weeks of age, and gained 10% more weight than the controls at 20
378 weeks (Figure 7B-C). The obesity phenotype is consistent with the previous reports (Nakamura
379 et al., 2011; Ratai et al., 2019) and is similar to what was observed in cilia-defective mice, which
380 became obese starting between 8-12 weeks (Ding et al., 2020; Fath et al., 2005; Mykytyn et al.,
381 2004; Nishimura et al., 2004). *Ncs1*$^{-/-}$ accumulated more fat than their littermate *Ncs1*$^{+/-}$ mice,
382 suggesting that the obesity phenotype at least partially comes from the increased fat amount in
383 *Ncs1*$^{-/-}$ mice. We also assessed other ciliopathy phenotypes, but *Ncs1*$^{-/-}$ did not show other cilia-
384 related symptoms, such as retinal degeneration (judged by thickness of outer nuclear layer),
385 polycystic kidney, and male infertility (Figure 8E-H). The absence of retinal degeneration, one of
386 the most penetrant phenotypes besides obesity in Bardet-Biedl syndrome (Forsythe & Beales,
387 2013) (Forsyth & Gunay-Aygun, 2020), might reflect the lack of Ncs1 at the ciliary base in
388 photoreceptors (Figure 7-figure supplement 2E). The milder phenotype of *Ncs1*$^{-/-}$ mice than the
389 previously reported cilia-defective mice may reflect mild-modest cilium formation defect of
390 *Ncs1*$^{-/-}$ mice (Figure 7E and G). Further investigations are needed to determine whether the
391 obesity phenotype singularly come from cilia defect, and how exactly dysfunction of cilia leads
392 to obesity in *Ncs1*$^{-/-}$ mice.

393 **Discussion**

394 In 1962, Sorokin described through electron micrographs that cilium biogenesis in fibroblasts is
395 initiated by attachment of a small vesicle to the distal end of the centriole (S. Sorokin, 1962), or
396 more precisely to the distal appendage of the mother centriole (Schmidt et al., 2012). Since the
397 distal appendage proteins that have been discovered so far (CEP83 (Tanos et al., 2013), CEP164

398 (Graser et al., 2007), TTBK2 (Cajanek & Nigg, 2014), SCLT1 (Tanos et al., 2013), FBF1 (Tanos
399 et al., 2013), CEP89 (Sillibourne et al., 2011), ANKRD26 (Bowler et al., 2019), LRRC45
400 (Kurtulmus et al., 2018)) lack apparent lipid binding motifs, how exactly the ciliary vesicle is
401 captured by the distal appendage is poorly understood. In an accompanying paper, we screened
402 all the previously and newly discovered distal appendage proteins and found that CEP89 is
403 important for ciliary vesicle recruitment but not for other processes of cilium formation, such as
404 IFT and CEP19 recruitment (see Figure 6 of an accompanying paper). Since CEP89 also lacks
405 any identifiable lipid binding domain, we hypothesized that an interactor of CEP89 would be
406 directly involved in the ciliary vesicle recruitment. In this paper, we discovered NCS1 as a
407 stoichiometric interactor of CEP89. We further show that NCS1 captures the ciliary vesicle via
408 its myristoylation motif.

409 **How NCS1 captures ciliary vesicles only at distal appendages?**

410 To make cilium formation efficient and error-free, we assume that the cells would have
411 mechanisms where NCS1 only captures the ciliary vesicle at the distal appendage but not at other
412 location of the cells (e.g. cytoplasm). In addition to its centriolar localization, NCS1 localizes
413 throughout cytoplasm, of which signal is completely lost in NCS1 knockout cells (Figure 2A).
414 This implies that NCS1 may sequester its myristoylation motif to remain in cytoplasm and may
415 expose the membrane association motif to capture the ciliary vesicle only at the distal
416 appendage. One very intriguing possibility is that NCS1 may protrude its myristoyl group in
417 response to increase in local calcium concentration (calcium-myristoyl switch), as shown in
418 other NCS family proteins, such as Recoverin and Hippocalcin (Ames et al., 1997; O'Callaghan
419 et al., 2003). The local calcium concentration may be higher at the centriole because of the high
420 calcium concentration in the cilium (Delling, DeCaen, Doerner, Febvay, & Clapham, 2013). We

421 addressed this question by making a series of EF-hand mutants of NCS1, where the amino acids
422 at the -z position required for calcium binding were mutated. Our data emphasizes the
423 importance of calcium in the stability of NCS1 (Figure 5-figure supplement 1A). As long as the
424 expression level of NCS1 is maintained, the mutation did not strongly affect either centriolar
425 localization or cilium formation (Figure 5-figure supplement 1B and C). These data suggest that
426 calcium may be required for the structural integrity of NCS1 but may not regulate protrusion of
427 myristoyl moiety, which is required for efficient ciliary vesicle recruitment and subsequent
428 cilium formation (Figure 5E and F). Our data aligns with the previous reports that suggest the
429 absence of calcium-myristoyl switch in NCS1 (Ames et al., 2000; O'Callaghan et al., 2002)
430 (Lemire et al., 2016). The second possibility is that NCS1 exposes its myristoyl group only when
431 the protein binds to another protein at the distal appendage. Given that CEP89 recruits NCS1 to
432 the distal appendage (Figure 2L), we wondered if NCS1 associates with membranes only when
433 the protein binds to CEP89. However, a fractionation experiment showed that NCS1 purifies
434 with the membrane fraction even in the absence of CEP89 (Figure 5A), indicating the absence of
435 CEP89-myristoyl switch. The third possibility is that NCS1 continuously expose its
436 myristoylation motif but remains in cytoplasm because of a weak membrane association. This
437 hypothesis is in agreement with the low affinity of myristoylated peptides for lipid with the
438 dissociation constant of 100 μM, which is barely sufficient to keep its membrane association
439 (Peitzsch & McLaughlin, 1993). Myristoylated proteins typically require additional mechanisms
440 to bind membranes (M. H. Wright, Heal, Mann, & Tate, 2010): 1) another acyl chain (e.g.,
441 palmitoylation), 2) a cluster of basic amino acids that help association with negatively charged
442 head group of the membrane, 3) an interacting partner that has affinity for membrane. Since
443 NCS1 does not appear to have another acyl chain, membrane binding of NCS1 is likely enhanced

444 by either basic amino acids or another distal appendage protein that is in close proximity to
445 NCS1 keeps the protein associated with membrane. Interestingly, a recent paper showed that
446 lysine residues at position 3, 7, and 9 may be also involved in membrane binding of NCS1
447 (Baksheeva et al., 2020). In terms of the binding partner induced membrane association, this
448 process is likely regulated by yet unknown distal appendage protein(s) and not by CEP89 as
449 membrane association of NCS1 does not require CEP89 (Figure 5A). The rise in the local
450 concentration of NCS1 as well as membrane vesicle at the centriole may also help NCS1's
451 membrane association at that location. The weak association between myristoylated NCS1 and
452 membrane could also explain why cells can capture ciliary vesicles, albeit less efficiently, even
453 in the absence of NCS1 (Figure 3C and 5F). We currently do not have an obvious candidate for a
454 distal appendage protein that may compensate the lack of NCS1, as the depletion of NCS1 in any
455 of the knockouts of the known distal appendage proteins did not further inhibit the ciliary vesicle
456 recruitment and cilium formation (Figure 4B-D). Future study will focus on identifying
457 additional protein(s) that recruit the ciliary vesicle to the centriole.

458 **How the ciliary vesicle is transported to the distal appendage.**

459 Our model suggests that the ciliary vesicle is recruited to the distal appendage in a microtubule-
460 dependent manner, whereas NCS1 can reach to the mother centriole without intact microtubules
461 (Figure 6). How is the ciliary vesicle recruited to the distal appendage? Classically, subdistal
462 appendages were considered as the site where the microtubule anchoring occurs, as the electron
463 micrograph showed that microtubule are in contact with the head of the subdistal appendage (see
464 Figure 12 of the (Vorobjev & Chentsov Yu, 1982)). The subdistal appendage localization of
465 Ninein, which was shown to be indispensable for microtubule anchoring at the centriole
466 (Delgehyr, Sillibourne, & Bornens, 2005), further supports that subdistal appendages are the

467 contact site of the microtubule. Therefore, one can hypothesize that the ciliary vesicle is
468 transported first to the subdistal appendage and then subsequently moves to the distal appendage
469 by an unknown mechanism. Interestingly, CEP89 and its interactors, NCS1 and C3ORF14, each
470 localize to positions near the subdistal appendage in addition to their distal appendage
471 localization (Figure 2D and F) (Chong et al., 2020). NCS1 may bind to ciliary vesicle at the
472 subdistal appendage and then move to the distal appendage to anchor the vesicle and promote
473 cilium formation. Possibly this process is rapid, so that any vesicle attached to the subdistal
474 appendage has never been observed in electron micrographs. However, this model conflicts with
475 the observation that subdistal appendages are dispensable for cilium formation (Mazo, Soplop,
476 Wang, Uryu, & Tsou, 2016). Alternatively, microtubules may populate a structural site around
477 the distal appendages as shown by recent dSTORM imaging (Chong et al., 2020). γ-tubulin
478 observed in vicinity of the distal appendage may nucleate those microtubules. If this is the case,
479 the ciliary vesicle may be transported directly to the distal appendage and then be captured by
480 NCS1. To address this question, it would be greatly informative if the entire ciliary vesicle
481 recruitment process could be visualized by super-resolution microscopy in live cells in a future
482 study. Another important question is whether NCS1 specifically recognizes a receptor on the
483 ciliary vesicle or NCS1 randomly captures the membrane of vesicles that arrive at the distal
484 appendage. NCS1 may recognize specific vesicles via the membrane curvature or specific lipid
485 components. Interestingly, a recent study showed that NCS1 preferentially binds to
486 phosphatidylinositol-3-phosphate (Baksheeva et al., 2020). This warrants future study.

487 **Requirement of NCS1 in cilium formation differs among cell types**

488 Cilium formation can be classified into two types (S. P. Sorokin, 1968) (Molla-Herman et al.,
489 2010): 1) the intracellular pathway, which is initiated by ciliary vesicle recruitment to the distal

490 appendage, and 2) the extracellular pathway, where the centriole first docks to plasma
491 membrane. While specific cell types have been observed to selectively use one of the two
492 pathways, the distinction between the pathways might not be so definite. For example, mouse
493 inner medullary collecting duct cells (mIMCD3), typically classified as using the extracellular
494 pathway, can use the intracellular pathway in less confluent cells (Stuck et al., 2021).
495 Nonetheless, the requirement for RAB34, a ciliary vesicle marker, in ciliogenesis is more
496 pronounced in the cells that use the intracellular pathway (Ganga et al., 2021; Oguchi, Okuyama,
497 Homma, & Fukuda, 2020; Stuck et al., 2021), indicating that ciliary vesicle recruitment is an
498 indispensable step for that pathway. Our data showed that cilium formation is modestly affected
499 by NCS1 depletion in the cell types that are known to use intracellular pathway (Molla-Herman
500 et al., 2010), such as RPE and MEFs (Figure 3A and Figure 7E). While the ciliogenesis pathway
501 is not well characterized in neurons, the presence of the ciliary pocket, a sign of the intracellular
502 pathway (Molla-Herman et al., 2010), is apparent in electron micrographs of neurons and neural
503 progenitors (Barnes, 1961; Brechbuhl, Klaey, & Broillet, 2008; Breunig et al., 2008; Dingemans,
504 1969; Han et al., 2008; Mirzadeh, Merkle, Soriano-Navarro, Garcia-Verdugo, & Alvarez-Buylla,
505 2008). Thus, we can predict that neurons would use the intracellular pathway. However,
506 inconsistently with RPE and MEFs, we did not observe a ciliary formation defect in cultured
507 hippocampal neurons isolated from E18.5 mice, suggesting that the requirement for NCS1 may
508 differ among cell types even though they use the same cilium formation pathway. Another
509 possible explanation for a failure to see cilium formation defects is that it is not easy to assess the
510 kinetics of ciliation in isolated hippocampal neurons because culture conditions are very different
511 from RPE cells. Notably, cilium formation is not induced by serum starvation in isolated
512 hippocampal neurons. In tissues *in vivo*, it was not easy to assess whether the *Ncs1*$^{-/-}$ mice have

513 fewer cilia than the control mice for several reasons. First, cilium structure is greatly affected by
514 sample preparation. For example, we cannot visualize cilia if we do not fix the tissues by cardiac
515 perfusion with 4% paraformaldehyde and it is difficult to achieve perfectly efficient perfusion.
516 Second, orientation of cilia is affected by the orientation of how the tissue is sectioned and it is
517 thus difficult to analyze cilia that elongate perpendicularly to the slice. Therefore, we could not
518 test whether NCS1 is required for cilium formation in cells that typically use extracellular
519 pathway. These questions warrant future studies. Importantly, we did observe a decrease in
520 ciliary localization of several membrane proteins, such as ARL13B (Figure 3-figure supplement
521 1A-C) and ADCY3 (Figure 7H) in *Ncs1*$^{-/-}$ cells, even when the percentage of ciliated cells was
522 comparable to the control cells. This may suggest that NCS1 might be involved in recruiting
523 membrane signaling proteins to the cilium besides its function in ciliary vesicle recruitment and
524 cilium formation. It would be interesting to test in the future study if other ciliary membrane
525 proteins are also brought to the cilium via ciliary vesicles.

526 ***NCS1* may be a ciliopathy gene**

527 Given that NCS1 is involved in ciliary vesicle recruitment and subsequent cilium formation, we
528 tested if *Ncs1*$^{-/-}$ mice exhibit ciliopathy phenotypes. Our data showed that *Ncs1*$^{-/-}$ mice display a
529 modest obesity phenotype, but no other apparent ciliopathy related phenotypes, including retinal
530 degeneration. The absence of retinal degeneration may be explained by the lack of Ncs1 at the
531 ciliary base in photoreceptors. A possible explanation for the lack of other ciliopathy phenotypes
532 is the partial penetrance of these other symptoms. In human, obesity and retinal degeneration is
533 observed in most Bardet-Biedl syndrome patients (-90%), whereas other phenotypes, such as
534 hypogonadism and kidney disease are often absent (Forsyth & Gunay-Aygun, 2020). Mice
535 lacking the distal appendage protein, FBF1(Zhang et al., 2021) or ANKRD26 (Acs et al., 2015)

536 (Bera et al., 2008), or the distal appendage associate protein, CEP19 (Shalata et al., 2013),
537 display morbid obesity with few other ciliopathy-related phenotypes (e.g., preweaning lethality
538 and hydrocephalus in *Fbf1*$^{-/-}$ and male infertility in *Cep19*$^{-/-}$ mice). Interestingly, our data
539 revealed that knockouts of each of these genes show a kinetic defect in ciliation, but the cells
540 also are observed to eventually catch up for cilium formation (Figure 5A and B in an
541 accompanying paper for ANKRD26 and FBF1) (Figure 3C of (Kanie et al., 2017) for CEP19).
542 This phenotype is almost identical to what was observed in CEP89 or NCS1 knockout cells
543 (Figure 3A), suggesting that mild cilium formation defect may result in obesity with few other
544 ciliopathy-related defects. Another explanation for the lack of other ciliopathy phenotypes
545 besides obesity is the background of our *Ncs1*$^{-/-}$ mice (C57BL6/J). It is well known that depletion
546 of the same gene could cause different severity of the phenotypes in different background of
547 mice. For example, mice lacking Bbip10, a BBSome associated protein (Loktev et al., 2008), in
548 pure C57BL6/J background show complete perinatal lethality, while approximately half of the
549 *Bbip10*$^{-/-}$ mice in 129/SvJ background can survive into adulthood (Loktev & Jackson, 2013).
550 Interestingly, two independent reports showed that *Ncs1*$^{-/-}$ exhibit partial (-50%) preweaning
551 lethality (Dickinson et al., 2016; Nakamura et al., 2011) in C57BL6/N mice. The difference in
552 the severity of the phenotypes in *Ncs1*$^{-/-}$ mice between previous reports and our results may be
553 explained by the difference between C57BL6/J and C57BL6/N. Genetic and phenotypic
554 differences between these two strains were extensively described in the previous paper (Simon et
555 al., 2013). Thus, NCS1 may be a ciliopathy gene and obesity caused by NCS1 depletion may be
556 attributable to ciliary defect. This warrants future genetic study. If obesity accompanied with
557 NCS1 depletion is due to a cilia defect, what kind of cilia defect exist in the *Ncs1* defective
558 animals *in vivo*? A simple defect may be the reduced number of ciliated cells because of the

559 cilium formation defect. While we did not see an apparent decrease in the number of cilia in
560 *Ncs1*$^{-/-}$ mice in any tissues that we examined (e.g., brain, kidney, pancreatic islets, and airway
561 epithelia) (Figure 7B-D, Figure 7-figure supplement 2), more accurate characterization is needed
562 to make a conclusion. It is possible that cilium formation is abolished in developmentally and
563 spatially regulated manner, so that the defect may be only apparent in specific cell types and
564 developmental stage. Another possibility that may cause cilia-related obesity phenotype in *Ncs1*$^{-}$
565 $^{/-}$ mice is that localization of some of the ciliary membrane proteins may be abolished in *Ncs1*$^{-/-}$
566 cells as shown in the cultured hippocampal neurons (Figure 7H). Unfortunately, it is not easy to
567 assess the number and morphology of the cilia as well as signal intensity of the ciliary membrane
568 proteins *in vivo* because of the issues described above. Technical improvement in the future may
569 allow us to more accurately characterize the cilia *in vivo* and determine whether ciliary defects in
570 *Ncs1*$^{-/-}$ mice indeed cause obesity. Alternatively, it would be interesting to see if *Cep89* knockout
571 mice display the similar phenotypes as *Ncs1* knockout mice.

572 **The connection between NCS1-related neurological disorder and cilia defect.**

573 NCS1 has been shown to participate in memory formation in *C. elegans* (Gomez et al., 2001) and
574 mice (Saab et al., 2009) (Nguyen et al., 2021) (Nakamura et al., 2017; Ng et al., 2016) (de
575 Rezende et al., 2014). While the neurological phenotypes in *Ncs1*$^{-/-}$ mice are not consistent
576 across studies, possibly because of the differences in mouse background, it seems that many
577 studies agree that the overall phenotypes are mild, and the mice display defects in memory
578 formation, when tested for novel object recognition (de Rezende et al., 2014) or displaced object
579 recognition (Mun et al., 2015; Ng et al., 2020; Nguyen et al., 2021). It is intriguing to consider
580 whether the memory formation defect in *Ncs1*$^{-/-}$ mice is attributable to ciliary defects. Several
581 lines of evidence suggest that loss of cilia in brain results in memory formation defects. If IFT88,

582 an IFT component critical for formation of the cilium, is depleted in telencephalon by Emx-1
583 Cre, the mice display impaired recognition memory assessed through novel object recognition
584 test (Berbari et al., 2014). The depletion of IFT20 in dentate gyrus of the hippocampus using
585 AAV-CAMKII-Cre caused the defect in displaced object recognition test (Rhee, Kirschen, Gu,
586 & Ge, 2016). Both mice lacking ADCY3 or SSTR3, ciliary membrane proteins that are
587 prominent in neurons (Bishop et al., 2007), exhibit defect in novel object recognition (Einstein et
588 al., 2010; Wang, Phan, & Storm, 2011). The similarity between cilia-defective mice and *Ncs1*$^{-/-}$
589 mice may suggest that the memory formation defect in *Ncs1*$^{-/-}$ deficient mice may be due to
590 ciliary dysfunction. It would be interesting to test whether SSTR3 agonist, which induces long-
591 term potentiation (LTP) (Einstein et al., 2010) likely via binding to the ciliary G-protein coupled
592 receptor, SSTR3, can induce LTP in *Ncs1*$^{-/-}$ mice. It would be also interesting to see if Cep89
593 depletion in mice causes similar memory formation defect, since NCS1 knockouts and CEP89
594 knockouts showed almost identical cilium formation defects (Figure 3). The importance of cilia
595 in neurological deficiencies should be an area of extensive future study.
596

597 **Author Contributions**

598 Conceptualization, T. K. and P. K. J.; Methodology, T. K., R.N., K.A., and P. K. J.;
599 Investigation, T. K., R.N., K.A., and P. K. J.; Writing – Original Draft, T. K.; Writing – Review
600 & Editing, T. K., R.N., K.A., O.P., and P. K. J.; Funding Acquisition, T.K. and P. K. J.;
601 Resources, T.K. and P. K. J.; Supervision, T. K. and P. K. J.
602

603 **Acknowledgments**

604 We thank Drs. Albert Wong and John Georgiou for providing *Ncs1* knockout mice. We thank

605 Dr. Jonathan Mulholland for technical advice on the 3D-SIM experiments. We thank Mr. John
606 Perrino for technical support for sample preparation for the electron microscopy experiments.
607 We thank members of the Jackson lab for helpful discussion and advice. 3D-SIM experiments
608 were performed at the Stanford Cell Sciences Imaging Facility and were supported by Award
609 Number 1S10OD01227601 from the National Center for Research Resources (NCRR). Electron
610 microscopy observation was performed at the Stanford Cell Sciences Imaging Facility and were
611 supported by National Institutes of Health (NIH) S10 Award Number 1S10OD028536-01, titled
612 "OneView 4kX4k sCMOS camera for transmission electron microscopy applications". The cell
613 authentication service performed by MTCRO-COBRE Cell line authentication core of the
614 University of Oklahoma Health Science Center was supported partly P20GM103639 and
615 National Cancer Institute Grant P30CA225520 of NIH. This project was support by funds from
616 the Baxter Laboratory for Stem Cell Research, the Stanford Department of Research, the
617 Stanford Cancer Center, NIH grants R01GM114276 and R01GM121565 to PKJ, NIH grant
618 P20GM103447 and a seed grant from Presbyterian Health Foundation (GRF00006006) to TK.
619

620 **Materials and Methods**

621 **Plasmids**

622 pMCB306, a lenti-viral vector containing loxP-mU6-sgRNAs-puro resistance-EGFP-loxP
623 cassette, and P293 Cas9-Blue Fluorescent Protein (BFP) were gifts from Prof. Michael Bassik.
624 Lenti-virus envelope and packaging vector, pCMV-VSV-G and pCMV-dR8.2 dvpr respectively,
625 were gifts from Prof. Bob Weinberg (Addgene plasmid #8454 and #8455).
626 pOG44 (V600520) was obtained from Thermo Fisher Scientific.

627 Lentiviral vectors containing single guide RNAs (sgRNAs) were generated by ligating 50 fmol
628 oligonucleotides encoding sgRNAs into 25 ng of the pMCB306 vector digested with BstXI
629 (R0113S, NEB) and BlpI (R0585S, NEB) restriction enzymes along with 0.25 μl of T4 ligase
630 (M0202S, NEB) in 2.5 μl total reaction volume. Before ligation, 4 μM of forward and reverse
631 oligonucleotides listed in the supplementary table were annealed in 50 μl of annealing buffer
632 (100 mM potassium acetate, 30 mM HEPES (pH7.4), and 3mM magnesium acetate) at room
633 temperature following denaturation in the same buffer at 95°C for 5 minutes. The targeting
634 sequence for sgRNAs are listed in the supplementary table "Source Data 1-Primers used for
635 genomic PCR and for generating sgRNA vectors". The guide RNA targeting sequence for
636 pMCB306-sgNCS1 vector used to create cells lacking both NCS1 and each of the other distal
637 appendage proteins shown in Figure 4 is the same as the one used to make NCS1 knockout cells.
638 The knockout cells for other distal appendage proteins were described in an accompanying
639 paper.
640 pG-LAP6/puro vector (pCDNA5/TO/FRT/EGFP-TEV cleavage site-S tag-PreScission cleavage
641 site/DEST) used for the tandem affinity purification experiment was previously described (Kanie
642 et al., 2017). Gateway cloning compatible lentiviral vectors, pWPXLd/LAP-N/puro/DEST vector
643 and pWPXLd/LAP-C/puro/DEST vector, were previously described (Kanie et al., 2017).
644 pWPXLd/LAP-N/blast/long EF/DEST was created by inserting N-terminally LAP tag (EGFP-
645 TEV cleavage site-S tag-PreScission cleavage site)/DEST/blasticidin resistance cassette into a
646 second generation lenti-viral vector, pWPXLd. pWPXLd vector was a gift from Prof. Didier
647 Trono (Addgene plasmid #12258). pWPXLd/LAP-C/blast/long EF/DEST vector was created by
648 inserting DEST/C-terminally LAP tag/blasticidin resistance cassette into the pWPXLd vector.
649 pWPXLd/FLAG-N/blast/DEST vector was created by inserting FLAG/DEST/blasticidin

650 resistance cassette into the pWPXLd vector. All the lenti-viral vectors were propagated in Stbl3
651 competent cells to reduce unwanted recombination of long terminal repeat of the vectors.
652 pCS2-N-terminal 5×MYC/DEST and pCS2-N-terminal 3×HA/DEST (used for in vitro
653 translation) were created by inserting either 5×MYC tag or 3×HA tag and destination cassette
654 into pCS2+ vector, which contains Sp6 and CMV promoter.
655 The Gateway entry vector for Homo sapiens CEP89 was created by BP recombination using a
656 Polymerase Chain Reaction (PCR) product containing attB1 and attB2 site, which was amplified
657 using pCR4-TOPO-CEP89 (MHS6278-213243472, Open Biosystems) as a template. Gateway
658 entry vectors carrying truncation mutants of CEP89 (1-343a.a. and 344-783a.a.) were created by
659 using BP recombination between pDONR221 and PCR-amplified inserts.
660 The Gateway entry vectors for Homo sapiens NCS1 (HsCD00366520) and C3ORF14
661 (HsCD00365881) were obtained from Harvard plasmid. STOP codons were added or removed
662 by using Quick change mutagenesis if necessary. The Gateway entry vectors for NCS1 mutants
663 (myristoylation defective or EF-hand mutants) were created via Quick change mutagenesis using
664 the entry vector for NCS1 described above. The quick-change mutagenesis was performed by
665 PCR with a complementary primary set (forward and reverse) that has a point mutation in the
666 middle of the primers. Following the PCR, the PCR product was treated with 20U of DpnI
667 (R0176L, NEB) for 1 hour at 37°C to eliminate the template, and was then used to transform
668 competent cells.
669 The entry vectors for the CEP350 fragment (2470-2836 a.a.) and FGFR1OP (or FOP) was
670 previously described (Kanie et al., 2017).
671 Flp-In system compatible N-terminally LAP-tagged CEP89 was generated by LR recombination
672 between CEP89 entry vector and pG-LAP6/puro.

673 Lentiviral vector containing untagged CEP89 (minimal CMV promoter) was created by LR
674 recombination between CEP89 entry vector that contains a stop codon and
675 pWPXLd/LAPC/blast/minimal CMV/DEST vector.
676 Lentiviral vectors containing untagged NCS1 (long EF promoter or short EF promoter) were
677 created by LR recombination between NCS1 (wild-type and mutants) entry vectors that contain
678 stop codons and pWPXLd/LAPC/blast/long EF/DEST or pWPXLd/LAPC/blast/short EF/DEST
679 vectors.
680 N-terminally HA tagged CEP89, C3ORF14, and FGFR1OP (or FOP) vectors used for in vitro
681 binding assay were created by LR recombination between the respective entry vectors containing
682 a stop codon and the pCS2-N-terminal 3×HA/DEST vector. pCS2-N-terminal 5×MYC tagged
683 C3ORF14, NCS1, and the CEP350 fragment (2470-2836 a.a.) vectors were created by LR
684 recombination between the respective entry vectors that contain stop codons and the pCS2-N-
685 terminal 5×MYC/DEST vector.
686
687 **Cell line, Cell culture, Transfection, and Lentiviral expression**
688 hTERT RPE-1 cells and 293T cells were grown in DMEM/F-12 (12400024, Thermo Fisher
689 Scientific) supplemented with 10% FBS (100-106, Gemini), 1× GlutaMax (35050-079, Thermo
690 Fisher Scientific), 100 U/mL Penicillin-Streptomycin (15140163, Thermo Fisher Scientific) at
691 37°C in 5% CO_2. To induce cilium formation, cells were incubated in DMEM/F-12
692 supplemented with 1×GlutaMax and 100 U/mL Penicillin-Streptomycin (serum-free media).
693 Both cell lines were authenticated via a short-tandem-repeat based test. The authentication was
694 performed by MTCRO-COBRE Cell line authentication core of the University of Oklahoma
695 Health Science Center. Mycoplasma negativity of the original cell lines (hTERT RPE-1 and

696 293T) grown in antibiotics-free media were confirmed by a PCR based test (G238, Applied
697 Biological Materials).
698 RPE-FRT9 expressing N-terminally LAP tagged CEP89 used for tandem affinity purification
699 was generated by transfecting 150 ng of the preceding vectors with 850 ng of pOG44, followed
700 by selection with 10 μg/ml puromycin. Flp-In system compatible RPE cells (RPE-FRT9) were
701 previously described (Sang et al., 2011).
702 All other stable cell lines, including CRISPR knockout cells, were generated using lentivirus.
703 Lentivirus carrying either gene of interest or sgRNAs was produced by co-transfecting 293T
704 cells with 150 ng of pCMV-VSV-G, 350 ng of pCMV-dR8.2 dvpr, and 500 ng of lenti-viral
705 transfer plasmids previously described along with 3 μl of Fugene 6 (E2692, Promega)
706 transfection reagent. Media was replaced 24 hr after transfection to omit transfection reagent,
707 and virus was harvested at 48 hr post-transfection. Virus was then filtered with a 0.45 μm PVDF
708 filter (SLHV013SL, Millipore) and mixed with 4-fold volume of fresh media containing 12.5
709 μg/ml polybrene (TR-1003-G, Millipore). Following infection for 66 hr, cells were selected with
710 either 10 μg/ml puromycin (P9620, SIGMA-Aldrich) or 10 μg/ml blasticidin (30-100-RB,
711 Corning) for at least 10 days before subsequent analysis.
712

713 **CRISPR knockout**

714 RPE cells expressing BFP-Cas9 were generated by infection with lentivirus carrying P293 Cas9-
715 BFP, followed by sorting BFP-positive cells using FACSAria (BD). RPE-BFP-Cas9 cells were
716 then infected with lentivirus carrying sgRNAs in the pMCB306 vector to generate knockout
717 cells. After selection with 10 μg/ml puromycin, cells were subjected to immunoblotting,
718 immunofluorescence, or genomic PCR combined with TIDE analysis (Brinkman, Chen,

719 Amendola, & van Steensel, 2014) to determine knockout efficiency. The exact assay used for
720 each cell line is listed in "Source Data 7-summary of CRISPR knockout cells". Cells were then
721 infected with adenovirus carrying Cre-recombinase (1045N, Vector Biolabs) at a multiplicity of
722 infection of 50 to remove the sgRNA-puromycin resistance-EGFP cassette. 10 days after
723 adenovirus infection, GFP-negative single cells were sorted using FACSAria. The single cell
724 clones were expanded, and their knockout efficiency were determined by immunofluorescence,
725 Western blot, and/or genomic. The same number of validated single clones (typically three to
726 four different clones) were mixed to create pooled single cell knockout clones to minimize the
727 phenotypic variability occurred in single cell clones. The cells lacking both NCS1 and each of
728 the other distal appendage proteins shown in Figure 4 were created by infecting the knockout
729 cells with lenti-virus carrying sgNCS1. The experiments shown in Figure 4 were performed
730 without removing loxP-mU6-sgRNAs-puro resistance-EGFP-loxP cassette.
731 Cells used in the rescue experiments shown in Figure 3B, Figure 3- figure supplement 1A-C,
732 Figure 5A-F, and Figure 5- figure supplement 1A-C were created by infecting the respective
733 knockout cells with lenti-virus carrying untagged CEP89 or NCS1 (wild-type or mutants). To
734 rescue the ciliation defect of CEP89 knockout cells, the expression level of CEP89 was carefully
735 adjusted by using minimal CMV promoter to mimic endogenous CEP89 expression, since
736 overexpression of CEP89 under the control of long EF promoter significantly inhibited cilium
737 formation (data not shown).
738

739 **Tandem affinity purification**

740 5 mL packed cell volume of RPE-FRT9 cells expressing N-terminally LAP-tagged CEP89 were
741 re-suspended with 20 mL of LAP-resuspension buffer (300 mM KCl, 50 mM HEPES-KOH [pH

742 7.4], 1 mM EGTA, 1 mM $MgCl_2$, 10% glycerol, 0.5 mM dithiothreitol (DTT), and protease
743 inhibitors [PI88266, Thermo Scientific]), lysed by gradually adding 600 μL 10% NP-40 to a
744 final concentration of 0.3%, then incubated on ice for 10 min. The lysate was first centrifuged at
745 14,000 rpm (27,000 g) at 4°C for 10 min, and the resulting supernatant was centrifuged at 43,000
746 rpm (100,000 g) for 1 hr at 4°C to further clarify the lysate. High speed supernatant was mixed
747 with 500 μL of GFP-coupled beads (Torres, Miller, & Jackson, 2009) and rotated for 1 hr at 4°C
748 to capture GFP-tagged proteins, and washed five times with 1 mL LAP200N buffer (200 mM
749 KCl, 50 mM HEPES-KOH [pH 7.4], 1 mM EGTA, 1 mM $MgCl_2$, 10% glycerol, 0.5 mM DTT,
750 protease inhibitors, and 0.05% NP40). After re-suspending the beads with 1 mL LAP200N buffer
751 lacking DTT and protease inhibitors, the GFP-tag was cleaved by adding 5 μg of TEV protease
752 and rotating tubes at 4°C overnight. All subsequent steps until the cutting of bands from protein
753 gels were performed in a laminar flow hood. TEV-eluted supernatant was added to 100 μL of S-
754 protein agarose (69704-3, EMD Millipore) to capture S-tagged protein. After washing three
755 times with LAP200N buffer lacking DTT and twice with LAP100 buffer (100 mM KCl, 50 mM
756 HEPES-KOH [pH 7.4], 1 mM EGTA, 1 mM $MgCl_2$, and 10% glycerol), purified protein
757 complexes were eluted with 50 μL of 2×Lithium Dodecyl Sulfate (LDS) buffer (212 mM Tris-
758 HCl, 282 mM Tris-base, 4% LDS, 20% glycerol, 1.02 mM EDTA, 0.13% Brilliant Blue G250,
759 0.05% phenol red buffer) containing 10% DTT and boiled at 95°C for 3 min. Samples were then
760 run on Bolt® Bis-Tris Plus Gels (NW04120BOX, Thermo Fisher Scientific) in Bolt® MES SDS
761 Running Buffer (B000202, Thermo Fisher Scientific). Gels were fixed in 100 mL of fixing
762 solution (50% methanol, 10% acetic acid in Optima™ LC/MS grade water [W6-1, Thermo
763 Fisher Scientific]) at room temperature, and stained with Colloidal Blue Staining Kit (LC6025,
764 Thermo Fisher Scientific). After the buffer was replaced with Optima™ water, the bands were

765 cut into eight pieces, followed by washing twice with 500 μL of 50% acetonitrile in Optima™
766 water. The gel slices were then reduced and alkylated followed by destaining and in-gel
767 digestion using 125 ng Trypsin/LysC (V5072, Promega) as previously described (Shevchenko,
768 Tomas, Havlis, Olsen, & Mann, 2006) with the addition of Protease Max (V2071, Promega) to
769 increase digestion efficiency. Tryptic peptides were extracted from the gel bands and dried in a
770 speed vac. Prior to LC-MS, each sample was reconstituted in 0.1% formic acid, 2% acetonitrile,
771 and water. NanoAcquity (Waters) LC instrument was set at a flow rate of either 300 nL/min or
772 450 nL/min where mobile phase A was 0.2% formic acid in water and mobile phase B was 0.2%
773 formic acid in acetonitrile. The analytical column was in-house pulled and packed using C18
774 Reprosil Pur 2.4 μM (Dr. Maisch) where the I.D. was 100 μM and the column length was 20-25
775 cm. Peptide pools were directly injected onto the analytical column in which linear gradients (4-
776 40% B) were of either 80 or 120 min eluting peptides into the mass spectrometer. Either the
777 Orbitrap Elite or Orbitrap Fusion mass spectrometers were used, where a top 15 or "fastest"
778 MS/MS data acquisition was used, respectively. MS/MS was acquired using CID with a
779 collisional energy of 32-35. In a typical analysis, RAW files were processed using Byonic
780 (Protein Metrics) using 12 ppm mass accuracy limits for precursors and 0.4 Da mass accuracy
781 limits for MS/MS spectra. MS/MS data was compared to an NCBI GenBank FASTA database
782 containing all human proteomic isoforms with the exception of the tandem affinity bait construct
783 sequence and common contaminant proteins. Spectral counts were assumed to have undergone
784 fully specific proteolysis and allowing up to two missed cleavages per peptide. All data was
785 filtered and presented at a 1% false discovery rate (Elias & Gygi, 2007).
786
787 **Silver staining**

788 5μl of samples containing LDS buffer and DTT prepared for tandem affinity purification and
789 mass spectrometry described above were mixed with 0.5 μl of 500 mM iodoacetamide
790 (0210035105, MP Biomedicals). Proteins were separated in a 4-12% Bis-Tris gel (NP0321BOX,
791 Invitrogen), followed by fixation of the gel overnight in 50% methanol at room temperature.
792 The gel was impregnate with solution C (0.8% (w/v) silver nitrate (S6506, SIGMA), 207.2mM
793 ammonium hydroxide (A6899, SIGMA) and 18.9 mM sodium hydroxide) for 15 minutes,
794 followed by rinsing with water twice. The image was then developed in solution D (0.05% citric
795 and 0.0185% formaldehyde in Milli-Q) until intensity of the bands increase to optimal level. The
796 reaction was then terminated by adding stop solution (45% methanol and 10% acetic acid).
797

798 **Immunoblot**

799 For immunoblotting, cells were lysed in NP-40 lysis buffer (50 mM Tris-HCl [pH7.5], 150 mM
800 NaCl, 0.3% NP-40 [11332473001, Roche Applied Science]) containing 10 μg/ml LPC
801 (leupeptin, Pepstatin A, and chymostatin) and 1% phosphatase inhibitor cocktail 2 (P5726,
802 SIGMA). Following clarification of the lysate by centrifugation at 15,000 rpm (21,000 g) for 10
803 min, samples were mixed with 1× LDS buffer (106 mM Tris-HCl, 141 mM Tris-base, 2% LDS,
804 10% glycerol, 0.51mM EDTA, 0.065% Brilliant Blue G250, 0.025% phenol red) containing
805 2.5% 2-mercaptoethanol (M3148, SIGMA) and incubated at 95°C for 5 min. Proteins were
806 separated in an NuPAGE™ Novex™ 4-12% Bis-Tris protein gel (WG1402BOX, Thermo Fisher
807 Scientific) in NuPAGE™ MOPS SDS running buffer (50 mM MOPS, 50 mM Tris Base, 0.1%
808 SDS, 1 mM EDTA, pH 7.7), and transferred onto an Immobilon™-FL PVDF Transfer
809 Membrane (IPFL00010, EMD Millipore) in Towbin Buffer (25 mM Tris, 192 mM glycine, pH
810 8.3). Membranes were incubated in LI-COR Odyssey Blocking Buffer (NC9232238, LI-COR)

811 for 30 min at room temperature, and then probed overnight at 4°C with the appropriate primary
812 antibody diluted in the blocking buffer. Next, the membrane was washed 3 × 5 min in TBST
813 buffer (20 mM Tris, 150 mM NaCl, 0.1% Tween 20, pH 7.5) at room temperature, and incubated
814 with the appropriate IRDye® antibodies (LI-COR) diluted in the blocking buffer for 30 min at
815 room temperature. After washing three times in TBST buffer, the membrane was scanned on an
816 Odyssey CLx Imaging System (LI-COR) and proteins were detected at wavelengths 680 and 800
817 nm. Primary antibodies used for immunoblotting are listed in the "Source Data 4-List of the
818 antiboidies_CEP89-NCS1". Secondary antibodies used for immunoblotting were IRDye®
819 800CW donkey anti-rabbit (926-32213, LI-COR) and IRDye® 680CW donkey anti-mouse (926-
820 68072, LI-COR).
821
822 **Co-immunoprecipitation**
823 Cells were plated in a 10 cm dish and grown to confluent. Cells were then lysed with NP-40 lysis
824 buffer (50 mM Tris-HCl [pH7.5], 150 mM NaCl, and 0.3% NP-40) containing 10 μg/ml LPC
825 (leupeptin, Pepstatin A, and chymostatin) and 1% phosphatase inhibitor cocktail 2 (P5726,
826 SIGMA), followed by clarification of the lysate by centrifugation at 15,000 rpm (21,000 g) for
827 10 min. The protein concentration was measured by Bradford assay as described previously (see
828 procedure B step 8 in (Kanie & Jackson, 2018)). For GFP co-immunoprecipitation shown in
829 Figure 1D and Figure 5- figure supplement 1A, the soluble fraction was incubated with Protein A
830 beads cross-linked with rabbit anti-GFP antibody (Torres et al., 2009) (10 μl bed volume per 3
831 mg of lysate) with end-over-end rotation for 1.5 hr at 4°C. For co-immunoprecipitation with
832 endogenous NCS1 shown in Figure 1- figure supplement 1A, the lysate was incubated with
833 mouse monoclonal anti-NCS1 antibody (sc-376206, Santa Cruz) (1 μg of antibody per 4 mg of

834 lysate) for 1 hour with end-over-end rotation. The samples were then mixed with protein A beads
835 (20 μl bed volume) and incubated with end-over-end rotation for 1.5 hr at 4°C. After the
836 incubation with the beads (for both GFP co-IP and NCS1 co-IP), the samples were washed five
837 times with IP wash buffer (50 mM Tris-HCl [pH 7.5], 150 mM NaCl, and 0.1% NP-40). Samples
838 were then eluted with 2 × LDS buffer containing 2.5% 2-mercaptoethanol (M3148, SIGMA).
839

840 **Subcellular fractionation**

841 Cells were plated in a 15 cm dish at the density of 1.25×10^6 cells and grown in DMEM/F-12
842 media containing 10% FBS for 90 hours. Cells were detached from the plate using 0.05%
843 trypsin/EDTA (25300-054, Gibco) and pelleted down by centrifugation at 500 g at 4°C for 5
844 minutes. After washing once with 15 ml of ice cold low osmotic buffer (25mM HEPES-NaOH
845 (pH7.5), 0.5 mM $MgCl_2$), the cell pellet was re-suspended in 10 ml of the ice cold low osmotic
846 buffer and incubated on ice for 10 minutes to let the cells swollen. The swollen cells were
847 pelleted down and were re-suspended in 0.8 ml of the ice cold low osmotic buffer, followed by
848 nitrogen cavitation at 300 psi for 30 minutes on ice. The cavitate was centrifuged at 1000 g at
849 4°C for 10 minutes. The 1000 g supernatant was then centrifuged at 15,000 g at 4°C for 10
850 minutes. The 15,000 g supernatant was then transferred to an ultracentrifugation tube (343778,
851 Beckman) and ultracentrifuged at 100,000 g (R_{max}) in a TLA100.2 fixed angle rotor (Beckman) at
852 4°C for 1 hour. The supernatant samples were prepared by mixing 25 μl of supernatant from
853 each centrifugation speed with 25 μl of 2×LDS buffer containing 5% 2-mercaptoethanol. The
854 pellet samples were prepared by re-suspending the pellet with appropriate amount of 1× LDS
855 buffer containing 2.5% 2-mercaptoethanol.
856

857 ***In vitro* binding assay**

858 *Co-In vitro* translated (co-IVT) proteins were generated with pCS2-N-terminal 5×MYC vectors
859 and pCS2-N-terminal 3×HA vectors described above using TnT® Coupled Reticulocyte Lysate
860 System under the SP6 promoter (L4600, Promega) and by following manufacturer's
861 recommendations with few modifications. Briefly, instead of in vitro translating 1μg of plasmid
862 for each reaction, 0.5μg of HA-tagged protein along with 0.5μg of corresponding MYC-tagged
863 protein was co-translated. Note that we only observed the interaction between CEP89 and NCS1
864 when the two proteins were co-translated. The interaction between all the other proteins were
865 identical between original protocol and co-IVT. For each pull-down reaction, 50 μl of co-IVT
866 protein was added along with 5 μL (bed volume) of washed HA-beads (11815016001, Roche) in
867 300 μL binding buffer (25 mM HEPES-NaOH [pH 7.5], 500 mM NaCl, 1 mM CaCl2, and 0.1%
868 Triton X-100) and mixed for 2 hours at 4°C. The beads were washed five times with the same
869 buffer and eluted with 1×LDS buffer containing 2.5% 2-mercaptoethanol. The eluates were then
870 resolved by SDS-PAGE and analyzed by immunoblotting with anti-HA (901501, BioLegend)
871 and anti-MYC (ab9106, Abcam) antibodies.

872

873 **Transmission electron microscopy**

874 Either control (sgGFP) or NCS1 knockout RPE cells were grown to confluent on 12 mm round
875 coverslips (12-545-81, Fisher Scientific), followed by serum starvation for 3 hr. Cells were then
876 fixed with 4% paraformaldehyde (PFA) (433689M, Alfa Aesar) and 2% glutaraldehyde (G7526,
877 SIGMA) in sodium cacodylate buffer (100 mM sodium cacodylate and 2 mM $CaCl_2$, pH 7.4) for
878 1 hr at room temperature, followed by two washes with sodium cacodylate buffer. Cells were
879 then post fixed in cold/aqueous 1% osmium tetroxide (19100, Electron Microscopy Sciences) in

880 Milli-Q water for 1 hour at 4°C, allowed to warm to room temperature (RT) for 2 hours rotating
881 in a hood, and washed three times with Milli-Q water. The samples were then stained with 1%
882 uranyl acetate in Milli-Q water at room temperature overnight. Next, the samples were
883 dehydrated in graded ethanol (50%, 70%, 95%, and 100%), followed by infiltration in EMbed
884 812. Ultrathin serial sections (80 nm) were created using an UC7 (Leica, Wetzlar, Germany), and
885 were picked up on formvar/Carbon coated 100 mesh Cu grids, stained for 40 seconds in 3.5%
886 Uranyl Acetate in 50% Acetone followed by staining in Sato's Lead Citrate for 2 minutes.
887 Electron micrographs were taken on JEOL JEM1400 (120kV) equipped with an Orius 832
888 digital camera with 9 μm pixel (Gatan). To test the percentage of the ciliary vesicle positive
889 centriole, multiple serial sections (typically 3-4) were analyzed per each mother centriole, as
890 ciliary vesicles are often not attached to all nine blades of the distal appendage (i.e., ciliary
891 vesicles are often not found in all the sections of the same mother centriole).
892
893 **Immunofluorescence**
894 For wide-field microscopy, cells were grown on acid-washed 12 mm #1.5 round coverslips
895 (72230-10, Electron Microscopy Sciences) and fixed either in 4% paraformaldehyde (433689M,
896 Alfa Aesar) in phosphate buffered saline (PBS) for 15 min at room temperature or in 100%
897 methanol (A412-4, Fisher Scientific) for 5 min at -20°C. The primary antibodies used for
898 immunofluorescence are listed in the "Source Data 4-List of the antiboidies_CEP89-NCS1". All
899 staining condition such as fixation condition and dilution of the antibodies can be found in the
900 source data of each figure. After blocking with 5% normal serum that are matched with the
901 species used to raise secondary antibodies (005-000-121 or 017-000-121, Jackson
902 ImmunoResearch) in immunofluorescence (IF) buffer (3% bovine serum albumin (BP9703100,

903 Fisher Scientific), 0.02% sodium azide (BDH7465-2, VWR International), and 0.1% NP-40 in
904 PBS) for 30 min at room temperature, cells were incubated with primary antibody in IF buffer
905 for at least 3 hr at room temperature, followed by rinsing with IF buffer five times. The samples
906 were then incubated with fluorescent-labeled secondary antibody (listed below) in IF buffer for 1
907 hr at room temperature, followed by rinsing with IF buffer five times. After nuclear staining with
908 4',6-diamidino-2-phenylindole (DAPI) (40043, Biotium) in IF buffer at a final concentration of
909 0.5 μg/ml, coverslips were mounted with Fluoromount-G (0100-01, SouthernBiotech) onto glass
910 slides (3050002, Epredia). Images were acquired on an Everest deconvolution workstation
911 (Intelligent Imaging Innovations) equipped with a Zeiss Axio Imager Z1 microscope and a
912 CoolSnap HQ cooled CCD camera (Roper Scientific). A 40x NA1.3 Plan-Apochromat objective
913 lens (420762-9800, Zeiss) was used for ciliation assays, and a 63x NA1.4 Plan-Apochromat
914 objective lens (420780-9900, Zeiss) was used for other analyses.
915 For ciliation assays, cells were plated into a 6-well plate at a density of 2 x 10^5 cells/well and
916 grown for 66 hr. Cells were serum starved for 24 hr unless otherwise indicated and fixed in 4%
917 PFA. In the experiments presented in Figure 3A, the cells were incubated in serum free media for
918 12, 24, 48, 72, or 96 hours before fixation. After the blocking step, cells were stained with anti-
919 ARL13B (17711-1-AP, Proteintech), anti-CEP170 (41-3200, Invitrogen), and anti-acetylated
920 tubulin (Ac-Tub) antibodies (T7451, SIGMA), washed, then stained with anti-rabbit Alexa Fluor
921 488 (711-545-152, Jackson ImmunoResearch), goat anti-mouse IgG1-Alexa Fluor 568 (A-
922 21124, Invitrogen), and goat anti-mouse IgG2b Alexa Fluor 647 (A-21242, Invitrogen). All the
923 images were captured by focusing CEP170 without looking at a channel of the ciliary proteins to
924 avoid selecting specific area based on the percentage of ciliated cells. The structures extending
925 from the centrosome and positive for ARL13B with the length of more than 1 μm was counted as

926 primary cilia. At least 6 images from different fields per sample were captured for typical
927 analysis. Typically, at least 200 cells were analyzed per experiment. Exact number of cells that
928 we analyzed in each sample can be found in the Source Data of corresponding figures. The
929 percentage of ciliated cells were manually counted using the SlideBook software (Intelligent
930 Imaging Innovations).
931 For ciliary vesicle recruitment assays, cells were plated into a 6-well plate at a density of 2 x 10^5
932 cells/well, grown for 66 hr (without serum starvation), and fixed in 4% PFA. After the blocking
933 step, cells were stained with anti-RAB34 (27435-1-AP, Proteintech), anti-Myosin Va (sc-
934 365986, Santa Cruz), and anti-CEP170 (to mark centriole) antibodies (41-3200, Invitrogen),
935 washed, and then stained with goat anti-mouse IgG2a Alexa Fluor 488 (A-21131, Proteintech),
936 goat anti-rabbit Alexa Fluor 568 (A10042, Invitrogen), and goat anti-mouse IgG1 Alexa Fluor
937 647 (A-21240, Invitrogen). All the images were captured by focusing CEP170 without looking at
938 a channel of the ciliary vesicle markers to avoid selecting specific area based on the percentage
939 of ciliary vesicle positive centrioles. At least eight images from different fields per sample were
940 captured for typical analysis. Typically, at least 50 cells were analyzed per experiment. Exact
941 number of cells that we analyzed in each sample can be found in the Source Data of
942 corresponding figures.
943 For CP110 removal assays, cells were plated into a 6-well plate at a density of 2 x 10^5 cells/well
944 and grown for 66 hr. Cells were serum starved for 24 hr in 100% methanol. After the blocking
945 step, cells were stained with anti-CP110 (12780-1-AP, Proteintech), anti-FOP (H00011116-M01,
946 Abnova) (to mark both mother and daughter centrioles), and anti-CEP164 (sc-515403, Santa
947 Cruz) (to mark the mother centriole) antibodies, washed, then stained with anti-rabbit Alexa
948 Fluor 488 (711-545-152, Jackson ImmunoResearch), goat anti-mouse IgG2a-Alexa Fluor 568

949 (A-21134, Invitrogen), and goat anti-mouse IgG2b Alexa Fluor 647 (A-21242, Invitrogen). All
950 the images were captured by focusing FOP without looking at a channel of the other centriolar
951 proteins to avoid selecting specific area based on the percentage of CP110 positive centrioles.
952 CP110 localizing to both mother and daughter centrioles (as judged by colocalization with FOP)
953 were counted as two dots, and CP110 localizing only to daughter centriole (as judged by no
954 colocalization with CEP164) was counted as a one dot. Exact number of cells that we analyzed
955 in each sample can be found in the Source Data of corresponding figures.
956
957 For structured illumination microscopy, cells were grown on 18 mm square coverslips with the
958 thickness of 0.17 mm (474030-9000-000, Zeiss), fixed, and stained as described above. DAPI
959 staining was not included for the structured illumination samples. Coverslips were mounted with
960 SlowFade Gold Antifade Reagent (S36936, Life Technologies). Images were acquired on a
961 DeltaVision OMX V4 system equipped with a 100×/1.40 NA UPLANSAPO100XO objective
962 lens (Olympus), and 488 nm (100 mW), 561 nm (100 mW), and 642 nm (300 mW) Coherent
963 Sapphire solid state lasers and Evolve 512 EMCCD cameras (Photometrics). Image stacks of 2
964 μm z-steps were taken in 0.125 μm increments to ensure Nyquist sampling. Images were then
965 computationally reconstructed and subjected to image registration by using SoftWoRx 6.5.1
966 software.
967 Secondary antibodies used for immunofluorescence were donkey anti-rabbit Alexa Fluor 488
968 (711-545-152, Jackson ImmunoResearch), donkey anti-Chicken IgY Alexa Fluor 488 (703-545-
969 155, Jackson ImmunoResearch), donkey anti-mouse IgG DyLight 488 (715-485-150, Jackson
970 ImmunoResearch), goat anti-mouse IgG2a Alexa Fluor 488 (A-21131, Thermo Fisher
971 Scientific), goat anti-mouse IgG_1 Alexa Fluor 488 (A-21121, Thermo Fisher Scientific), donkey

anti-rabbit IgG Alexa Fluor 568 (A10042, Thermo Fisher Scientific), goat anti-mouse IgG2a-Alexa Fluor 568 (A-21134, Thermo Fisher Scientific), goat anti-mouse IgG1-Alexa568 (A-21124, Thermo Fisher Scientific), goat anti-mouse IgG2b Alexa Fluor 647 (A-21242, Thermo Fisher Scientific), goat anti-mouse IgG1 Alexa Fluor 647 (A-21240, Thermo Fisher Scientific), donkey anti-rabbit IgG Alexa Fluor 647 (711-605-152, Jackson ImmunoResearch).

Mice

Ncs1$^{-/-}$ mice in a C57BL/6J background were originally generated by the lab of Olaf Pongs (Hermainski, 2012) and the strategy for the gene targeting was previously described (Ng et al., 2016). Briefly, the 129 strain derived R1 embryonic stem cells carrying the targeting cassette was injected into C57BL/6J blastocysts. The resulting *Ncs1*$^{-/-}$ mice, which lack exon 4-7 of *Ncs1*, were backcrossed to C57BL/6J over 10 generations. The backcrossed mice were re-derived and maintained at the Toronto Centre for Phenogenomics until they were transferred to Stanford University.

All mice were maintained under specific pathogen-free conditions at the Stanford animal care facility. All experiments were approved by Administrative Panel on Laboratory Animal Care at Stanford University (Institutional Animal Care and Use Committee protocol number: 28556). The primers used for genotyping PCR are mNCS1_genotyping-F: 5'-GTCCACCCATACCAATCACT -3', mNCS1_genotyping_WT-R: 5'-ACAGAGAATCCAAAGCCAGC-3', mNCS1_genotyping_KO-R: 5'-TTGTGCTGGAGAAGGGAGAG-3'. The bands observed by PCR amplifications are 398 bp and 514 bp for wild-type and knockout mice respectively.

994 The term “littermate controls” used in this paper means that the mice were born from the same
995 mother on the same day and were housed in the same cage as the test animals throughout the life.
996
997 Assessment of viability of *Ncs1*$^{-/-}$ mice
998 To test viability of *Ncs1*$^{-/-}$ mice, *Ncs1*$^{+/-}$ female and male mice were mated, and genotype of the
999 offspring was examined by genomic PCR using the genotyping PCR primers described above at
1000 P21.
1001
1002 Body weight measurement
1003 The body weight of male or female *Ncs1*$^{-/-}$ mice and their littermate controls were measured
1004 weekly between 9 am-12 pm. The statistics was obtained through 2-way ANOVA with Tukey’s
1005 multiple comparisons test. All the raw data can be available in Figure 8B-Source Data.
1006
1007 Measurement of fat weight
1008 20 week old *Ncs1*$^{-/-}$ and their litter mate *Ncs1*$^{+/-}$ mice were anesthetized with isoflurane and
1009 euthanized by cervical dissociation. Inguinal or epididymal fat was then dissected out from the
1010 mice and were measured on a scale.
1011
1012 Preparation, staining, and imaging of the tissue samples.
1013 6- to 8-week-old *Ncs1*$^{-/-}$ or their litter mate control animals were first anesthetized with 3%
1014 isoflurane (Fluriso, Bet-one) at a delivery rate of 1L/min. Complete anesthesia was confirmed by
1015 checking toe pinch reflex, and the animal was kept anesthetized throughout the procedure using a
1016 face mask that is connected to the anesthesia machine (VetEquip). Following exposure of the

1017 heart, an incision was made in the right atrium. Next, 27G½ gage needle (305109, BD)
1018 connected to a 20 ml syringe (302830, BD) was inserted into the left ventricle to transcardially
1019 perfuse the animal with 20 ml of PBS followed by 1.5 ml/g (-35 ml) of 4% (v/v)
1020 paraformaldehyde (PFA) (15710, Electron Microscopy Sciences). Note that the transcardial
1021 perfusion of 4% PFA is critical to preserve the sample to visualize primary cilia in tissues. The
1022 fixed tissues were dissected out and post-fixed in 20 ml of 100% methanol at -20°C for 20 hours.
1023 We found that the post fixation in methanol is critical for Ncs1 visualization in tissues likely
1024 through washing out the PFA from the tissue, since over-fixation of the samples in PFA greatly
1025 diminished the centrosomal signal of Ncs1 in monolayer cultured cells (data not shown). The
1026 post-fixed tissues were then submerged in graded concentration (10-20-30% (w/v)) of sucrose
1027 (S9378, SIGMA Aldrich) in PBS at 4°C until the tissue sunk in each solution to cryoprotect the
1028 samples. The tissues were then embedded into OCT compound (4583, Tissue-Tek). Cryosections
1029 (typically 7-10 μm thickness) were created on a Cryostat (3050S, Leica) and the sliced tissues
1030 were collected on adhesive microscope slides (16005-110, VWR). Samples were immunostained
1031 using the same procedure as the one used for wide-field microscopy experiments. The stained
1032 samples were imaged on the Marianas SDC spinning disk microscope (Intelligent Imaging
1033 Innovations) equipped with Cascade 1K camera (photometrics) and CSU22 confocal scanner
1034 unit (Yokogawa). A 63x NA1.4 Plan-Apochromat objective lens (420781-9910-000, Zeiss) was
1035 used to acquire images. Typically, image stacks of 10 -20 μm z-steps were taken in 0.5 μm
1036 increments.
1037
1038 <u>HE stains</u>

1039 20, 30, or 50 weeks old *Ncs1*$^{-/-}$ mice and their littermate controls were first fixed by transcardial
1040 perfusion of 4% PFA as described above and post-fixed in 4% PFA at 4°C for 72 hours. Tissues
1041 were then processed, embedded in paraffin blocks, sectioned on a microtome, and stained with
1042 Hematoxylin and eosin by standard techniques. Optimal number of tile pictures were obtained
1043 and stitched together via Keyence BZ-X710 fluorescent microscope.
1044
1045 Isolation of hippocampal neurons
1046 Hippocampus was dissected out from E18.5 mice, which were developed from *Ncs1*$^{+/-}$ female
1047 mouse crossed with *Ncs1*$^{+/-}$ male mice. The dissected hippocampus was dissociated by incubating
1048 the tissue in calcium magnesium free (CMF)-HBSS media (14175095, Gibco) supplemented
1049 with 10 mM HEPES (15630080, Gibco) containing 0.05% trypsin (15400-054, Gibco) at 37°C
1050 for 20 minutes. After washing the trypsinized tissue three times with 500 μl of CMF-HBSS
1051 containing 10 mM HEPES, the tissue was triturated with a fire polished Pasteur pipette. The
1052 dissociated cells were then plated on a 12 mm round coverslip (12-545-81, Fisher Scientific)
1053 coated with poly-D-lysine at a density of 60,000 cells per 24-well plate (930186, Thermo
1054 Scientific). The cells were grown in 500 μl of the Neurobasal Medium (21103049, Gibco)
1055 supplemented with 1×B27 (17504044, Gibco), 1×GlutaMax, 100 U/mL Penicillin-Streptomycin,
1056 and 10% horse serum (16050130, Gibco). 24 hours after plating, the media were replaced with
1057 the Neurobasal Medium media supplemented with 1×B27, 1×GlutaMax, and 100 U/mL
1058 Penicillin-Streptomycin. The genotype of the neurons was confirmed by genotyping PCR using
1059 the genotyping PCR primers described above.
1060
1061 Preparation of Mouse Embryonic Fibroblast

1062 Mouse embryonic fibroblasts (MEFs) were prepared from E13.5 mice embryos, which were
1063 developed from *Ncs1*$^{+/-}$ female mice crossed with *Ncs1*$^{+/-}$ male mice. After removing innards
1064 from the embryo, the remaining was minced with a razor blade (55411-050, VWR). The minced
1065 tissues were dissociated using 2 ml 0.05% trypsin/EDTA (25300-054, Gibco) for 20 minutes at
1066 37°C, followed by neutralization of trypsin by adding 4 ml of MEF media (DMEM high glucose
1067 (11995073, Gibco), 10% FBS (100-106, Gemini), 1×GlutaMax (35050-079, Thermo Fisher
1068 Scientific), and 100 U/mL Penicillin-Streptomycin (15140163, Thermo Fisher Scientific))
1069 containing 100 μg DNase I (LS002006, Worthington). Cells were then pelleted down, re-
1070 suspended in 15 ml of MEF media and plated into a T75 flask. The genotype of the MEFs were
1071 confirmed by genotyping PCR using the genotyping PCR primers described above. All
1072 experiments were performed with the cells that were passaged no more than three times.
1073

1074 <u>Immunoblotting of the tissue lysate</u>

1075 A 7-week-old *Ncs1*$^{-/-}$ and a 6-week-old *Ncs1*$^{+/+}$ mouse (not a littermate control) were anesthetized
1076 with isoflurane and euthanized by cervical dissociation. Tissues were quickly dissected out and
1077 minced with a razor blade (55411-050, VWR). The minced tissue is lysed in tissue lysis buffer
1078 (50 mM Tris-HCl [pH7.5], 150 mM NaCl, and 1% NP-40 (11332473001, Roche Applied
1079 Science)) for 15 minutes. Following clarification of the lysate at centrifugation at 15,000 rpm
1080 (21,000 g) for 15 minutes at 4°C, the concentration of the supernatant was measured by Bradford
1081 assay as previously described (see Procedure B step 8 in (Kanie & Jackson, 2018)). The lysate
1082 was mixed to prepare a sample containing 4 mg/ml lysate, 1×LDS buffer, and 2.5% 2-
1083 mercaptoethanol. 50 μg (for NCS1 blot) or 12 μg (for other proteins) were loaded onto

1084 NuPAGE™ Novex™ 4-12% Bis-Tris protein gels. Western blot was performed as described
1085 above and the fluorescent signal was detected on an Odyssey CLx Imaging System (LI-COR).
1086

1087 **Experimental replicates**

1088 The term "replicates" used in this paper indicate that the same cell lines were plated at different
1089 dates for each experiment. In most cases, cell lines were thawed from liquid nitrogen at different
1090 dates and immunostaining was performed at different dates among the replicates.
1091

1092 **Quantification of fluorescent intensity and statistical analysis**

1093 *Fluorescent intensity measurement*

1094 The fluorescent intensity was measured with 16-bit TIFF muti-color stack images acquired at
1095 63x magnification (NA1.4) by using Image J software. To measure the fluorescent intensity of
1096 centrosomal proteins, channels containing CEP170 and the protein of interest (POI) were
1097 individually extracted into separate images. A rolling ball background subtraction with a rolling
1098 ball radius of 5 pixels was implemented for both CEP170 and the POI to perform local
1099 background subtraction. The mask for both CEP170 and the POI was created by setting the lower
1100 threshold to the minimum level that covers only centrosome. Each mask was then combined by
1101 converting the two masks to a stack followed by z projection and then dilating the mask until the
1102 two masks are merged. After eroding the dilated masks several times, the fluorescent intensity of
1103 the POI was measured via "analyze particles" command with optimal size and circularity. The
1104 size and circularity are optimized for individual POI to detect most of the centrosome in the
1105 image without capturing non-centrosomal structure. Outliers (likely non-centrosomal structure)
1106 were then excluded from the data using the ROUT method with a false discovery rate of 1%

1107 using GraphPad Prism 9 software. Fluorescent intensity of ciliary proteins was measured
1108 similarly to centrosomal proteins but with several modifications. Mask was created for ciliary
1109 proteins by setting the lower threshold to the minimum level that covers only cilia. The size and
1110 circularity are optimized for individual POI to detect only cilia without capturing non-ciliary
1111 structure. Macros used for the intensity measurement are available from "Source Data- Macro for
1112 measuring fluorescent intensity of centrosomal proteins" and "Source Data-Macro for measuring
1113 fluorescent intensity of ciliary proteins" in an accompanying paper.
1114 To test whether the difference in the signal intensity is statistically different between control and
1115 test samples, the intensity measured through the described method was compared between
1116 control and test samples using nested one-way ANOVA with Dunnett's multiple comparisons
1117 test or nested t-test if there are more than two replicates. In case there are less than three
1118 replicates, the statistical test was not performed in a single experiment, as the signal intensity is
1119 affected slightly by staining procedure and statistical significance is affected largely by the
1120 number of cells examined. For example, we saw statistical significance in the signal intensity
1121 with the same samples that are stained independently if we analyze large number of the cells
1122 (more than 100 cells). Instead, we confirmed the same tendency in the change of fluorescent
1123 intensity in the test samples across two replicates.
1124
1125 *Statistical analysis for ciliation, ciliary vesicle recruitment, and CP110 removal assay*
1126 For ciliation, ciliary vesicle recruitment, and CP110 removal assay, the number of ciliated cells
1127 from the indicated number of replicates were compared between control (sgGFP or sgSafe) and
1128 the test samples using Welch's t test. The exact number of samples and replicated are indicated
1129 in the Source Data of the corresponding figures.

1130

1131 For all the statistics used in this paper, asterisks denote *: $0.01 \leq p < 0.05$, **: $p < 0.01$, ***: $p <$

1132 0.001, n.s.: not significant. All the statical significance was calculated by using GraphPad Prism

1133 9 software.

1134

1135 **Materials Availability Statement**

1136 All the newly created materials used in this paper including plasmids and stable cell lines are

1137 readily available from the corresponding authors (Tomoharu-Kanie@ouhsc.edu or

1138 pjackson@stanford.edu) upon request.

1139

1140 **Figure supplements**

1141 Figure 1-figure supplement 1. *Co-immunoprecipitation of endogenous NCS1 and the localization*

1142 *of CEP89 mutants shown in Figure 1C.*

1143 Figure 1-figure supplement 2. *A negative control for the experiment shown in Figure 1E and F.*

1144 Figure 2-figure supplement 1. *Localization of GFP tagged NCS1.*

1145 Figure 2-figure supplement 2. *Quantification data and immunoblot related to Figure 2.*

1146 Figure 2-figure supplement 3. *Localization of other distal appendage proteins in NCS1*

1147 *knockouts.*

1148 Figure 3-figure supplement 1. *Quantification of ciliary signal intensity of ARL13B in CEP89 and*

1149 *NCS1 knockouts.*

1150 Figure 5-figure supplement 1. *Calcium is required mainly for the stability of NCS1.*

1151 Figure 7-figure supplement 1. *The expression of NCS1 in various tissues.*

1152 Figure 7-figure supplement 2. *NCS1 localizes to the ciliary base in most ciliated tissues but not*
1153 *in photoreceptor cells*.
1154 Figure 7-figure supplement 3. *Localization of ciliary GPCRs is mildly decreased in hippocampal*
1155 *neurons prepared from Ncs1$^{-/-}$ mice*.
1156
1157 **Source Data**
1158 Figure 1A- Source Data. Uncropped image of silver staining of the tandem affinity purification
1159 analysis of CEP89.
1160 Figure 1B-Source Data. Mass spectrometry analysis of tandem affinity purification of CEP89.
1161 Figure 2A-Source Data. Immunofluorescence conditions in the experiment shown in Figure 2A.
1162 Figure 2B-Source Data. Immunofluorescence conditions in the experiment shown in Figure 2B.
1163 Figure 2C-Source Data. Immunofluorescence conditions, raw image quantification data, and
1164 detailed statistics of the experiment shown in Figure 2C.
1165 Figure 2D-I-Source Data. Immunofluorescence conditions in the experiment shown in Figure
1166 2D-I.
1167 Figure 2K-Source Data. Immunofluorescence conditions in the experiment shown in Figure 2K.
1168 Figure 2L-Source Data. Immunofluorescence conditions in the experiment shown in Figure 2L.
1169 Figure 2M-Source Data. Immunofluorescence conditions in the experiment shown in Figure 2M.
1170 Figure 3A-Source Data. Raw quantification data, immunofluorescence conditions and detailed
1171 statistics of the experiment shown in Figure 3A.
1172 Figure 3B-Source Data. Raw quantification data, immunofluorescence conditions and detailed
1173 statistics of the experiment shown in Figure 3B.

1174 Figure 3C-Source Data. Raw quantification data, immunofluorescence conditions and detailed
1175 statistics of the experiment shown in Figure 3C.
1176 Figure 3E-Source Data. Raw quantification data and detailed statistics of the experiment shown
1177 in Figure 3E.
1178 Figure 3F-Source Data. Raw quantification data, immunofluorescence conditions and detailed
1179 statistics of the experiment shown in Figure 3F.
1180 Figure 3F-Source Data. Raw quantification data, immunofluorescence conditions and detailed
1181 statistics of the experiment shown in Figure 3F.
1182 Figure 3G-Source Data. Raw quantification data, immunofluorescence conditions and detailed
1183 statistics of the experiment shown in Figure 3G.
1184 Figure 3H-Source Data. Raw quantification data, immunofluorescence conditions and detailed
1185 statistics of the experiment shown in Figure 3H.
1186 Figure 4B-Source Data. Raw quantification data, immunofluorescence conditions and detailed
1187 statistics of the experiment shown in Figure 4B.
1188 Figure 4C-Source Data. Raw quantification data, immunofluorescence conditions and detailed
1189 statistics of the experiment shown in Figure 4C.
1190 Figure 4D-Source Data. Raw quantification data, immunofluorescence conditions and detailed
1191 statistics of the experiment shown in Figure 4D.
1192 Figure 5C-Source Data. Immunofluorescence conditions in the experiment shown in Figure 5C.
1193 Figure 5D-Source Data. Raw quantification data and immunofluorescence conditions of the
1194 experiment shown in Figure 5D.
1195 Figure 5E-Source Data. Raw quantification data, immunofluorescence conditions and detailed
1196 statistics of the experiment shown in Figure 5E.

1197 Figure 5F-Source Data. Raw quantification data, immunofluorescence conditions and detailed
1198 statistics of the experiment shown in Figure 5F.
1199 Figure 6B-Source Data. Immunofluorescence conditions in the experiment shown in Figure 6B.
1200 Figure 6C-Source Data. Raw quantification data, immunofluorescence conditions and detailed
1201 statistics of the experiment shown in Figure 6C.
1202 Figure 6D-Source Data. Raw quantification data, immunofluorescence conditions and detailed
1203 statistics of the experiment shown in Figure 6D.
1204 Figure 6E-Source Data. Raw quantification data and immunofluorescence conditions of the
1205 experiment shown in Figure 6E.
1206 Figure 6F-Source Data. Raw quantification data and immunofluorescence conditions of the
1207 experiment shown in Figure 6F.
1208 Figure 7A-Source Data. Immunofluorescence conditions in the experiment shown in Figure 7A.
1209 Figure 7B-Source Data. Immunofluorescence conditions in the experiment shown in Figure 7B.
1210 Figure 7C-Source Data. Immunofluorescence conditions in the experiment shown in Figure 7C.
1211 Figure 7D-Source Data. Immunofluorescence conditions in the experiment shown in Figure 7D.
1212 Figure 7E-Source Data. Raw quantification data, immunofluorescence conditions and detailed
1213 statistics of the experiment shown in Figure 7E.
1214 Figure 7F-Source Data. Raw quantification data, immunofluorescence conditions and detailed
1215 statistics of the experiment shown in Figure 7F.
1216 Figure 7G-Source Data. Raw quantification data, immunofluorescence conditions and detailed
1217 statistics of the experiment shown in Figure 7G.
1218 Figure 7H-Source Data. Raw quantification data, immunofluorescence conditions and detailed
1219 statistics of the experiment shown in Figure 7H.

1220 Figure 8A-Source Data. Detailed information of the mice and detailed statistics of the
1221 experiment shown in Figure 8A.
1222 Figure 8B-C-Source Data. Raw data and detailed statistics of the experiment shown in Figure
1223 8B-C.
1224 Figure 8D-Source Data. Raw data and detailed statistics of the experiment shown in Figure 8D.
1225 Figure 8E-G-H-Source Data. Information of the mice used in the experiments shown in Figure
1226 8E, G and H.
1227 Figure 8F-Source Data. Raw data and detailed statistics of the experiment shown in Figure 8F.
1228
1229 Figure 1-Figure Supplement 1B-Source Data. Immunofluorescence conditions in the experiment
1230 shown in Figure 1-Figure supplement 1B.
1231 Figure 2-Figure Supplement 1-Source Data. Immunofluorescence conditions in the experiment
1232 shown in Figure 2-Figure supplement 1.
1233 Figure 2-Figure Supplement 2A-Source Data. Immunofluorescence conditions and raw
1234 quantification data of the experiment shown in Figure 2-Figure supplement 2A.
1235 Figure 2-Figure Supplement 2B-Source Data. Immunofluorescence conditions and raw
1236 quantification data of the experiment shown in Figure 2-Figure supplement 2B.
1237 Figure 2-Figure Supplement 2C-Source Data. Immunofluorescence conditions and raw
1238 quantification data of the experiment shown in Figure 2-Figure supplement 2C.
1239 Figure 2-Figure Supplement 3A-Source Data. Immunofluorescence conditions, raw
1240 quantification data and detailed statistics of the experiment shown in Figure 2-Figure supplement
1241 3A.

1242 Figure 2-Figure Supplement 3B-Source Data. Immunofluorescence conditions, raw
1243 quantification data and detailed statistics of the experiment shown in Figure 2-Figure supplement
1244 3B.
1245 Figure 2-Figure Supplement 3C-Source Data. Immunofluorescence conditions and raw
1246 quantification data of the experiment shown in Figure 2-Figure supplement 3C.
1247 Figure 2-Figure Supplement 3D-Source Data. Immunofluorescence conditions and raw
1248 quantification data of the experiment shown in Figure 2-Figure supplement 3D.
1249 Figure 3-Figure Supplement 1-Source Data. Immunofluorescence conditions, raw quantification
1250 data and detailed statistics of the experiment shown in Figure 3-Figure supplement 1A-C.
1251 Figure 5-Figure Supplement 1B-Source Data. Immunofluorescence conditions and raw
1252 quantification data of the experiment shown in Figure 5-Figure supplement 1B.
1253 Figure 5-Figure Supplement 1C-Source Data. Immunofluorescence conditions, raw
1254 quantification data and detailed statistics of the experiment shown in Figure 5-Figure supplement
1255 1C.
1256 Figure 7-Figure Supplement 2-Source Data. Immunofluorescence conditions in the experiment
1257 shown in Figure 7-Figure supplement 2A-E.
1258 Figure 7-Figure Supplement 3A-Source Data. Immunofluorescence conditions, raw
1259 quantification data and detailed statistics of the experiment shown in Figure 7-Figure supplement
1260 3A.
1261 Figure 7-Figure Supplement 3B-Source Data. Immunofluorescence conditions, raw
1262 quantification data and detailed statistics of the experiment shown in Figure 7-Figure supplement
1263 3B.
1264 Source Data 1-Primers used for genomic PCR and for generating sgRNA vectors.

1265 Source Data 2- The list of mouse embryonic fibroblasts used in this paper.

1266 Source Data 3- The list of Hippocampal Neurons used in this paper.

1267 Source Data 4- The list of antibodies used in this paper.

1268 Source Data 5- The list of cell lines used in this paper.

1269 Source Data 6- uncropped images of the Immunoblot.

1270 Source Data 7-summary of CRISPR knockout cells.

1271

1272 **References**

1273 Acs, P., Bauer, P. O., Mayer, B., Bera, T., Macallister, R., Mezey, E., & Pastan, I. (2015). A
1274 novel form of ciliopathy underlies hyperphagia and obesity in Ankrd26 knockout mice. Brain
1275 Struct Funct, 220(3), 1511-1528. doi:10.1007/s00429-014-0741-9

1276 Ames, J. B., Hendricks, K. B., Strahl, T., Huttner, I. G., Hamasaki, N., & Thorner, J. (2000).
1277 Structure and calcium-binding properties of Frq1, a novel calcium sensor in the yeast
1278 Saccharomyces cerevisiae. Biochemistry, 39(40), 12149-12161. doi:10.1021/bi0012890

1279 Ames, J. B., Ishima, R., Tanaka, T., Gordon, J. I., Stryer, L., & Ikura, M. (1997). Molecular
1280 mechanics of calcium-myristoyl switches. Nature, 389(6647), 198-202. doi:10.1038/38310

1281 Anderson, R. G. (1972). The three-dimensional structure of the basal body from the rhesus
1282 monkey oviduct. J Cell Biol, 54(2), 246-265. doi:10.1083/jcb.54.2.246

1283 Aravind, P., Chandra, K., Reddy, P. P., Jeromin, A., Chary, K. V., & Sharma, Y. (2008).
1284 Regulatory and structural EF-hand motifs of neuronal calcium sensor-1: Mg 2+ modulates Ca 2+
1285 binding, Ca 2+ -induced conformational changes, and equilibrium unfolding transitions. J Mol
1286 Biol, 376(4), 1100-1115. doi:10.1016/j.jmb.2007.12.033

Baksheeva, V. E., Nemashkalova, E. L., Firsov, A. M., Zalevsky, A. O., Vladimirov, V. I., Tikhomirova, N. K., . . . Zernii, E. Y. (2020). Membrane Binding of Neuronal Calcium Sensor-1: Highly Specific Interaction with Phosphatidylinositol-3-Phosphate. Biomolecules, 10(2). doi:10.3390/biom10020164

Barnes, B. G. (1961). Ciliated secretory cells in the pars distalis of the mouse hypophysis. J Ultrastruct Res, 5, 453-467. doi:10.1016/s0022-5320(61)80019-1

Bera, T. K., Liu, X. F., Yamada, M., Gavrilova, O., Mezey, E., Tessarollo, L., . . . Pastan, I. (2008). A model for obesity and gigantism due to disruption of the Ankrd26 gene. Proc Natl Acad Sci U S A, 105(1), 270-275. doi:10.1073/pnas.0710978105

Berbari, N. F., Bishop, G. A., Askwith, C. C., Lewis, J. S., & Mykytyn, K. (2007). Hippocampal neurons possess primary cilia in culture. J Neurosci Res, 85(5), 1095-1100. doi:10.1002/jnr.21209

Berbari, N. F., Malarkey, E. B., Yazdi, S. M., McNair, A. D., Kippe, J. M., Croyle, M. J., . . . Yoder, B. K. (2014). Hippocampal and cortical primary cilia are required for aversive memory in mice. PLoS One, 9(9), e106576. doi:10.1371/journal.pone.0106576

Bernatik, O., Pejskova, P., Vyslouzil, D., Hanakova, K., Zdrahal, Z., & Cajanek, L. (2020). Phosphorylation of multiple proteins involved in ciliogenesis by Tau Tubulin kinase 2. Mol Biol Cell, 31(10), 1032-1046. doi:10.1091/mbc.E19-06-0334

Bishop, G. A., Berbari, N. F., Lewis, J., & Mykytyn, K. (2007). Type III adenylyl cyclase localizes to primary cilia throughout the adult mouse brain. J Comp Neurol, 505(5), 562-571. doi:10.1002/cne.21510

Bornens, M. (2012). The centrosome in cells and organisms. Science, 335(6067), 422-426. doi:10.1126/science.1209037

Bourne, Y., Dannenberg, J., Pollmann, V., Marchot, P., & Pongs, O. (2001). Immunocytochemical localization and crystal structure of human frequenin (neuronal calcium sensor 1). J Biol Chem, 276(15), 11949-11955. doi:10.1074/jbc.M009373200

Bowler, M., Kong, D., Sun, S., Nanjundappa, R., Evans, L., Farmer, V., . . . Loncarek, J. (2019). High-resolution characterization of centriole distal appendage morphology and dynamics by correlative STORM and electron microscopy. Nat Commun, 10(1), 993. doi:10.1038/s41467-018-08216-4

Brechbuhl, J., Klaey, M., & Broillet, M. C. (2008). Grueneberg ganglion cells mediate alarm pheromone detection in mice. Science, 321(5892), 1092-1095. doi:10.1126/science.1160770

Breunig, J. J., Sarkisian, M. R., Arellano, J. I., Morozov, Y. M., Ayoub, A. E., Sojitra, S., . . . Town, T. (2008). Primary cilia regulate hippocampal neurogenesis by mediating sonic hedgehog signaling. Proc Natl Acad Sci U S A, 105(35), 13127-13132. doi:10.1073/pnas.0804558105

Brinkman, E. K., Chen, T., Amendola, M., & van Steensel, B. (2014). Easy quantitative assessment of genome editing by sequence trace decomposition. Nucleic Acids Res, 42(22), e168. doi:10.1093/nar/gku936

Burgoyne, R. D., & Weiss, J. L. (2001). The neuronal calcium sensor family of Ca2+-binding proteins. Biochem J, 353(Pt 1), 1-12. Retrieved from https://www.ncbi.nlm.nih.gov/pubmed/11115393

Cajanek, L., & Nigg, E. A. (2014). Cep164 triggers ciliogenesis by recruiting Tau tubulin kinase 2 to the mother centriole. Proc Natl Acad Sci U S A, 111(28), E2841-2850. doi:10.1073/pnas.1401777111

1331 Cheeseman, I. M., & Desai, A. (2005). A combined approach for the localization and tandem
1332 affinity purification of protein complexes from metazoans. Sci STKE, 2005(266), pl1.
1333 doi:10.1126/stke.2662005pl1
1334 Chong, W. M., Wang, W. J., Lo, C. H., Chiu, T. Y., Chang, T. J., Liu, Y. P., . . . Liao, J. C.
1335 (2020). Super-resolution microscopy reveals coupling between mammalian centriole subdistal
1336 appendages and distal appendages. Elife, 9. doi:10.7554/eLife.53580
1337 Craft, J. M., Harris, J. A., Hyman, S., Kner, P., & Lechtreck, K. F. (2015). Tubulin transport by
1338 IFT is upregulated during ciliary growth by a cilium-autonomous mechanism. J Cell Biol,
1339 208(2), 223-237. doi:10.1083/jcb.201409036
1340 Dason, J. S., Romero-Pozuelo, J., Atwood, H. L., & Ferrus, A. (2012). Multiple roles for
1341 frequenin/NCS-1 in synaptic function and development. Mol Neurobiol, 45(2), 388-402.
1342 doi:10.1007/s12035-012-8250-4
1343 Dateyama, I., Sugihara, Y., Chiba, S., Ota, R., Nakagawa, R., Kobayashi, T., & Itoh, H. (2019).
1344 RABL2 positively controls localization of GPCRs in mammalian primary cilia. J Cell Sci,
1345 132(2). doi:10.1242/jcs.224428
1346 de Rezende, V. B., Rosa, D. V., Comim, C. M., Magno, L. A., Rodrigues, A. L., Vidigal, P., . . .
1347 Romano-Silva, M. A. (2014). NCS-1 deficiency causes anxiety and depressive-like behavior
1348 with impaired non-aversive memory in mice. Physiol Behav, 130, 91-98.
1349 doi:10.1016/j.physbeh.2014.03.005
1350 Delgehyr, N., Sillibourne, J., & Bornens, M. (2005). Microtubule nucleation and anchoring at the
1351 centrosome are independent processes linked by ninein function. J Cell Sci, 118(Pt 8), 1565-
1352 1575. doi:10.1242/jcs.02302

Delling, M., DeCaen, P. G., Doerner, J. F., Febvay, S., & Clapham, D. E. (2013). Primary cilia are specialized calcium signalling organelles. Nature, 504(7479), 311-314. doi:10.1038/nature12833

Dickinson, M. E., Flenniken, A. M., Ji, X., Teboul, L., Wong, M. D., White, J. K., . . . Murray, S. A. (2016). High-throughput discovery of novel developmental phenotypes. Nature, 537(7621), 508-514. doi:10.1038/nature19356

Ding, X., Fragoza, R., Singh, P., Zhang, S., Yu, H., & Schimenti, J. C. (2020). Variants in RABL2A causing male infertility and ciliopathy. Hum Mol Genet, 29(20), 3402-3411. doi:10.1093/hmg/ddaa230

Dingemans, K. P. (1969). The relation between cilia and mitoses in the mouse adenohypophysis. J Cell Biol, 43(2), 361-367. doi:10.1083/jcb.43.2.361

Einstein, E. B., Patterson, C. A., Hon, B. J., Regan, K. A., Reddi, J., Melnikoff, D. E., . . . Tallent, M. K. (2010). Somatostatin signaling in neuronal cilia is critical for object recognition memory. J Neurosci, 30(12), 4306-4314. doi:10.1523/JNEUROSCI.5295-09.2010

Elias, J. E., & Gygi, S. P. (2007). Target-decoy search strategy for increased confidence in large-scale protein identifications by mass spectrometry. Nat Methods, 4(3), 207-214. doi:10.1038/nmeth1019

Fath, M. A., Mullins, R. F., Searby, C., Nishimura, D. Y., Wei, J., Rahmouni, K., . . . Sheffield, V. C. (2005). Mkks-null mice have a phenotype resembling Bardet-Biedl syndrome. Hum Mol Genet, 14(9), 1109-1118. doi:10.1093/hmg/ddi123

Forsyth, R. L., & Gunay-Aygun, M. (2020). Bardet-Biedl Syndrome Overview. 2003 Jul 14 [Updated 2020 Jul 23]. In E. D. Adam MP, Mirzaa GM, et al (Ed.), GeneReviews® [Internet]. Seattle (WA).

Forsythe, E., & Beales, P. L. (2013). Bardet-Biedl syndrome. Eur J Hum Genet, 21(1), 8-13. doi:10.1038/ejhg.2012.115

Ganga, A. K., Kennedy, M. C., Oguchi, M. E., Gray, S., Oliver, K. E., Knight, T. A., . . . Breslow, D. K. (2021). Rab34 GTPase mediates ciliary membrane formation in the intracellular ciliogenesis pathway. Curr Biol, 31(13), 2895-2905 e2897. doi:10.1016/j.cub.2021.04.075

Gierke, P., Zhao, C., Brackmann, M., Linke, B., Heinemann, U., & Braunewell, K. H. (2004). Expression analysis of members of the neuronal calcium sensor protein family: combining bioinformatics and Western blot analysis. Biochem Biophys Res Commun, 323(1), 38-43. doi:10.1016/j.bbrc.2004.08.055

Gomez, M., De Castro, E., Guarin, E., Sasakura, H., Kuhara, A., Mori, I., . . . Nef, P. (2001). Ca2+ signaling via the neuronal calcium sensor-1 regulates associative learning and memory in C. elegans. Neuron, 30(1), 241-248. doi:10.1016/s0896-6273(01)00276-8

Graham, J. M. (2015). Fractionation of Subcellular Organelles. Curr Protoc Cell Biol, 69, 3 1 1-3 1 22. doi:10.1002/0471143030.cb0301s69

Graser, S., Stierhof, Y. D., Lavoie, S. B., Gassner, O. S., Lamla, S., Le Clech, M., & Nigg, E. A. (2007). Cep164, a novel centriole appendage protein required for primary cilium formation. J Cell Biol, 179(2), 321-330. doi:10.1083/jcb.200707181

Gupta, G. D., Coyaud, E., Goncalves, J., Mojarad, B. A., Liu, Y., Wu, Q., . . . Pelletier, L. (2015). A Dynamic Protein Interaction Landscape of the Human Centrosome-Cilium Interface. Cell, 163(6), 1484-1499. doi:10.1016/j.cell.2015.10.065

Han, Y. G., Spassky, N., Romaguera-Ros, M., Garcia-Verdugo, J. M., Aguilar, A., Schneider-Maunoury, S., & Alvarez-Buylla, A. (2008). Hedgehog signaling and primary cilia are required for the formation of adult neural stem cells. Nat Neurosci, 11(3), 277-284. doi:10.1038/nn2059

Hermainski, J. G. (2012). Untersuchungen zur Funktion des Neuronalen Calcium Sensors 1 (NCS-1) an genetisch veränderten Mauslinien (Mus musculus, Linnaeus 1758). (Dissertation).

Hibbard, J. V. K., Vazquez, N., Satija, R., & Wallingford, J. B. (2021). Protein turnover dynamics suggest a diffusion-to-capture mechanism for peri-basal body recruitment and retention of intraflagellar transport proteins. Mol Biol Cell, 32(12), 1171-1180. doi:10.1091/mbc.E20-11-0717

Huttlin, E. L., Bruckner, R. J., Navarrete-Perea, J., Cannon, J. R., Baltier, K., Gebreab, F., . . . Gygi, S. P. (2021). Dual proteome-scale networks reveal cell-specific remodeling of the human interactome. Cell, 184(11), 3022-3040 e3028. doi:10.1016/j.cell.2021.04.011

Kanie, T., Abbott, K. L., Mooney, N. A., Plowey, E. D., Demeter, J., & Jackson, P. K. (2017). The CEP19-RABL2 GTPase Complex Binds IFT-B to Initiate Intraflagellar Transport at the Ciliary Base. Dev Cell, 42(1), 22-36 e12. doi:10.1016/j.devcel.2017.05.016

Kanie, T., & Jackson, P. K. (2018). Guanine Nucleotide Exchange Assay Using Fluorescent MANT-GDP. Bio Protoc, 8(7). doi:10.21769/BioProtoc.2795

Kurtulmus, B., Yuan, C., Schuy, J., Neuner, A., Hata, S., Kalamakis, G., . . . Pereira, G. (2018). LRRC45 contributes to early steps of axoneme extension. J Cell Sci, 131(18). doi:10.1242/jcs.223594

Lemire, S., Jeromin, A., & Boisselier, E. (2016). Membrane binding of Neuronal Calcium Sensor-1 (NCS1). Colloids Surf B Biointerfaces, 139, 138-147. doi:10.1016/j.colsurfb.2015.11.065

Lim, S., Strahl, T., Thorner, J., & Ames, J. B. (2011). Structure of a Ca2+-myristoyl switch protein that controls activation of a phosphatidylinositol 4-kinase in fission yeast. J Biol Chem, 286(14), 12565-12577. doi:10.1074/jbc.M110.208868

Lo, C. H., Lin, I. H., Yang, T. T., Huang, Y. C., Tanos, B. E., Chou, P. C., . . . Wang, W. J. (2019). Phosphorylation of CEP83 by TTBK2 is necessary for cilia initiation. J Cell Biol, 218(10), 3489-3505. doi:10.1083/jcb.201811142

Loktev, A. V., & Jackson, P. K. (2013). Neuropeptide Y family receptors traffic via the Bardet-Biedl syndrome pathway to signal in neuronal primary cilia. Cell Rep, 5(5), 1316-1329. doi:10.1016/j.celrep.2013.11.011

Loktev, A. V., Zhang, Q., Beck, J. S., Searby, C. C., Scheetz, T. E., Bazan, J. F., . . . Nachury, M. V. (2008). A BBSome subunit links ciliogenesis, microtubule stability, and acetylation. Dev Cell, 15(6), 854-865. doi:10.1016/j.devcel.2008.11.001

Lu, Q., Insinna, C., Ott, C., Stauffer, J., Pintado, P. A., Rahajeng, J., . . . Westlake, C. J. (2015). Early steps in primary cilium assembly require EHD1/EHD3-dependent ciliary vesicle formation. Nat Cell Biol, 17(3), 228-240. doi:10.1038/ncb3109

Mazo, G., Soplop, N., Wang, W. J., Uryu, K., & Tsou, M. F. (2016). Spatial Control of Primary Ciliogenesis by Subdistal Appendages Alters Sensation-Associated Properties of Cilia. Dev Cell, 39(4), 424-437. doi:10.1016/j.devcel.2016.10.006

Mirzadeh, Z., Merkle, F. T., Soriano-Navarro, M., Garcia-Verdugo, J. M., & Alvarez-Buylla, A. (2008). Neural stem cells confer unique pinwheel architecture to the ventricular surface in neurogenic regions of the adult brain. Cell Stem Cell, 3(3), 265-278. doi:10.1016/j.stem.2008.07.004

Molla-Herman, A., Ghossoub, R., Blisnick, T., Meunier, A., Serres, C., Silbermann, F., . . . Benmerah, A. (2010). The ciliary pocket: an endocytic membrane domain at the base of primary and motile cilia. J Cell Sci, 123(Pt 10), 1785-1795. doi:10.1242/jcs.059519

Mun, H. S., Saab, B. J., Ng, E., McGirr, A., Lipina, T. V., Gondo, Y., . . . Roder, J. C. (2015). Self-directed exploration provides a Ncs1-dependent learning bonus. Sci Rep, 5, 17697. doi:10.1038/srep17697

Mykytyn, K., Mullins, R. F., Andrews, M., Chiang, A. P., Swiderski, R. E., Yang, B., . . . Sheffield, V. C. (2004). Bardet-Biedl syndrome type 4 (BBS4)-null mice implicate Bbs4 in flagella formation but not global cilia assembly. Proc Natl Acad Sci U S A, 101(23), 8664-8669. doi:10.1073/pnas.0402354101

Nakamura, T. Y., Jeromin, A., Mikoshiba, K., & Wakabayashi, S. (2011). Neuronal calcium sensor-1 promotes immature heart function and hypertrophy by enhancing Ca2+ signals. Circ Res, 109(5), 512-523. doi:10.1161/CIRCRESAHA.111.248864

Nakamura, T. Y., Nakao, S., Nakajo, Y., Takahashi, J. C., Wakabayashi, S., & Yanamoto, H. (2017). Possible Signaling Pathways Mediating Neuronal Calcium Sensor-1-Dependent Spatial Learning and Memory in Mice. PLoS One, 12(1), e0170829. doi:10.1371/journal.pone.0170829

Ng, E., Georgiou, J., Avila, A., Trought, K., Mun, H. S., Hodgson, M., . . . Wong, A. H. C. (2020). Mice lacking neuronal calcium sensor-1 show social and cognitive deficits. Behav Brain Res, 381, 112420. doi:10.1016/j.bbr.2019.112420

Ng, E., Varaschin, R. K., Su, P., Browne, C. J., Hermainski, J., Le Foll, B., . . . Wong, A. H. (2016). Neuronal calcium sensor-1 deletion in the mouse decreases motivation and dopamine release in the nucleus accumbens. Behav Brain Res, 301, 213-225. doi:10.1016/j.bbr.2015.12.037

Nguyen, L. D., Nolte, L. G., Tan, W. J. T., Giuvelis, D., Santos-Sacchi, J., Bilsky, E., & Ehrlich, B. E. (2021). Comprehensive somatosensory and neurological phenotyping of NCS1 knockout mice. Sci Rep, 11(1), 2372. doi:10.1038/s41598-021-81650-5

Nishimura, D. Y., Fath, M., Mullins, R. F., Searby, C., Andrews, M., Davis, R., . . . Sheffield, V. C. (2004). Bbs2-null mice have neurosensory deficits, a defect in social dominance, and retinopathy associated with mislocalization of rhodopsin. Proc Natl Acad Sci U S A, 101(47), 16588-16593. doi:10.1073/pnas.0405496101

O'Callaghan, D. W., Ivings, L., Weiss, J. L., Ashby, M. C., Tepikin, A. V., & Burgoyne, R. D. (2002). Differential use of myristoyl groups on neuronal calcium sensor proteins as a determinant of spatio-temporal aspects of Ca2+ signal transduction. J Biol Chem, 277(16), 14227-14237. doi:10.1074/jbc.M111750200

O'Callaghan, D. W., Tepikin, A. V., & Burgoyne, R. D. (2003). Dynamics and calcium sensitivity of the Ca2+/myristoyl switch protein hippocalcin in living cells. J Cell Biol, 163(4), 715-721. doi:10.1083/jcb.200306042

Oguchi, M. E., Okuyama, K., Homma, Y., & Fukuda, M. (2020). A comprehensive analysis of Rab GTPases reveals a role for Rab34 in serum starvation-induced primary ciliogenesis. J Biol Chem, 295(36), 12674-12685. doi:10.1074/jbc.RA119.012233

Olafsson, P., Soares, H. D., Herzog, K. H., Wang, T., Morgan, J. I., & Lu, B. (1997). The Ca2+ binding protein, frequenin is a nervous system-specific protein in mouse preferentially localized in neurites. Brain Res Mol Brain Res, 44(1), 73-82. doi:10.1016/s0169-328x(96)00188-x

Paintrand, M., Moudjou, M., Delacroix, H., & Bornens, M. (1992). Centrosome organization and centriole architecture: their sensitivity to divalent cations. J Struct Biol, 108(2), 107-128. doi:10.1016/1047-8477(92)90011-x

Peitzsch, R. M., & McLaughlin, S. (1993). Binding of acylated peptides and fatty acids to phospholipid vesicles: pertinence to myristoylated proteins. Biochemistry, 32(39), 10436-10443. doi:10.1021/bi00090a020

Pongs, O., Lindemeier, J., Zhu, X. R., Theil, T., Engelkamp, D., Krah-Jentgens, I., . . . et al. (1993). Frequenin--a novel calcium-binding protein that modulates synaptic efficacy in the Drosophila nervous system. Neuron, 11(1), 15-28. doi:10.1016/0896-6273(93)90267-u

Ratai, O., Hermainski, J., Ravichandran, K., & Pongs, O. (2019). NCS-1 Deficiency Is Associated With Obesity and Diabetes Type 2 in Mice. Front Mol Neurosci, 12, 78. doi:10.3389/fnmol.2019.00078

Reiter, J. F., & Leroux, M. R. (2017). Genes and molecular pathways underpinning ciliopathies. Nat Rev Mol Cell Biol, 18(9), 533-547. doi:10.1038/nrm.2017.60

Rhee, S., Kirschen, G. W., Gu, Y., & Ge, S. (2016). Depletion of primary cilia from mature dentate granule cells impairs hippocampus-dependent contextual memory. Sci Rep, 6, 34370. doi:10.1038/srep34370

Rigaut, G., Shevchenko, A., Rutz, B., Wilm, M., Mann, M., & Seraphin, B. (1999). A generic protein purification method for protein complex characterization and proteome exploration. Nat Biotechnol, 17(10), 1030-1032. doi:10.1038/13732

Saab, B. J., Georgiou, J., Nath, A., Lee, F. J., Wang, M., Michalon, A., . . . Roder, J. C. (2009). NCS-1 in the dentate gyrus promotes exploration, synaptic plasticity, and rapid acquisition of spatial memory. Neuron, 63(5), 643-656. doi:10.1016/j.neuron.2009.08.014

Sang, L., Miller, J. J., Corbit, K. C., Giles, R. H., Brauer, M. J., Otto, E. A., . . . Jackson, P. K. (2011). Mapping the NPHP-JBTS-MKS protein network reveals ciliopathy disease genes and pathways. Cell, 145(4), 513-528. doi:10.1016/j.cell.2011.04.019

Schmidt, K. N., Kuhns, S., Neuner, A., Hub, B., Zentgraf, H., & Pereira, G. (2012). Cep164 mediates vesicular docking to the mother centriole during early steps of ciliogenesis. J Cell Biol, 199(7), 1083-1101. doi:10.1083/jcb.201202126

Shalata, A., Ramirez, M. C., Desnick, R. J., Priedigkeit, N., Buettner, C., Lindtner, C., . . . Martignetti, J. A. (2013). Morbid obesity resulting from inactivation of the ciliary protein CEP19 in humans and mice. Am J Hum Genet, 93(6), 1061-1071. doi:10.1016/j.ajhg.2013.10.025

Shevchenko, A., Tomas, H., Havlis, J., Olsen, J. V., & Mann, M. (2006). In-gel digestion for mass spectrometric characterization of proteins and proteomes. Nat Protoc, 1(6), 2856-2860. doi:10.1038/nprot.2006.468

Sillibourne, J. E., Hurbain, I., Grand-Perret, T., Goud, B., Tran, P., & Bornens, M. (2013). Primary ciliogenesis requires the distal appendage component Cep123. Biol Open, 2(6), 535-545. doi:10.1242/bio.20134457

Sillibourne, J. E., Specht, C. G., Izeddin, I., Hurbain, I., Tran, P., Triller, A., . . . Bornens, M. (2011). Assessing the localization of centrosomal proteins by PALM/STORM nanoscopy. Cytoskeleton (Hoboken), 68(11), 619-627. doi:10.1002/cm.20536

Simon, M. M., Greenaway, S., White, J. K., Fuchs, H., Gailus-Durner, V., Wells, S., . . . Brown, S. D. (2013). A comparative phenotypic and genomic analysis of C57BL/6J and C57BL/6N mouse strains. Genome Biol, 14(7), R82. doi:10.1186/gb-2013-14-7-r82

Sorokin, S. (1962). Centrioles and the formation of rudimentary cilia by fibroblasts and smooth muscle cells. J Cell Biol, 15, 363-377. doi:10.1083/jcb.15.2.363

Sorokin, S. P. (1968). Reconstructions of centriole formation and ciliogenesis in mammalian lungs. J Cell Sci, 3(2), 207-230. doi:10.1242/jcs.3.2.207

Spektor, A., Tsang, W. Y., Khoo, D., & Dynlacht, B. D. (2007). Cep97 and CP110 suppress a cilia assembly program. Cell, 130(4), 678-690. doi:10.1016/j.cell.2007.06.027

Stuck, M. W., Chong, W. M., Liao, J. C., & Pazour, G. J. (2021). Rab34 is necessary for early stages of intracellular ciliogenesis. Curr Biol, 31(13), 2887-2894 e2884. doi:10.1016/j.cub.2021.04.018

Tanos, B. E., Yang, H. J., Soni, R., Wang, W. J., Macaluso, F. P., Asara, J. M., & Tsou, M. F. (2013). Centriole distal appendages promote membrane docking, leading to cilia initiation. Genes Dev, 27(2), 163-168. doi:10.1101/gad.207043.112

Torres, J. Z., Miller, J. J., & Jackson, P. K. (2009). High-throughput generation of tagged stable cell lines for proteomic analysis. Proteomics, 9(10), 2888-2891. doi:10.1002/pmic.200800873

Vorobjev, I. A., & Chentsov Yu, S. (1982). Centrioles in the cell cycle. I. Epithelial cells. J Cell Biol, 93(3), 938-949. doi:10.1083/jcb.93.3.938

Wang, Z., Phan, T., & Storm, D. R. (2011). The type 3 adenylyl cyclase is required for novel object learning and extinction of contextual memory: role of cAMP signaling in primary cilia. J Neurosci, 31(15), 5557-5561. doi:10.1523/JNEUROSCI.6561-10.2011

Wright, K. J., Baye, L. M., Olivier-Mason, A., Mukhopadhyay, S., Sang, L., Kwong, M., . . . Jackson, P. K. (2011). An ARL3-UNC119-RP2 GTPase cycle targets myristoylated NPHP3 to the primary cilium. Genes Dev, 25(22), 2347-2360. doi:10.1101/gad.173443.111

Wright, M. H., Heal, W. P., Mann, D. J., & Tate, E. W. (2010). Protein myristoylation in health and disease. J Chem Biol, 3(1), 19-35. doi:10.1007/s12154-009-0032-8

Wu, C. T., Chen, H. Y., & Tang, T. K. (2018). Myosin-Va is required for preciliary vesicle transportation to the mother centriole during ciliogenesis. Nat Cell Biol, 20(2), 175-185. doi:10.1038/s41556-017-0018-7

Wu, Y., & Shroff, H. (2018). Faster, sharper, and deeper: structured illumination microscopy for biological imaging. Nat Methods, 15(12), 1011-1019. doi:10.1038/s41592-018-0211-z

Zhang, Y., Hao, J., Tarrago, M. G., Warner, G. M., Giorgadze, N., Wei, Q., . . . Hu, J. (2021). FBF1 deficiency promotes beiging and healthy expansion of white adipose tissue. Cell Rep, 36(5), 109481. doi:10.1016/j.celrep.2021.109481

Main Figures

1561

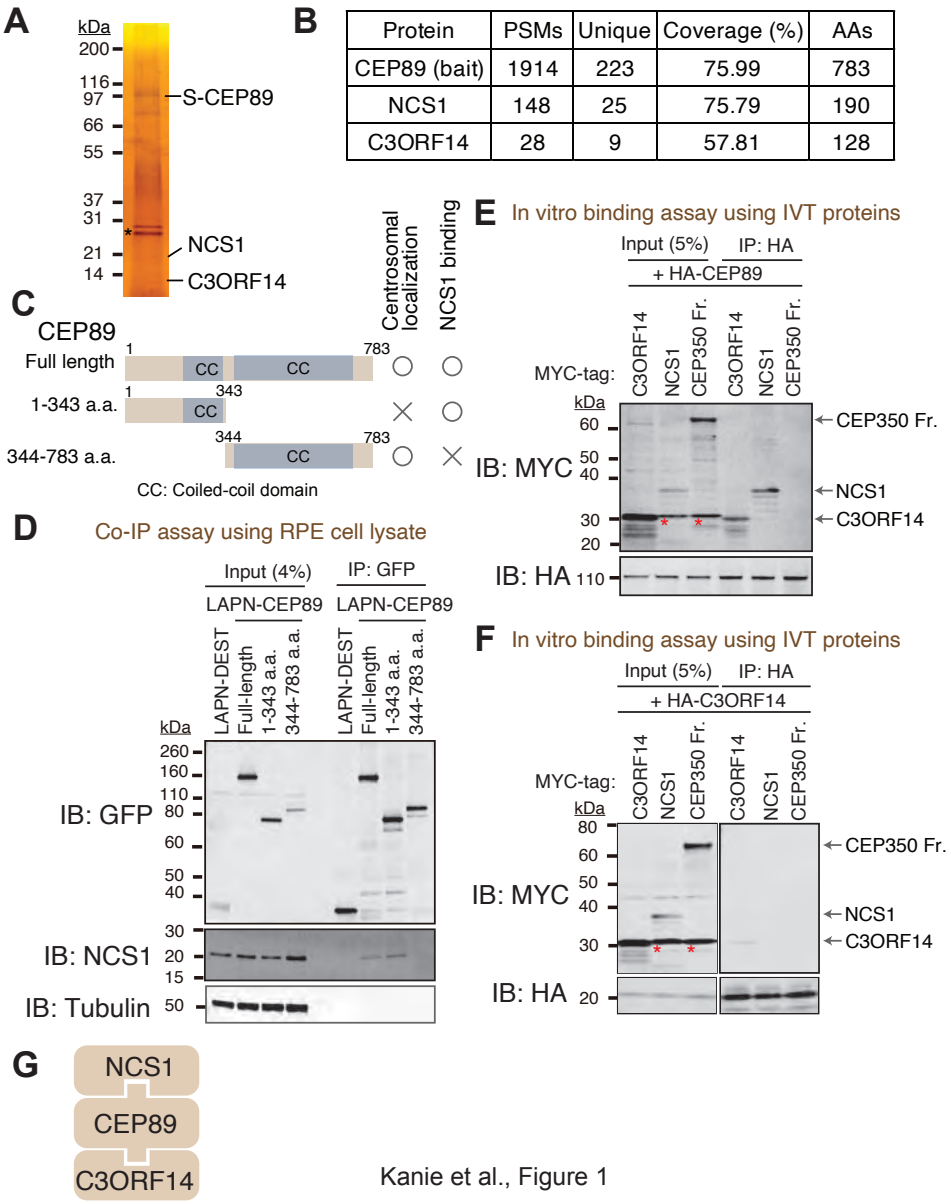

Protein	PSMs	Unique	Coverage (%)	AAs
CEP89 (bait)	1914	223	75.99	783
NCS1	148	25	75.79	190
C3ORF14	28	9	57.81	128

Kanie et al., Figure 1

Figure 1 ***Identification of Neuronal Calcium Sensor-1 as a stoichiometric interactor of CEP89.***

A. Silver staining of the eluate following tandem affinity purification of N-terminally LAP (EGFP-TEV cleavage site-S tag-PreScission cleavage site)-tagged CEP89 expressed in confluent RPE cells. The cell lysates were purified with GFP antibodies and S-protein beads, resolved by Sodium Dodecyl Sulfate–Polyacrylamide Gel Electrophoresis (SDS-PAGE) and visualized by silver staining. The bands corresponding to S tagged CEP89 (S-CEP89), NCS1, and C3ORF14 are indicated. Molecular weights (kDa) estimated from a protein marker are indicated. Asterisk denotes a band corresponding to TEV protease used for tandem affinity purification.

B. Tabulation of peptide-spectrum matches (PSMs), unique peptide counts, coverage, and the length of the amino acids from the mass spectrometry analysis of the eluate shown in (A).

C. A cartoon depicting the region of CEP89 important for centrosomal localization or binding to NCS1. Localization data can be found in Figure 1-figure supplement 1A.

D. Immunoblot (IB) analysis of the eluates from a co-immunoprecipitation assay of the full length or the indicated fragments of N-terminally LAP-tagged CEP89 expressed in confluent RPE cells. The cell lysates were purified with GFP antibodies, resolved by SDS-PAGE and immunoblotted with the indicated antibodies. Molecular weights (kDa) estimated from a protein marker are indicated.

E-F. Immunoblot (IB) analysis of the eluates from *in vitro* binding assay of the *in vitro* translated (IVT) N-terminally HA-tagged CEP89 (E) or C3ORF14 (F) and the indicated N-terminally MYC tagged proteins. The *in vitro* translated proteins were mixed and captured by HA-agarose beads, resolved by SDS-PAGE and immunoblotted with the indicated antibodies. The CEP350 fragment (2470-2836 a.a.), which binds to FOP efficiently (Figure 1-figure supplement 2A)(Kanie et al. 2017) serves as a negative control. Red asterisks indicate non-specific bands, which overlap with the MYC-tagged C3ORF14. Molecular weights (kDa) estimated from a protein marker are indicated.

G. The order of binding for CEP89-NCS1-C3ORF14 interaction.

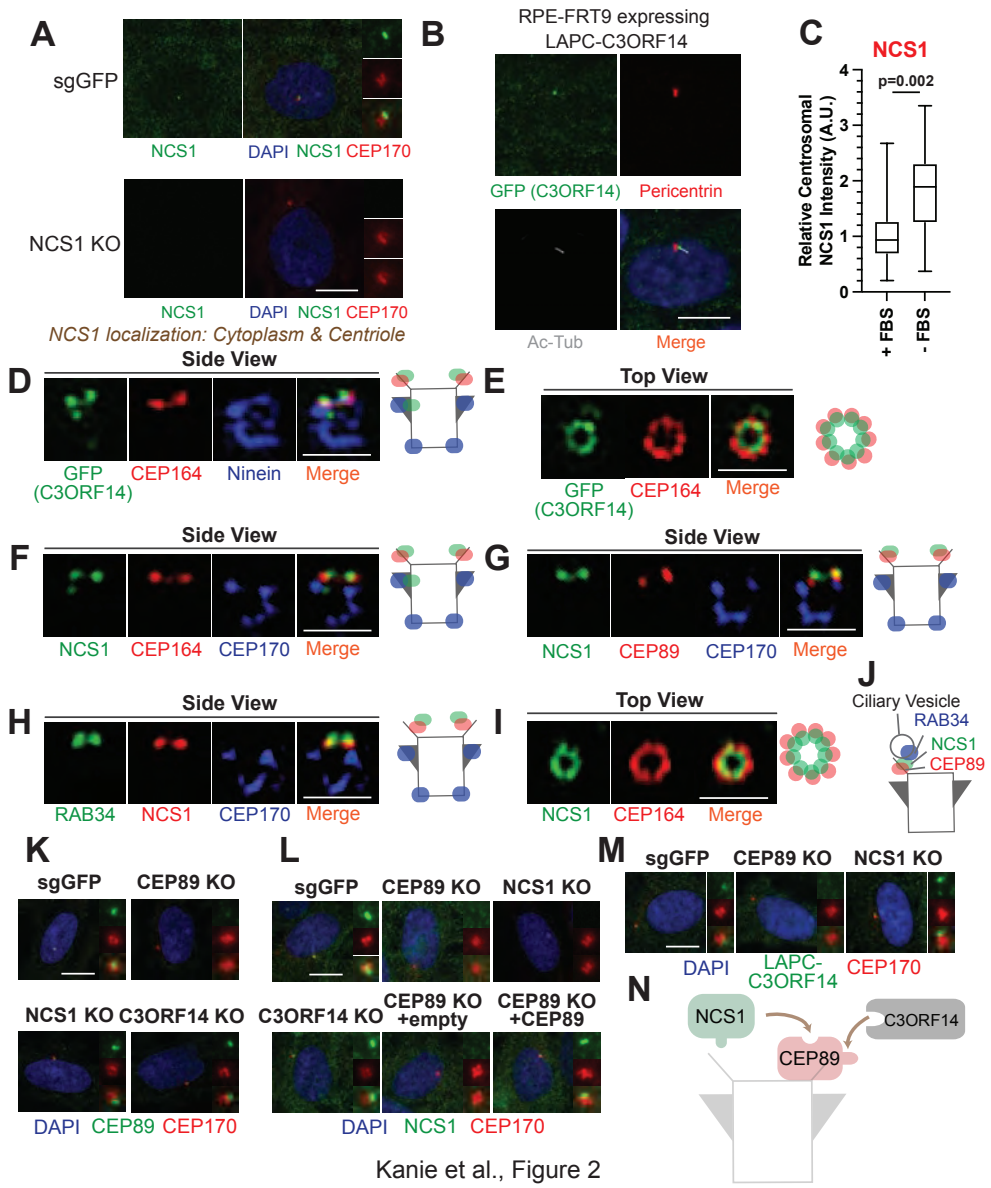

Figure 2 ***NCS1 is recruited to the distal appendage by CEP89.***

A. Immunofluorescence images taken via wide-field microscopy. Control (sgGFP) or NCS1 knockout RPE cells were serum starved for 24 hours, fixed, and stained with indicated antibodies. Insets at the right panels are the enlarged images of the mother centriole. Ac-Tub indicates acetylated α-tubulin. Scale bar: 10 μm.

B. Immunofluorescence images taken via wide-field microscopy. RPE cells expressing C-terminally LAP (LAPC) tagged C3ORF14 were serum starved for 24 hours, fixed, and stained with indicated antibodies. Scale bar: 10 μm.

C. Box plots showing centrosomal signal intensity of NCS1. RPE cells were grown in fetal bovine serum (FBS)-containing media for 24 hours, and then grown in either fetal bovine serum (FBS)-containing media (+ FBS) or serum free media (-FBS) for an additional 24 hours. Cells were fixed and stained with NCS1 antibody. Centrosomal signal intensity of NCS1 was measured from fluorescence images using the method described in Materials and Methods. A.U., arbitrary units. Data are combined from three replicates. Statistical significance was calculated from a nested T-test. The raw data, experimental conditions, and detailed statistics are available in Figure 2C-Source data

D-I. Immunofluorescence images taken via 3D-structured illumination microscopy. Side view (D, F, G, and H) or Top view (E and I) is shown. RPE cells were either grown to confluent (H) or serum starved for 24 hours (D-G and I), fixed and stained with indicated antibodies. Each individual image is from a representative z-slice. Scale bar: 1 μm. CEP170: a marker of subdistal appendage and proximal end of the mother centriole. A cartoon at the right of each figure shows estimated positions of each protein at the mother centriole.

J. A cartoon depicting the localization of NCS1 relative to RAB34 and CEP89. NCS1 is sandwiched between RAB34 and CEP89.

K-M. Immunofluorescence images taken via wide-filed microscopy. Control (sgGFP) or indicated knockout RPE cells were serum starved for 24 hours, fixed, and stained with indicated antibodies. Scale bar: 10 μm. Insets at the right panels are the enlarged images of the mother centriole. Quantification data are available in Figure 2-figure supplement 2A-C.

N. A cartoon depicting the order of recruitment of the CEP89-NCS1-C3ORF14 complex.

1563

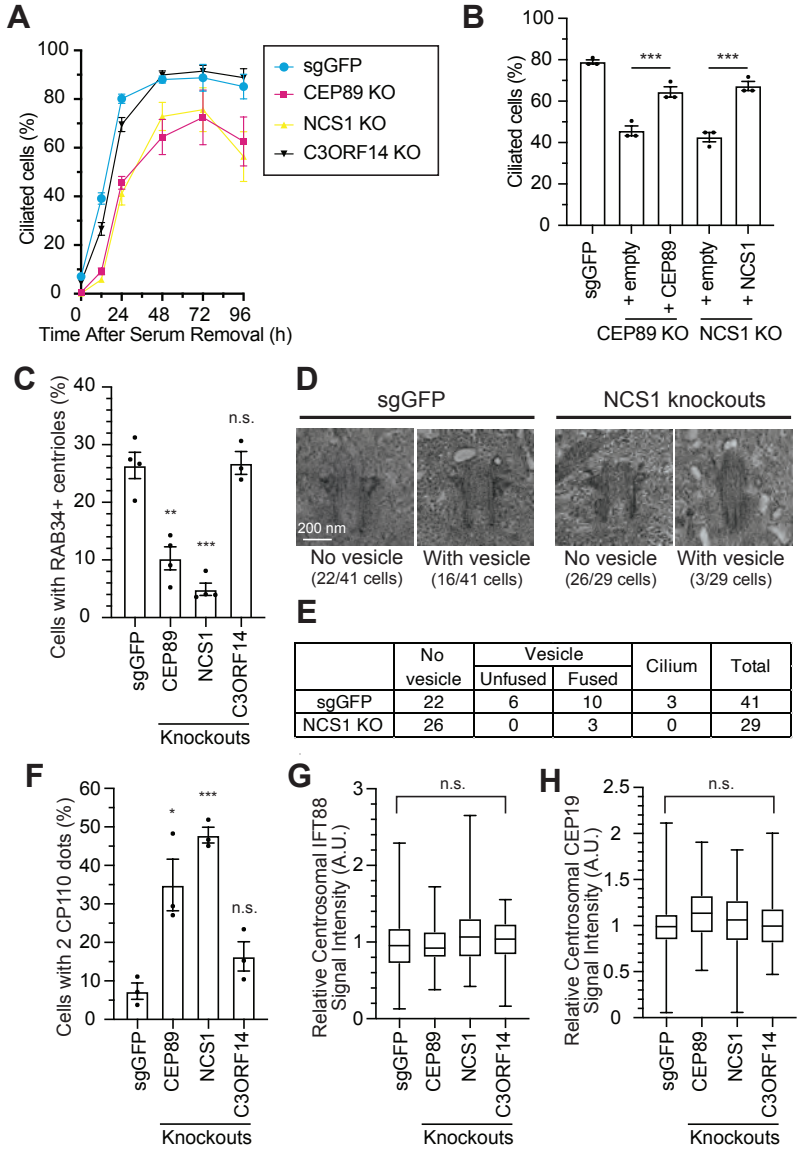

	No vesicle	Vesicle		Cilium	Total
		Unfused	Fused		
sgGFP	22	6	10	3	41
NCS1 KO	26	0	3	0	29

Kanie et al., Figure 3

Figure 3 ***NCS1 is important for ciliary vesicle recruitment, but not for IFT88/CEP19 recruitment.***

A. Time course of cilium formation assay in control (sgGFP) and indicated knockout RPE cells. The indicated cells were serum starved for 12, 24,48,72,96 hours, fixed, stained with α-ARL13B (to mark cilium) and α-CEP170 (to mark centriole), and imaged via wide-field microscopy. Data averaged from four independent experiments. Error bars represent ± SEM. Statistics obtained through comparing between each knockout and control by Welch's t-test. The raw data, experimental conditions, detailed statistics are available in Figure 3A-Source data.

B. Cilium formation assay in control (sgGFP) and indicated knockout RPE cells serum starved for 24 hours. Data averaged from three independent experiments, and each black dot indicates the value from the individual experiment. Error bars represent ± SEM. Statistics obtained by Welch's t-test. The raw data, experimental conditions, and detailed statistics are available in Figure 3B-Source data.

C. Ciliary vesicle recruitment assay in control (sgGFP) or indicated knockout RPE cells grown to confluence (without serum starvation). The data are averaged from 4 independent experiments, and each black dot indicates the value from each individual experiment. Error bars represent ± SEM. Statistics obtained through comparing between each knockout and control by Welch's t-test. The raw data, experimental conditions, and detailed statistics are available in Figure 3C-Source data.

D. Transmission electron microscopy analysis of the mother centriole in control (sgGFP) or NCS1 knockout RPE cells serum starved for 3 hours. The representative images of the mother centrioles without (left) or with (right) ciliary vesicle at the distal appendage are shown. Scale: 200 nm.

E. Quantification of the data from the experiments shown in Figure 3D. The raw data and detailed statistics are available in Figure 3E-Source data. This experiment was synchronized with the experiment shown in the Figure 4C of an accompanying paper, hence the values for sgGFP are exactly the same as the ones shown in the accompanying paper.

F. CP110 removal assay in control (sgGFP) and indicated knockout RPE cells serum starved for 24 hours. Data are averaged from three independent experiments, and each black dot indicates the value from the individual experiment. Error bars represent ± SEM. Statistics obtained through comparing between each knockout and control by Welch's t-test. The raw data, experimental conditions, and detailed statistics are available in Figure 3F-Source data.

G-H. Quantification of the centrosomal signal intensity of IFT88 (G) or CEP19 (H) in control (sgGFP) and indicated knockout RPE cells serum starved for 24 hours. The data are combined from three independent experiments. Statistical significance was calculated from nested T test. The raw data, experimental conditions, detailed statistics are available in Figure 3G-H-Source Data.

A.U., arbitrary units; n.s., not significant; *p < 0.05, **p < 0.01, ***p < 0.001

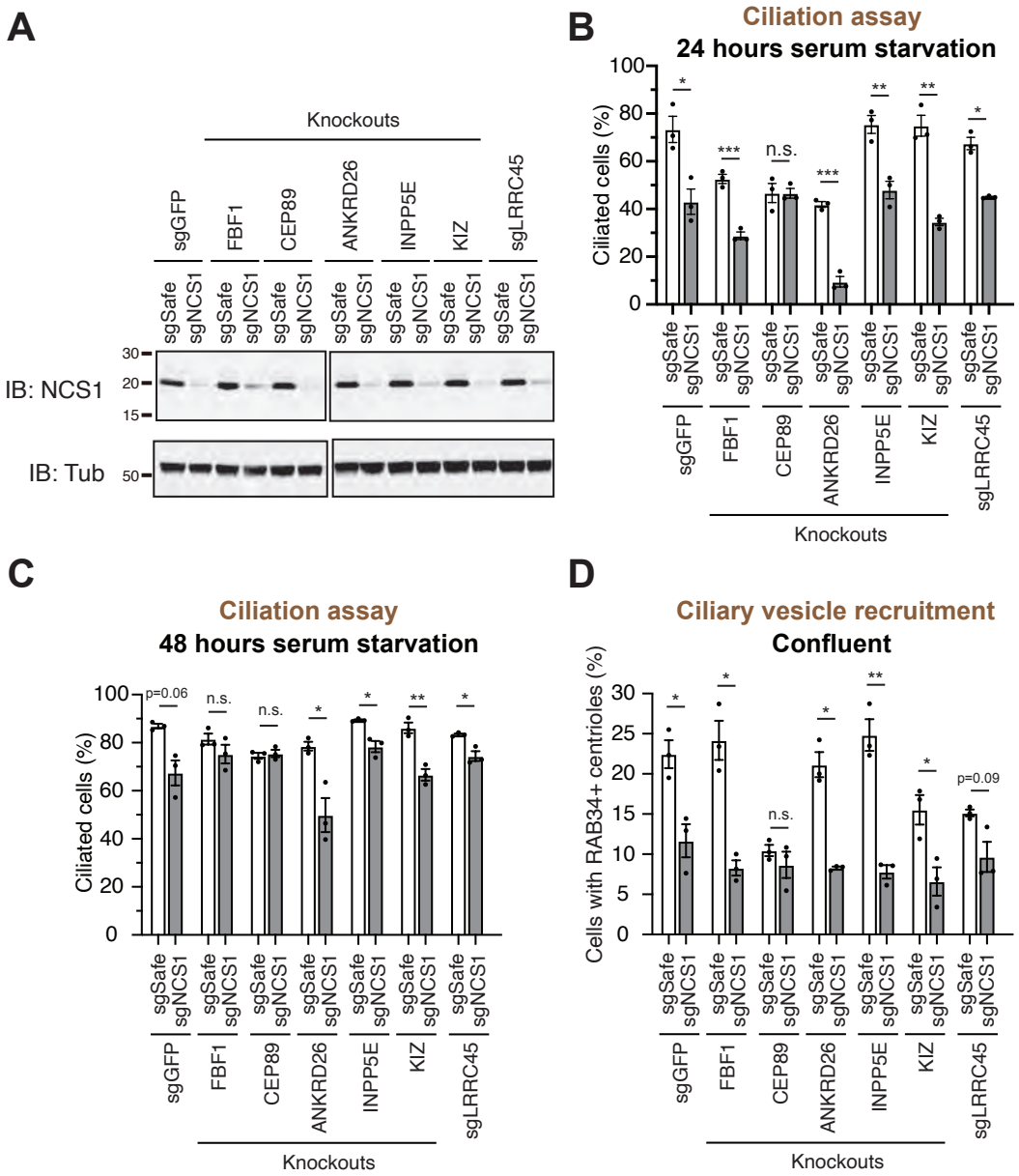

Kanie et al., Figure 4

Figure 4 A ***ciliary vesicle recruitment defect in NCS1 knockout cells is compensated by yet unknown distal appendage proteins.***

A. Immunoblot (IB) analysis of expression of NCS1 (IB: NCS1) and α-tubulin (IB: Tub) in control (sgGFP) or indicated knockout RPE cells stably expressing either sgSafe (non-targeting) or sgNCS1. The cells were grown to confluence (without serum starvation), lysed and analyzed by immunoblot. Molecular weights (kDa) estimated from a protein marker are indicated.

B-C. Cilium formation assay in control (sgGFP) and indicated knockout RPE cells stably expressing either sgSafe (non-targeting) or sgNCS1. The cells were serum starved for 24 (B) or 48 (C) hours. Data averaged from three independent experiments, and each black dot indicates the value from the individual experiment. Error bars represent ± SEM. Statistics obtained by Welch's t-test. The raw data, experimental conditions, and detailed statistics are available in Figure 4B-C-Source Data.

D. Ciliary vesicle recruitment assay in control (sgGFP) or indicated knockout RPE cells stably expressing either sgSafe (control) or sgNCS1. Cells were grown to confluence (without serum starvation). Data are averaged from three independent experiments. Error bars represent ± SEM. Statistics obtained by Welch's t-test. The raw data, experimental conditions, and detailed statistics are available in Figure 4D-Source data.

n.s., not significant; *$p < 0.05$, **$p < 0.01$, ***$p < 0.001$

1564

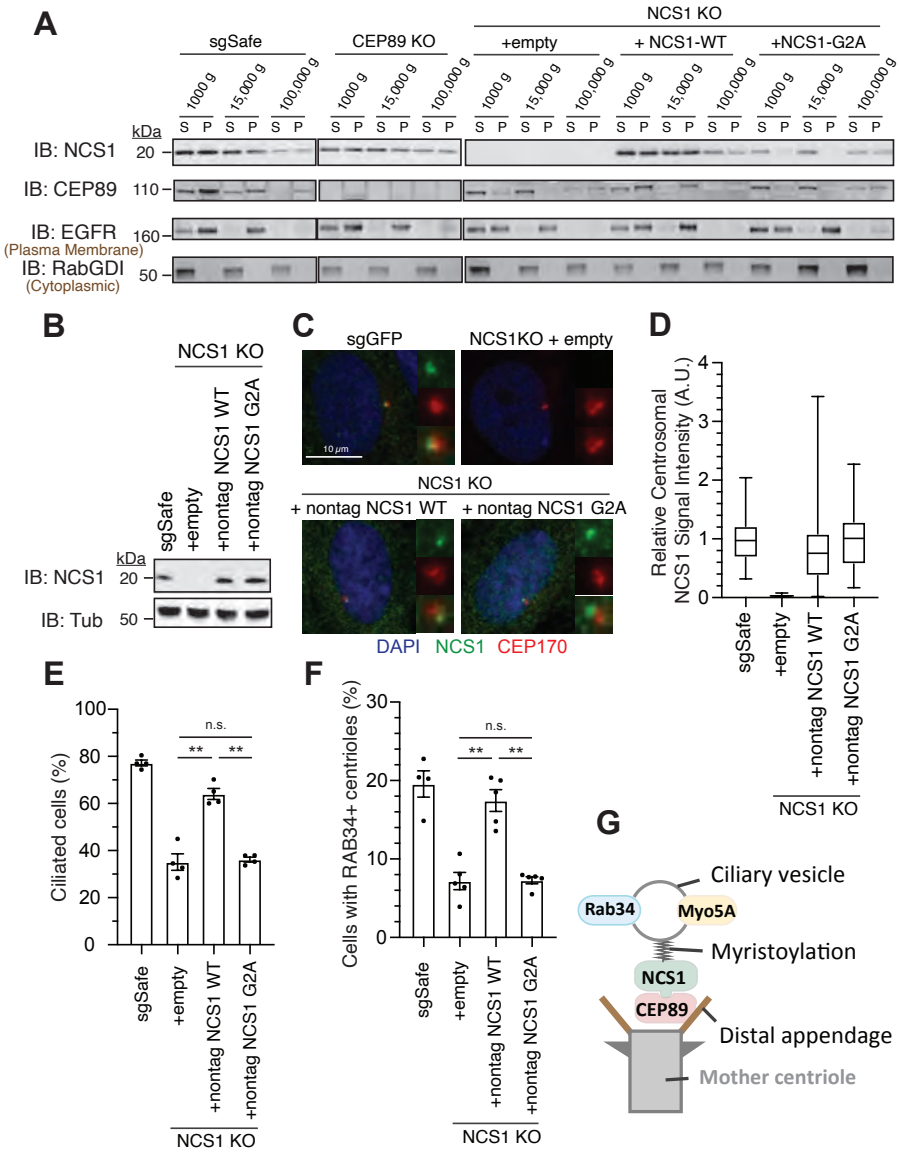

Kanie et al., Figure 5

Figure 5 ***NCS1 captures the ciliary vesicle via its myristoylation motif.***

A. Immunoblot (IB) analysis of expression of NCS1, CEP89, EGFR, and RabGDI. The control (sgSafe) and indicated knockout cells were grown to confluence, lysed by nitrogen cavitation, and fractionated by differential centrifugation at 1,000, 15,000, and 100,000 x g. S: supernatant; P: pellet. Molecular weights (kDa) estimated from a protein marker are indicated. EGFR and RabGDI serves as representative markers for plasma membrane or cytoplasmic proteins, respectively.

B. Immunoblot (IB) analysis of expression of NCS1 and α-tubulin in control (sgSafe) or or indicated RPE cells. Molecular weights (kDa) estimated from a protein marker are indicated.

C. Immunofluorescence images taken via wide-filed microscopy in the cells described in (B) serum starved for 24 hours. Insets at the right panels are the enlarged images of the mother centriole. Scale bar: 10 μm.

D. Box plots showing centrosomal signal intensity of NCS1 in cells described in (B) that were serum starved for 24 hours. A.U., arbitrary units. The data from a representative experiment are shown. The raw data and experimental conditions are available in Figure 5D-Source data.

E. Cilium formation assay in the cells described in (B) serum starved for 24 hours. Data averaged from four independent experiments, and each black dot indicates the value from the individual experiment. Error bars represent ± SEM. Statistics obtained by Welch's t-test. The raw data, experimental conditions, and detailed statistics are available in Figure 5E-Source data.

F. Ciliary vesicle recruitment assay in the cells described in (B) grown to confluence (without serum starvation). Data averaged from 5 independent experiments. Error bars represent ± SEM. Statistics obtained through comparing between each knockout and control by Welch's t-test. The raw data, experimental conditions, and detailed statistics are available in Figure 5F-Source data.

G. A cartoon depicting the model generated by our results. NCS1 is recruited to the distal appendage by CEP89 and captures ciliary vesicle via its myristoylation motif. n.s., not significant; *$p < 0.05$, **$p < 0.01$, ***$p < 0.001$

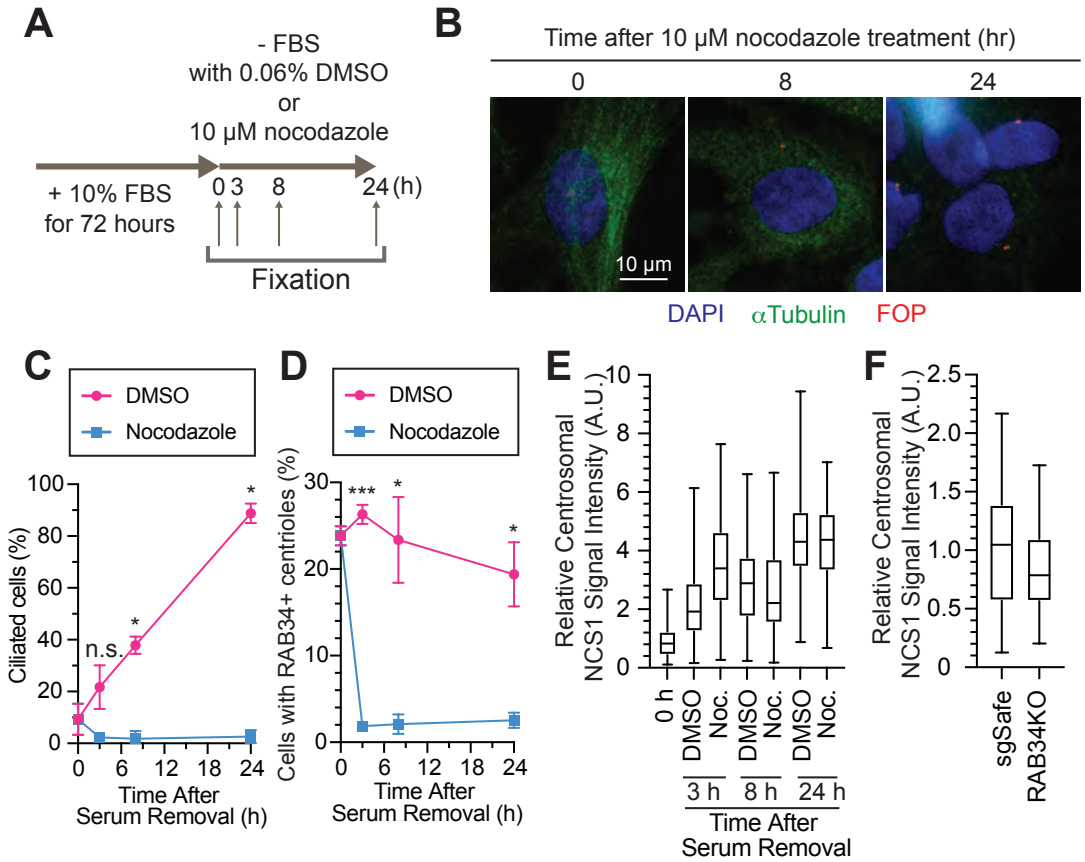

Kanie et al., Figure 6

Figure 6 ***Ciliary vesicle, but not NCS1 and CEP89, is recruited to the centriole via microtubule.***

A. A cartoon showing the method used to test the requirement of microtubules in ciliary vesicle recruitment and NCS1 localization. RPE cells were cultured in media containing 10% FBS for 72 hours, then serum starved (-FBS) for indicated times in the presence of nocodazole or dimethyl sulfoxide (DMSO).

B. Immunofluorescence images taken via wide-filed microscopy. RPE cells were cultured as shown in (A), fixed, and stained with antibodies against α-Tubulin and FGFR1OP (FOP). Scale bar: 10 μm.

C. The time course of cilium formation in cells treated with either DMSO (magenta) or nocodazole (blue). The cells were fixed at indicated time points, stained with α-ARL13B (to mark cilium) and α-CEP170 (to mark centriole), and imaged via wide-field microscopy. Data averaged from three independent experiments. Error bars represent ± SEM. Statistics obtained through comparing between DMSO and nocodazole treated cells at each time point by Welch's t-test. The raw data, experimental conditions, and detailed statistics are available in Figure 6C-Source data.

D. The time course of ciliary vesicle recruitment in cells treated with either DMSO (magenta) or nocodazole (blue). The cells were fixed at indicated time points, stained with α-RAB34 (to mark ciliary vesicle) and α-CEP170 (to mark centriole), and imaged via wide-field microscopy. Data are averaged from three independent experiments. Error bars represent ± SEM. Statistics obtained through comparing between DMSO and nocodazole treated cells at each time point by Welch's t-test. The raw data, experimental conditions, and detailed statistics are available in Figure 6D-Source data.

E. Box plots showing centrosomal signal intensity of NCS1 in RPE cells prepared using the method described in (A). The data from the representative experiment are shown. The raw data and experimental conditions are available in Figure 6E-Source data.

F. Quantification of the centrosomal signal intensity of NCS1 in control or RAB34 knockout RPE cells serum starved for 24 hours. The data from the representative experiment are shown. The raw data and experimental conditions are available in Figure 6F-Source data.

A.U., arbitrary units; n.s., not significant; *$p < 0.05$, **$p < 0.01$, ***$p < 0.001$

1566

1567

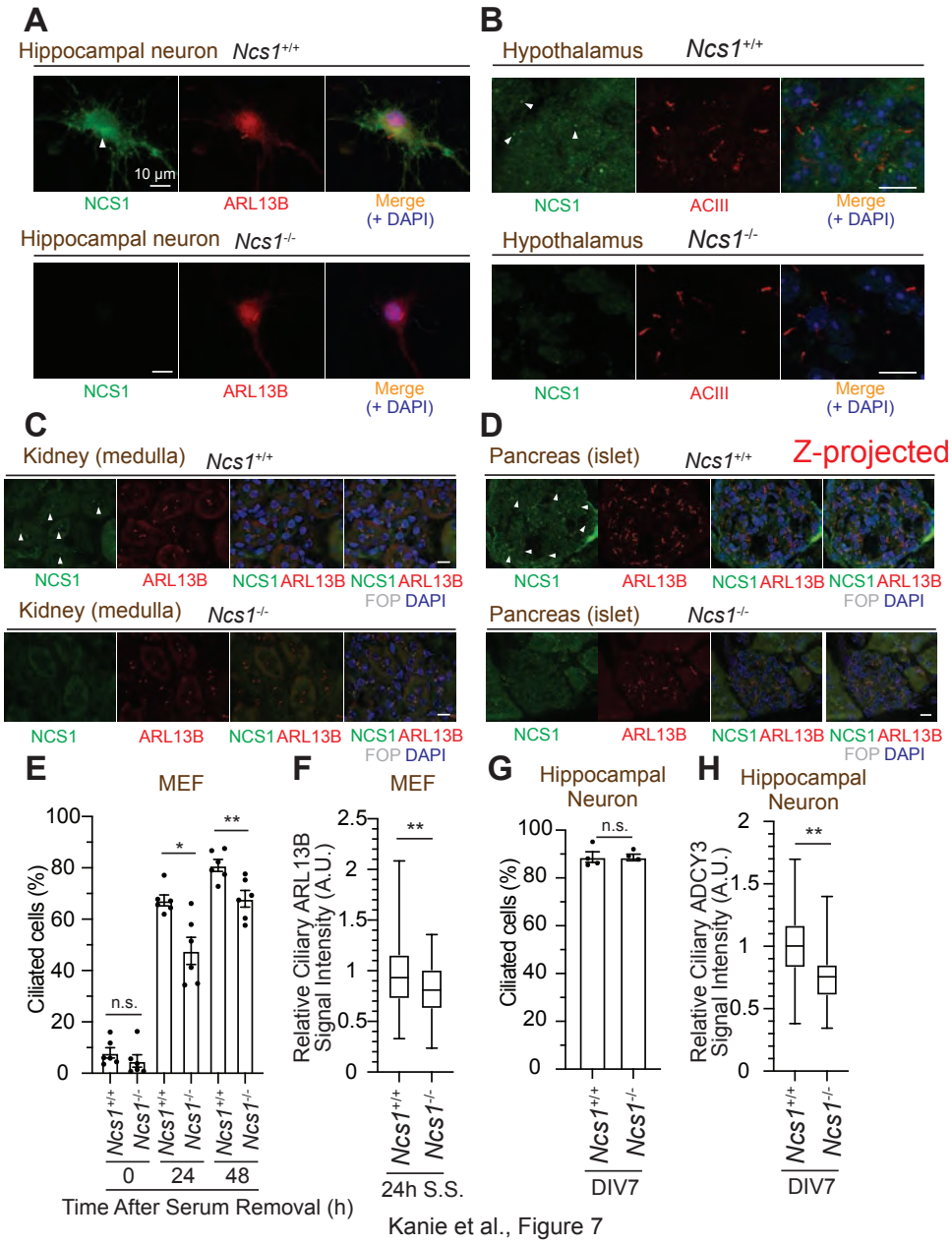

Figure 7 ***NCS1 localizes to the ciliary base in ciliated tissues and gets involved in cilium formation and ciliary membrane protein trafficking.***

A. Immunofluorescence images of cultured hippocampal neurons taken by wide-field microscopy. The isolated hippocampal neurons from E18.5 mice were fixed and stained for the indicated markers. Arrow indicates Ncs1 localization at the ciliary base. The individual image is from a representative z-slice. Scale bar: 10 μm.

B-D. Immunofluorescence images of indicated mouse tissues taken via spinning disk confocal microscopy. Tissue sections prepared from 8 week old *Ncs1*$^{+/+}$ or *Ncs1*$^{-/-}$ mice with the method described in Materials and Methods were stained for indicated markers. The images shown in (D) were created by maximum intensity z-projection. The other images were from representative z-slices. Arrowheads indicate NCS1 localization. Scale bar: 10 μm.

E. Cilium formation assay in *Ncs1*$^{+/+}$ or *Ncs1*$^{-/-}$ mouse embryonic fibroblasts (MEFs) serum starved for indicated time. Data averaged from six different MEFs per genotype. Each black dot indicates the value from the individual experiment. Error bars represent ± SEM. Statistics obtained through comparing between the two genotypes at each time point by Welch's t-test. The raw data, experimental conditions, and detailed statistics are available in Figure 7E-Source data.

F. Box plots showing ciliary signal intensity of ARL13B in *Ncs1*$^{+/+}$ or *Ncs1*$^{-/-}$ MEFs. The cells were serum starved for 24 hours, fixed, stained with α-ARL13B (to mark cilium) and α-CEP170 (to mark centriole), and imaged via wide-field microscopy. Data averaged from six different MEFs per genotype. Statistical significance was calculated from nested T test. The raw data, experimental conditions, and detailed statistics are available in Figure 7F-Source data.

G. Cilium formation assay in isolated hippocampal neurons prepared from *Ncs1*$^{+/+}$ or *Ncs1*$^{-/-}$ E18.5 mouse embryos at 7 days in vitro (DIV). Data are averaged from four different hippocampal neurons per genotype. Each black dot indicates the value from the individual experiment. Error bars represent ± SEM. Statistics obtained through comparing between the two genotypes at each time point by Welch's t-test. The raw data, experimental conditions, detailed statistics are available in Figure 7G-Source data.

H. Box plots showing ciliary signal intensity of ADCY3 in isolated hippocampal neurons prepared from *Ncs1*$^{+/+}$ or *Ncs1*$^{-/-}$ E18.5 mouse embryos at DIV7. The cells were fixed and stained with α-ADCY3 antibody, and imaged via wide-field microscopy. Data are averaged from five different neurons per genotype. Statistical significance was calculated from nested T test. The raw data, experimental conditions, and detailed statistics are available in Figure 7H-Source data.

A.U., arbitrary units; n.s., not significant; *p < 0.05, **p < 0.01, ***p < 0.001

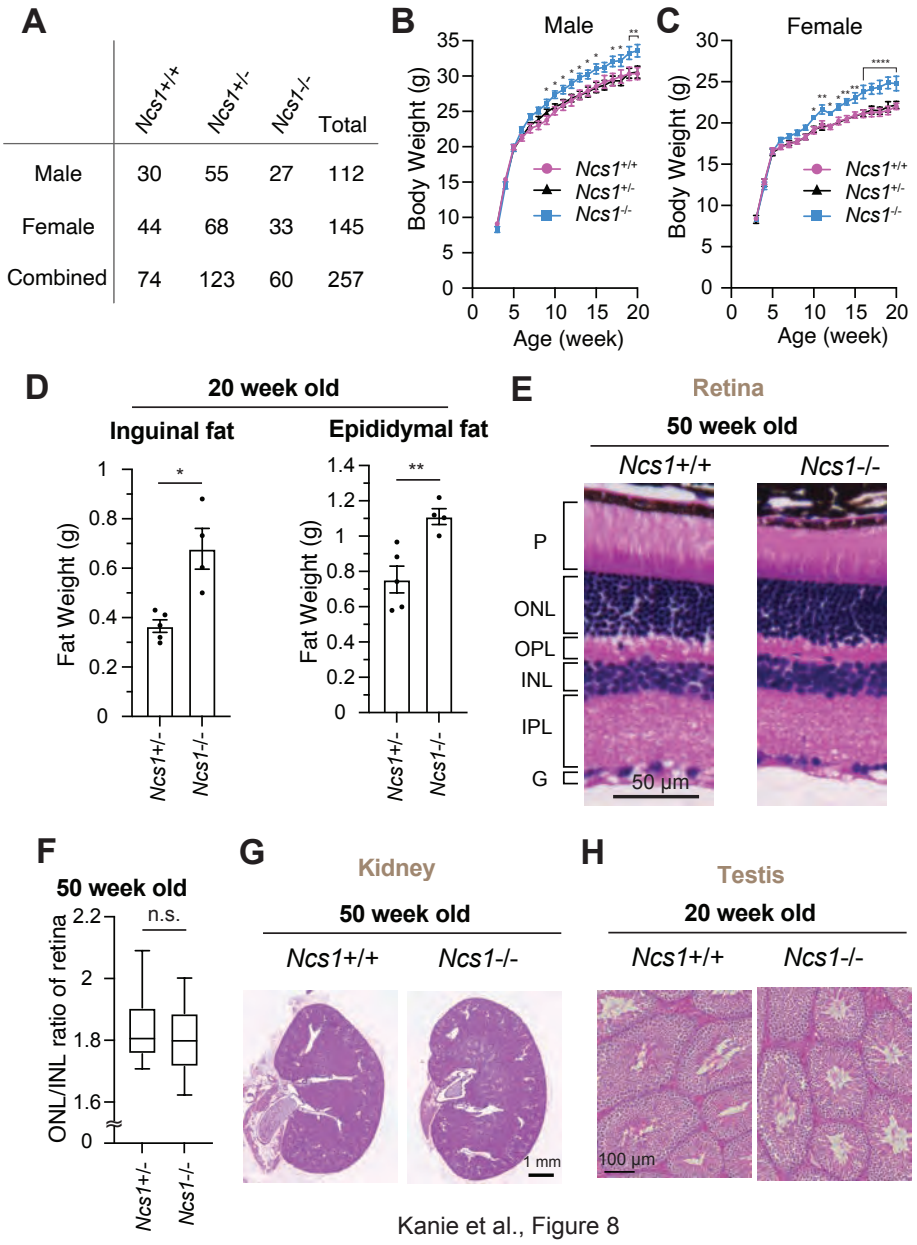

Figure 8 *Ncs1* knockout mice display obesity but no other ciliopathy-related phenotypes.

A. A table showing viability of *Ncs1*$^{+/+}$, *Ncs1*$^{+/-}$, or *Ncs1*$^{-/-}$ mice, generated by crossing *Ncs1*$^{+/-}$ male and female, at P21. Detailed information of the mice and statistics are available in Figure 8A-Source Data.

B-C. Body weight analysis of *Ncs1*$^{+/+}$, *Ncs1*$^{+/-}$, or *Ncs1*$^{-/-}$ male (B) and female (C) mice. Raw data and detailed statistics are available from Figure 8B-C-Source Data.

D. Measurements of the weights of inguinal fat (left) or epididymal fat (right) from 20-week-old *Ncs1*$^{+/+}$ or *Ncs1*$^{-/-}$ male mice. Raw data and detailed statistics are available in Figure D-Source Data.

E. Hematoxylin and Eosin (H&E) staining of the retina prepared from 50-week-old *Ncs1*$^{+/+}$ or *Ncs1*$^{-/-}$ female mice. Scale bar: 50 μm. G, ganglion cell layer; IPL, inner plexiform layer; INL, inner nuclear layer; OPL, outer plexiform layer; ONL, outer nuclear layer; P, photoreceptor cell layer. Representative images from five *Ncs1*$^{+/+}$ or *Ncs1*$^{-/-}$ mice are shown. Detailed information of the mice is available in Figure 8E-G-H-Source Data.

F. Quantification of ONL/INL ration of the retina prepared from 50-week-old *Ncs1*$^{+/+}$ or *Ncs1*$^{-/-}$ mice. 8 areas per mouse and 5 mice from each genotype were analyzed. Statistical significance was calculated from nested T test. The raw data, detailed information of the mice, and detailed statistics are available in Figure 8F-Source Data.

G-H. H&E staining of the kidney (G) or Testis (H) prepared from 50-week-old *Ncs1*$^{+/+}$ or *Ncs1*$^{-/-}$ female mice (G) or 20-week-old *Ncs1*$^{+/+}$ or *Ncs1*$^{-/-}$ male mice. Scale bar: 1mm (G) and 100 μm (H). Representative images from five (G) or three (H) *Ncs1*$^{+/+}$ or *Ncs1*$^{-/-}$ mice are shown. Detailed information of the mice is available in Figure 8E-G-H-Source Data.

n.s., not significant; *p < 0.05, **p < 0.01, ***p < 0.001

Figure supplements

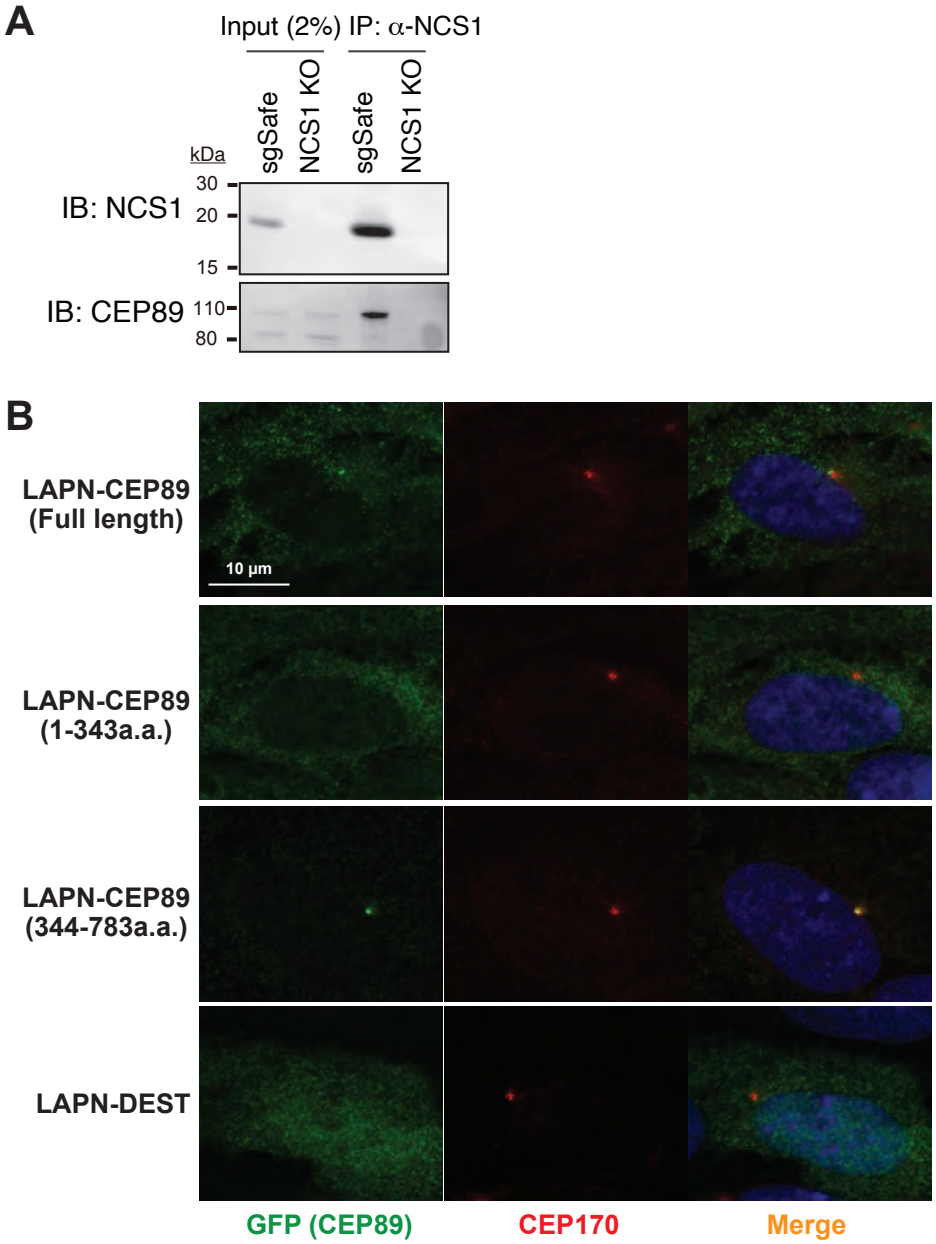

Kanie et al., Figure 1-figure supplement 1

Figure 1-figure supplement 1 ***Individual channels of the images shown in Figure 1A.***

A. Immunoblot (IB) analysis of the eluates from co-immunoprecipitation assay of endogenous NCS1 in the control (sgSafe) or NCS1 knockout cells. The eluates were immunoblotted with antibodies against NCS1 or CEP89. Molecular weights (kDa) estimated from a protein marker are indicated.
B. Immunofluorescence images taken via wide-field microscopy. RPE cells expressing the indicated N-terminally LAP (EGFP and S) tagged fragments of CEP89 or LAPN (control) were serum starved for 24 hours, fixed, and stained with antibodies against GFP and CEP170. Scale bar: 10 μm.

1569

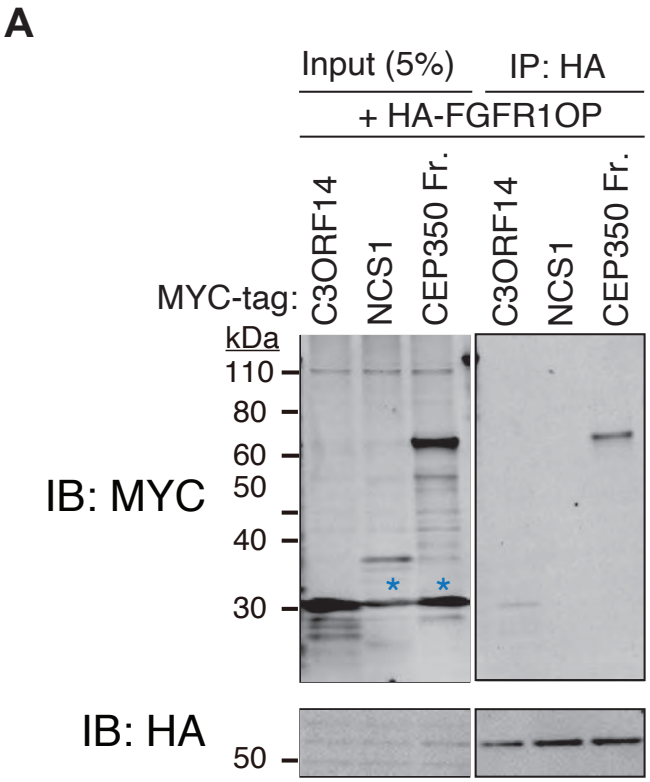

Kanie et al., Figure 1-figure supplement 2

Figure 1-figure supplement 2 ***A negative control for the experiment shown in Figure 1E and F.***

A. Immunoblot (IB) analysis of the eluates from *in vitro* binding assay of the *in vitro* translated N-terminally HA-tagged FGFR1OP and the indicated N-terminally MYC tagged proteins. The *in vitro* translated proteins were mixed and captured by HA-agarose beads, resolved by SDS-PAGE and immunoblotted with the indicated antibodies. The CEP350 fragment (2470-2836 a.a.), which binds to FGFR1OP efficiently (Kanie et al. 2017) serves as a positive control. Blue asterisks indicate non-specific bands, which overlap with the MYC-tagged C3ORF14. Molecular weights (kDa) estimated from a protein marker are indicated.

1570

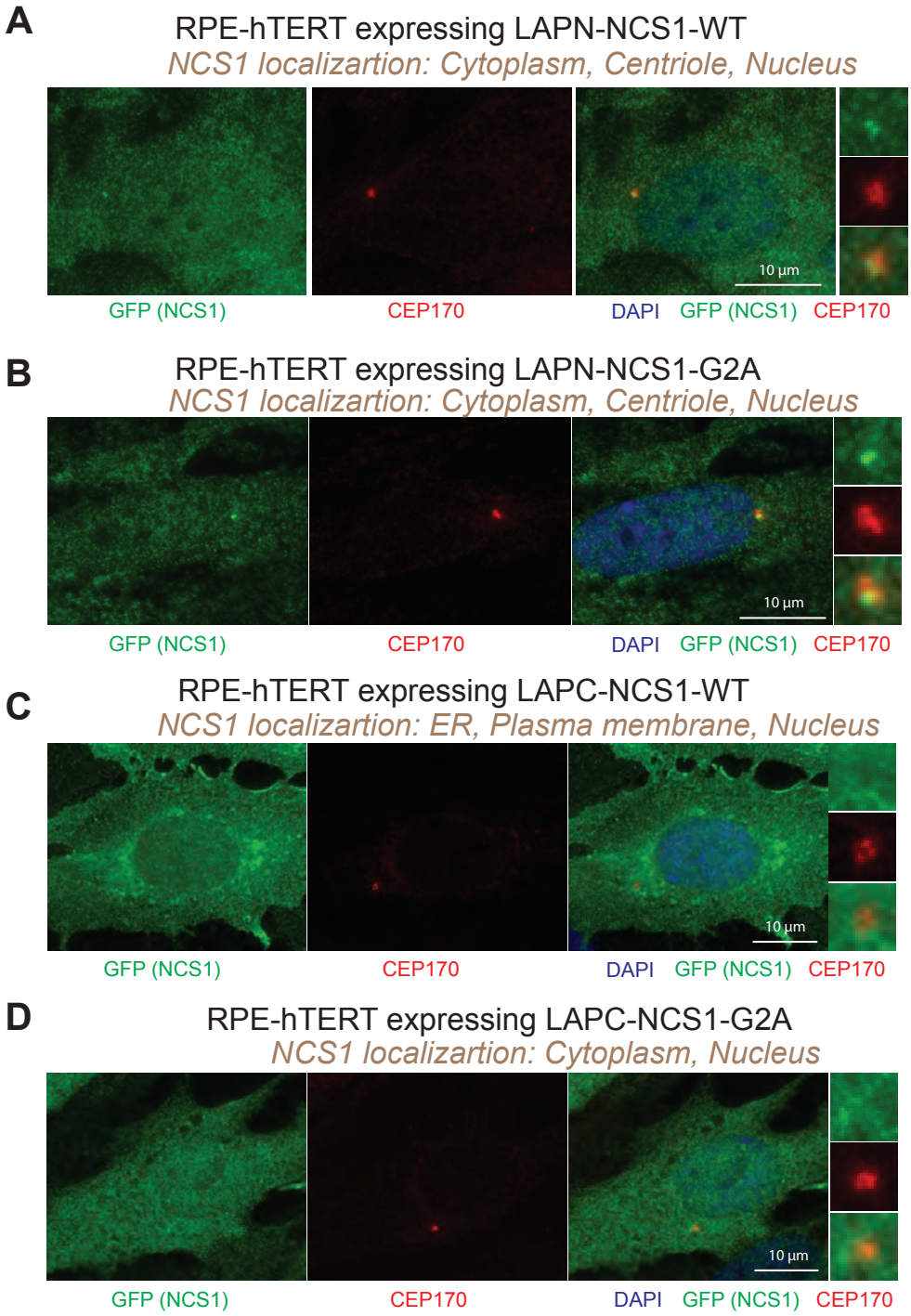

Kanie et al., Figure 2-figure supplement 1

Figure 2-figure supplement 1 ***Localization of GFP tagged NCS1.***

A-D. Immunofluorescence images taken via wide-field microscopy. RPE cells expressing N-terminally LAP tagged wilde-type NCS1 (A), N-terminally LAP tagged myristoylation defective mutant (G2A) of NCS1 (B), C-terminally LAP tagged wild-type NCS1 (C), or C-terminally LAP tagged myristoylation defective mutant (G2A) of NCS1 (D) were serum starved for 24 hours, fixed, and stained with indicated antibodies. Scale bar: 10 μm. Insets at the right panels are the enlarged images of the mother centriole. The experimental conditions are available in Figure 2-Figure Supplement 1-Source Data.

1571

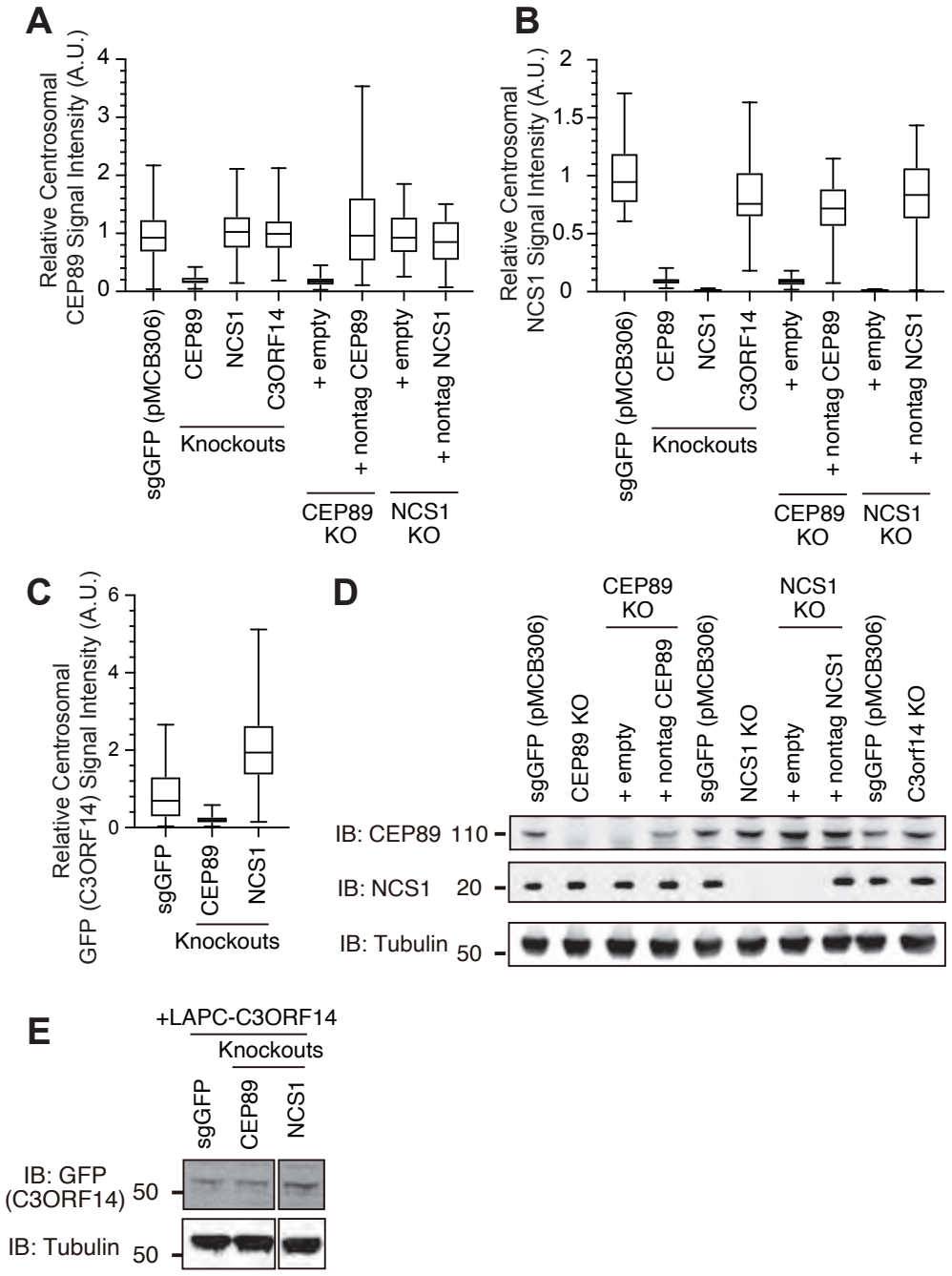

Kanie et al., Figure 2-figure supplement 2

Figure 2-figure supplement 2 ***Quantification data and Westen blot related to Figure 2.***

A-C. Box plots showing centrosomal signal intensity of CEP89 (A), NCS1 (B), or GFP-C3ORF14 (C) from the immunofluorescence experiments shown in Fig.2K-M. Data from a representative experiment are shown. A.U., arbitrary units. The raw data and experimental conditions are available in Figure 2-Figure Supplement 2A-C-Source Data.

D-E. Immunoblot (IB) analysis of expression of CEP89, NCS1, and LAPC-C3ORF14 in indicated RPE cells. The cells were serum starved for 24 hours, lysed and analyzed by immunoblot. Molecular weights (kDa) estimated from a protein marker are indicated.

A.U., arbitrary units; n.s., not significant

1572

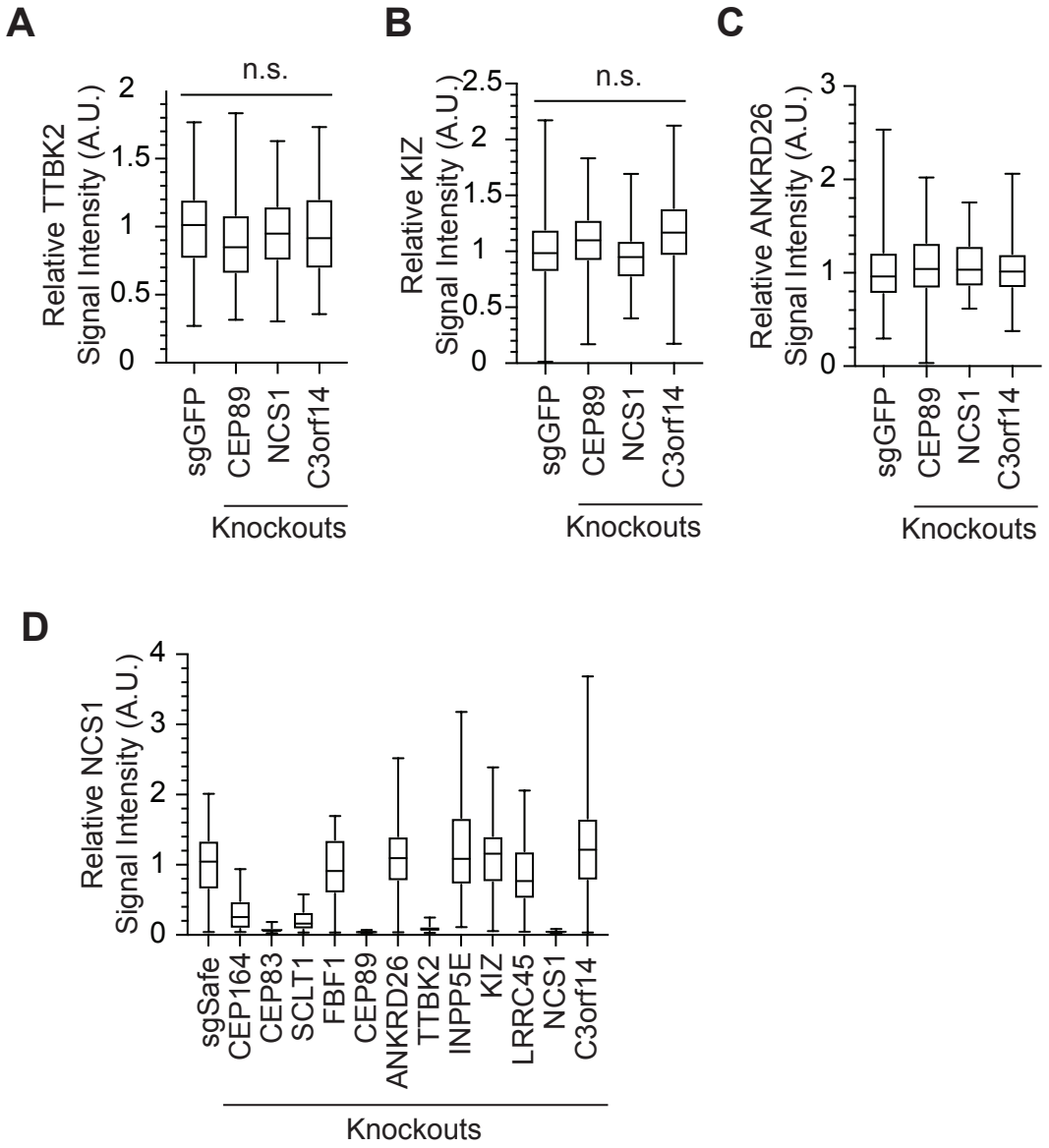

Kanie et al., Figure 2-figure supplement 3

Figure 2-figure supplement 3 ***Localization of distal appendage protein in NCS1 knockouts.***

A-B. Box plots showing centrosomal signal intensity of TTBK2 (A) and KIZ (B) in control (sgGFP), CEP89, NCS1, or C3ORF14 knockout RPE cells. The data combined from three independent experiments. Statistical significance was calculated from nested T test. The raw data, experimental conditions, detailed statistics are available in Figure 2-figure supplement 3A-B-Source data.

C-D. Quantification of centrosomal signal intensity of ANKRD26 (C) and NCS1 (D) in indicated RPE cells. The data from the representative experiment are shown. The raw data and experimental condition are available in the source data of Figure 2-figure supplement 3C-D-Source data.

1573

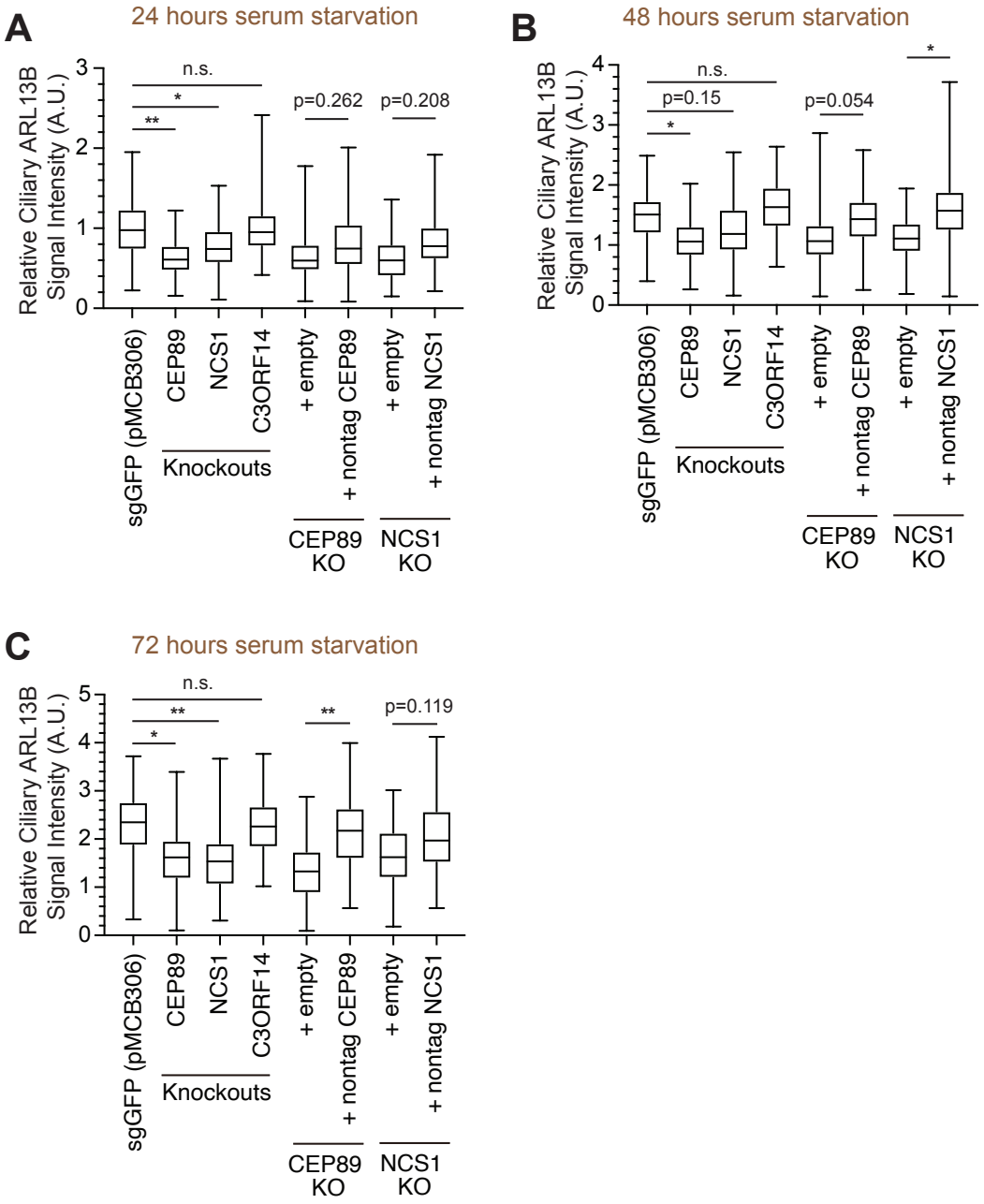

Kanie et al., Figure 3-figure supplement 1

Figure 3-figure supplement 1 ***Quantification of ciliary signal intensity of ARL13B in CEP89 and NCS1 knockouts.***

A-C. Quantification of ciliary signal intensity of ARL13B in indicated cells. The cells were serum starved for 24 (A), 48 (B), and 72 (C) hours, fixed, stained with α-ARL13B (cilium marker) and α-CEP170 (centriole marker), and imaged via wide-field microscopy. Data are averaged from three independent experiments. Error bars represent ± SEM. Statistics obtained by One-way ANOVA with Šídák's multiple comparison test. The raw data, experimental conditions, detailed statistics are available in Figure3-figure supplement 1-Source data.
A.U., arbitrary units.

1574

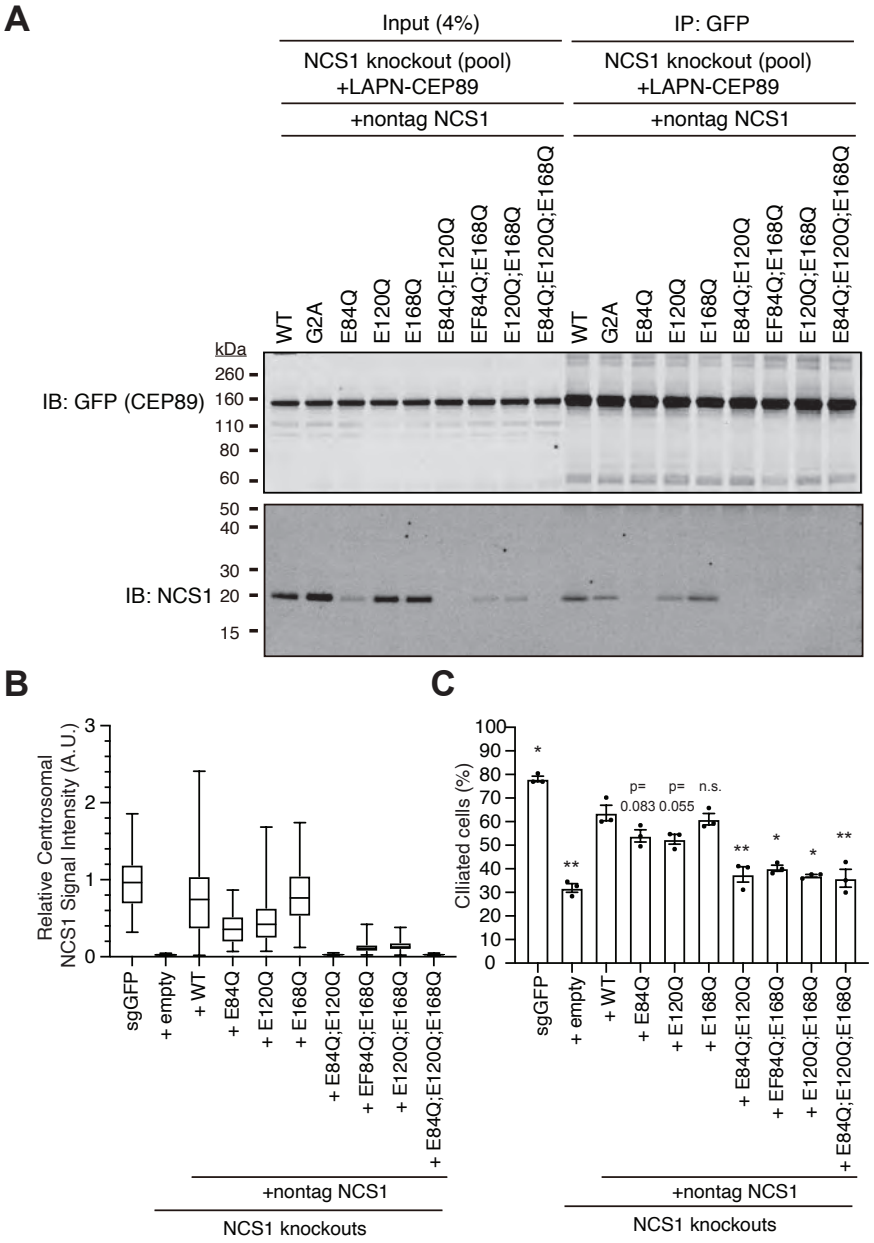

Kanie et al., Figure 5-figure supplement 1

Figure 5-figure supplement 1 ***Calcium is required mainly for the stability of NCS1.***

A. Immunoblot (IB) analysis of the eluates from co-immunoprecipitation assay of NCS1 knockout RPE cells stably expressing wild-type or indicated point mutants of untagged NCS1 and N-terminally LAP (EGFP and S) tagged CEP89. The cell lysates were co-immunoprecipitated with GFP antibodies, resolved by SDS-PAGE and immunoblotted with indicated antibodies. Molecular weights (kDa) estimated from a protein marker are indicated.

B. Box plots showing centrosomal signal intensity of NCS1. Control (sgGFP) or NCS1 knockout RPE cells stably expressing wild-type or indicated point mutants of NCS1were serum starved for 24 hours. Cells were fixed and stained with NCS1 antibody. Centrosomal signal intensity of NCS1 was measured from fluorescent images with the method described in Materials and Methods. A.U., arbitrary units. Data from a representative experiment are shown. The raw data and experimental conditions are available in Figure 5-figure supplement 1B-Source data.

C. Cilium formation assay in cells described in (B) serum starved for 24 hours. Data are averaged from three independent experiments, and each black dot indicates the value from the individual experiment. Error bars represent ± SEM. Statistics obtained through comparing between each mutant and wild-type NCS1 by Welch's t-test. The raw data, experimental conditions, and detailed statistics are available in Figure 5-figure supplement 1C-Source data.

n.s., not significant; *p < 0.05, **p < 0.01, ***p < 0.001

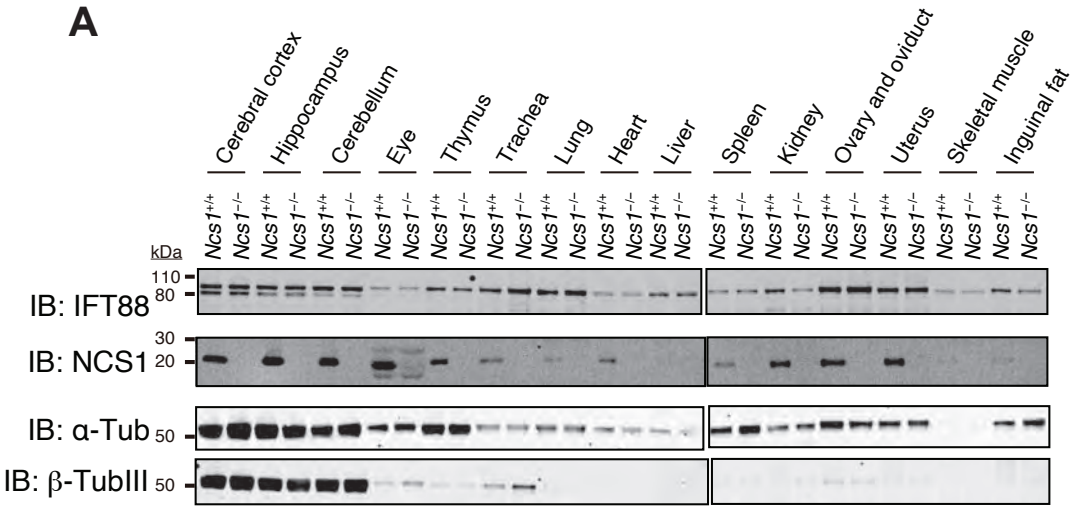

Kanie et al., Figure 7-figure supplement 1

Figure 7-figure supplement 1 ***The expression of NCS1 in various tissues.***

A. Immunoblot (IB) analysis of the indicated tissue lysate from *Ncs1*$^{+/+}$ (7-week-old) or *Ncs1*$^{-/-}$ (6-week-old) mice. 50 μg (for NCS1 detection) or 12 μg (for detection of other proteins) of each tissue lysate was loaded and analyzed by immunoblot with the indicated antibodies. Molecular weights (kDa) estimated from a protein marker are indicated.

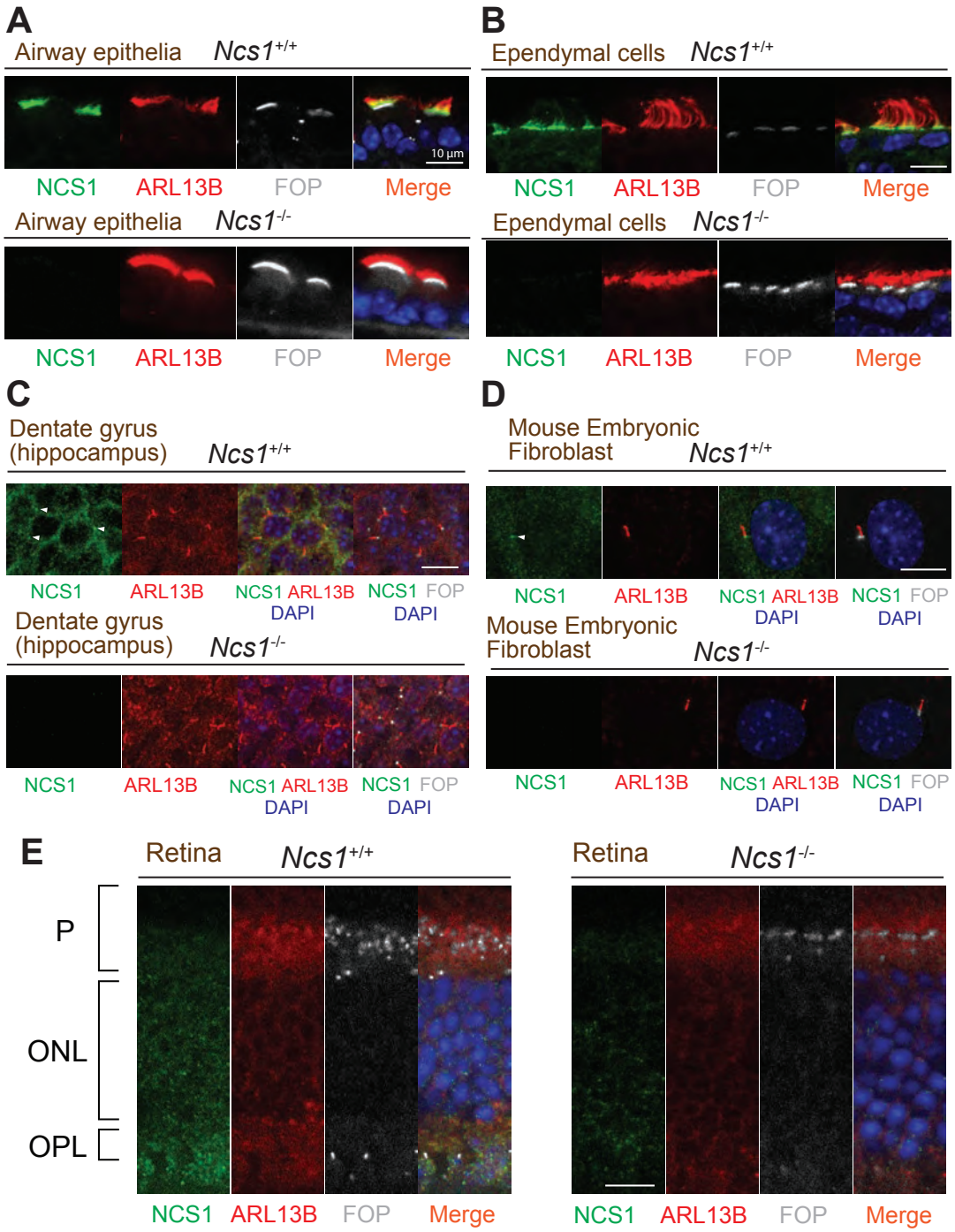

Kanie et al., Figure 7-figure supplement 2

Figure 7-figure supplement 2 ***NCS1 localizes to the ciliary base in most ciliated tissues but not in photoreceptor cells.***

A-E. Immunofluorescence images of indicated mouse tissues taken via spinning disk confocal microscopy. Tissue sections prepared from 8-week-old *Ncs1*$^{+/+}$ or *Ncs1*$^{-/-}$ mice with the method described in materials and methods were stained for indicated markers. Arrowheads indicate NCS1 localization. The individual image is from a representative z-slice. Scale bar: 10 μm. P, photoreceptor cell layer; ONL, outer nuclear layer; OPL, outer plexiform layer.

1577

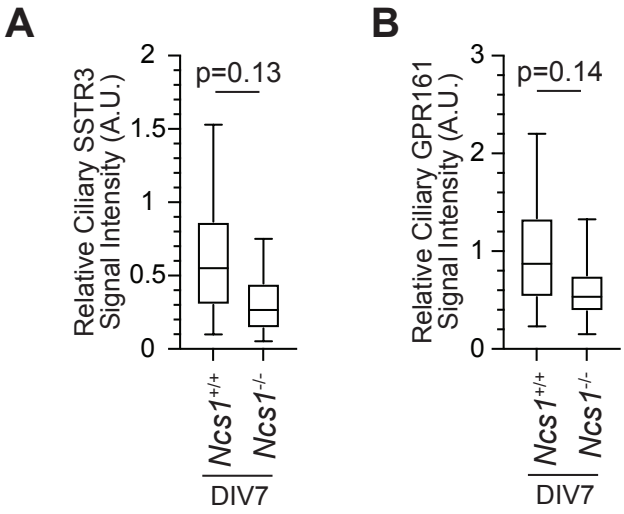

Kanie et al., Fig.7- figure supplement 3

Figure 7-figure supplement 3 ***Localization of ciliary GPCRs is mildly decreased in hippocampal neurons prepared from Ncs1$^{-/-}$ mice.***

A-B. Box plots showing ciliary signal intensity of SSTR3 (A) or GPR161 (B) in isolated hippocampal neurons prepared from E18.5 *Ncs1*$^{+/+}$ or *Ncs1*$^{-/-}$ mouse embryos. The cells were cultured in vitro for 7 days (DIV7), fixed, and stained with either SSTR3 or GPR161 together with α-ARL13B (to mark cilium) and α-FGFR1OP (to mark centriole), and imaged via wide-field microscopy. Data are averaged from five different neurons per genotype for SSTR3 and 3 *Ncs1*$^{+/+}$ and 4 *Ncs1*$^{-/-}$ neurons for GPR161. Statistical significance was calculated from nested T test. The raw data, experimental conditions, detailed statistics are available in Figure 7-figure supplement 3A-B-Source data.